CLINICAL APPLICATION OF MAXIMUM ENTROPY IMAGE PROCESSING IN PLANAR RADIONUCLIDE IMAGING

by

Essam Hussain Mattar

B.Sc., M.Sc.

A Thesis submitted for the degree of

Doctor of Philosophy

UNIVERSITY OF SOUTHAMPTON

NUCLEAR MEDICINE
MEDICAL PHYSICS AND BIOENGINEERING
FACULTY OF MEDICINE, HEALTH AND BIOLOGICAL SCIENCES

February 2000

UNIVERSITY OF SOUTHAMPTON

ABSTRACT

FACULTY OF MEDICINE, HEALTH AND BIOLOGICAL SCIENCES

MEDICAL PHYSICS AND BIOENGINEERING

Doctor of Philosophy

CLINICAL APPLICATION OF MAXIMUM ENTROPY IMAGE PROCESSING IN PLANAR RADIONUCLIDE IMAGING

by Essam Hussain Mattar

Nuclear medicine images are degraded by the physical processes in the imaging system, that affect principally resolution and accentuate noise. Image processing might improve this situation and it is important, that the technique used is capable of dealing with a situation of high noise in the image. The maximum entropy data processing technique, has been found to be useful as a powerful and generally applicable image processing method for reconstructing images from noisy and incomplete data and shown to be of potential value in planar imaging. The aim of the research was to develop the technique of maximum entropy for clinical application and to evaluate its effectiveness in improving image quality.

Maximum entropy (ME) requires definition of various parameters for its operation. Studies were carried out to investigate the way in which the values of these parameters affected image quality. This allows methods for deriving optimal values in any situation to be devised.

A study was carried out to investigate the way in which the figure of merit (FOM) method of image quality assessment depended on definition of regions defining the object and surroundings. This allowed description of a method for defining the regions which provided robust values for FOM.

A comparative evaluation of maximum entropy processing with simple image smoothing (i.e,. conventional smoothing (SM)) and Wiener filtering (WF) was carried out in simulated images of a planar object. Image quality was evaluated using the FOM and using receiver operating characteristic (ROC) analysis with two different observers. The FOM analysis showed that all image processing technique produced significant improvement over the raw data and that ME was the best of the methods. These findings were generally supported by the ROC analysis although, the conclusions were not so clearly defined. There was significant correlation between FOM and detectability for individual observers interpreting images from a single processing technique. Correlation was poorer when data from all the methods were combined.

A further comparative evaluation of the processing techniques in simulated lung images was performed using ROC analysis. The analysis failed to show significant improvements in detectability using conventional smoothing or Wiener filtering. However for one of the observers maximum entropy was better than raw data.

The use of simulated images provided a known true image which was valuable both in objective FOM analysis and in studying visual interpretation. The variability in observation patterns observed for the two different readers made combined analysis of the data difficult but demonstrated the importance of multi-observer studies. FOM can not be used to describe the variability in observer performance.

ME has been adapted to be suitable for clinical use. It gave the best results for processing nuclear medicine planar images, among the techniques studied. This may assist in improving diagnostic accuracy or in obtaining similar quality images with less radioactivity given to the patient or shorter imaging times. It's clinical usefulness is not yet convincingly shown but is of sufficient promise to recommend further studies.

To my most beloved Mother and Father
to whom I owe everything

LIST OF CONTENTS

Chapter One: Physics of Nuclear Medicine Imaging

Chapter Two: Image Processing in Planar Nuclear Medicine Imaging

Chapter Three: Investigations On the use of Maximum Entropy in Planar Radionuclide Imaging Deconvolution

List of Tables

List of Figures

List of Symbols

b	default solution
C_1	multiplicative error parameter for maximum entropy algorithm
C_2	additive error parameter for maximum entropy algorithm
$C_{2\,max}$	maximum value of error parameter C_2 of maximum entropy solutions
$C_{2\,min}$	minimum value of error parameter C_2 of maximum entropy solutions
$C_{2\,op}$	value of error parameter C_2 that gives solutions with similar level of noise
$C_{2\,opt}$	the optimal value of parameter C_2
d	data for problem under consideration(aquired image)
$\mathscr{D}$	the Fourier transform of data (d) {chapter 3}
$\mathscr{D}_t$	real noisy data {chapter 3}
f	fixed percentage for the calculation of $C_{2\,op}$
g	generated noiseless data
H(u,v)	the Fourier transform of the PSF {chapter 5}
H*(u,v)	the conjugate of H(u, v) {chapter 5}
k	counter for data space vectors
L	lower limit of convergence
m	map for problem under consideration (the ideal image)
$\mathscr{M}$	the Fourier transform of map (m) {chapter 3}
m_b	mean value of pixels in background region
m_o	mean value of pixels in object region
n	noise (an additive factor)
N	number of counts
n_b	number of pixels in defined background region
N_{data}	number of data points
N_{map}	number of map points
n_o	number of pixels in defined object region
p	point spread function

$\mathscr{P}$	the Fourier transform of point spread function (p) {chapter 3}
R	matrix specifying map-to-data transform
S	entropy
$\mathscr{u}$	spatial frequency in the x direction {chapter 2}
U	upper limit of convergence
ν	spatial frequency {chapter 1}
$\mathscr{v}$	spatial frequency in the y direction {chapter 2}
$\varphi_f(u,v)$	power spectrum of the object {chapter 5}
$\varphi_n(u,v)$	power spectrum of the noise {chapter 5}
σ	standard deviation of errors
σ_b^2	variance of pixels in background region
σ_o^2	variance of pixels in object region
χ^2	measure of miss-fit between generated and measured data (Chi quare)
$\otimes$	denotes convolution process

Preface

The work described in chapter 4, has been presented in the Institute of Physics and Engineering in Medicine (IPEM), South Western Group Annual Meeting, 8-9 May 1998, at Royal Devon and Exeter Hospital, Exeter, The United Kingdom.

Acknowledgement

In the Name of God, the Most Gracious the Most Merciful, Who Created mankind and Who Said: "We Do raise to (high) degrees (of knowledge) whom We please but over all endowed with knowledge is One the All-Knowing"(S.12,V:76). "And of knowledge, you (mankind) have been given only a little" (S.17,V:85). All my thanks and prayers goes to Him day and night.

I am truly grateful to Dr. John Fleming the Honorary Reader and the Consultant Physicist in the Department of Nuclear Medicine, Southampton General Hospital. I do appreciate his politeness, kindness, enthusiasm, guidance, constructive criticism and encouragement throughout the research. John! It has been an honour working with you. Your patience, tolerance and open threshold will never be forgotten. You have indeed (maximised) the entropy of my knowledge in Nuclear Medicine Imaging and (minimised) the noise which has been located in both the 'ROI' and the 'SBKG region' of my mind. John! your successive radiant of instruction has been completely detected. Thank you (John).

My appreciation is to Dr. Peter Jackson the Reader and Head of Medical Physics and Bioengineering Department, for his supervision, guidance, help and support.

I should particularly like to thank Dr. Paul Kemp, Consultant Physician in Nuclear Medicine, for spending part of his time reading the 'unclear' nuclear medicine images which I used in this thesis.

I do thank the staff of the Nuclear Medicine and Medical Physics Departments, for their kindness and support during the pleasant period I spent with them. Many thanks to all who have helped me with advice and assistance, particularly Alan Aldous (he is now in Ipswich hospital), Peter Halson, Keith Goatman and Dr. Maria Tristam. They have indeed helped ease the difficulties that had faced me throughout my research. Peter Halson! I really do appreciate your enthusiasm, assistance, patience and specially your politeness in answering my enquires, even if you are busy. I think

you found a little bit of peace when you moved to the office next door, I wish you all the best. Also my thanks go to my office colleague, Angela Darekar, Veronique Sauret and Chris Monk for their guidance and friendship. I also thank Dr. Valerie Lewington, and Dr. Lorraine Wilson, for trying to help in reading the preliminary test images, Dr. Vince Batty for his advice regarding the lung segments and offering to help in reading the images. Also Lesley Leavesley, Dean Martin, Nick Bryant and Livia Bolt for their help and support. A special thanks to the secretaries, Linda Lemon, Lucy Bolton, Elaine Glover, Judy Coltman and Riva Doncom for their help and beautiful smile. And to everyone I have not named, thank you from the bottom of my heart.

I wish to thank Professor Charles E. Metz, from the University of Chicago Medical Center, Chicago, USA, for providing me with the software for ROC analysis and for his help in answering my enquiries.

My great compliment is to the Kingdom of Saudi Arabia, for the grant and the financial support they provided during the period of my study. Also my thanks go to the Saudi Arabian Cultural Bureau in London, particularly the cultural attaché Mr. Abdullah Al-Nasser and my supervisor Mr. Ahmed Sabry, for their fantastic supervision, support and encouragement.

My great respect, special thanks and gratitude are to the souls of my kind, dearest and the most beloved **Mother and Father**, whom without their guidance, support and excellent upbringing I could not have reached where I am now.

My special thanks also to my wife, daughters, brothers and sisters, for their care and enthusiastic support.

I am very grateful to my lovely wife Lina Hammad, who indeed showed her love, care, compassion and sacrifice, before, during and I am sure after our long stay in the United Kingdom, carrying out our research together. Lina! it was not easy to play a fantastic role similar to what you did, you have been a wife, a mother, a confidant as well, and on top of this have managed to squeeze in being a PhD student.

Similarly my gratitude is to my three little treasures Rafif, Rahif and Reef. You are really the candles that lighten our life.

Abbreviations

ADC	analogue-to-digital convertor
AFROC	alternative free-response receiver operating characteristic analysis
ANT	anterior
ARSAC	administration of radioactive substances advisory committee
AUC	area under ROC curve
BKG	background region
c/p	counts per pixel
c/s	counts per second
CI	confidence interval
cm	centimetre
cn1	contrast 1
cn2	contrast 2
cn3	contrast 3
CPU	central processing unit
CRT	cathode ray tube
CT	computerised Tomography
DTPA	diethylene triamine pentaacetic acid
EC	electron capture
FOM	figure of merit
FPF	false-positive fraction
1 - FPF	specificity (1 - false positive fraction)
FROC	free-response operating characteristic analysis
FWHM	full width half maximum
HAM	human albumin microspheres
IT	isomeric transition
keV	kiloelectron volt
LAO	left anterior oblique
LL	left lateral

LPO	left posterior oblique
LROC	location ROC analysis
LSF	line spread function
MAA	macroaggregates
MBq	MegaBecquerel
MDP	methylene-diphosphonate
ME	maximum entropy
MLEM	maximum likelihood expectation maximisation
MRI	magnetic resonance imaging
MTF	modulation transfer function
NaI(Tl)	sodium iodide with trace quantities of thallium added
PE	pulmonary embolism
PET	positron emission tomography
PHA	pulse-hight-analyzer
PICS	portable imaging computer software
PIOPED	prospective investigation of pulmonary embolism diagnosis
PM	photomultiplier
POST	posterior
PSF	point spread function
RAO	right anterior oblique
RD	raw data
RL	right lateral
ROC	receiver operating characteristic analysis
RPO	right posterior oblique
SBKG	surrounding background region
SCTA	spiral computed tomography angiography
SD	standard deviation
SM	conventional smoothing
TN	true negatives
TP	true positives
TPF	sensitivity (true positive fraction)
V/Q	ventilation and perfusion scintigraphy
WF	Wiener filter

^{11}C	carbon-11
^{18}F	florine-18
^{123}I	sodium iodide-123
^{81m}Kr	krypton gas
^{13}N	nitrogen-13
^{15}O	oxygen-15
^{99m}Tc	technetium-99m
$^{99m}TcO_4^-$	technetium pertechnetate
^{201}Tl	thallium-201
^{133}Xe	xenon gas

Chapter One

Physics of Nuclear Medicine Imaging

1.1 Introduction

Nuclear medicine imaging is a process which involves radioactive material and an appropriate imaging instrument. The result of the process is formation of an image, which is useful in the diagnosis of different diseases. The image formed is a distribution of a radioactive material in the body, after its administration usually into the patient's circulatory system. The radioactive material used is a radio-labelled tracer: a radionuclide, which is a gamma emitter, it is incorporated into a pharmaceutical (chemical) substance with a specific physiological properties. The incorporation will produce a substance, called a radiopharmaceutical. The distribution can be measured by using an external radiation detector. The most common instrument which acts as an external detector for imaging in nuclear medicine, is the gamma camera. It detects the emitted radiation from the patient, building up an image of the tracer distribution. The information produced is useful for assessing the function of different organs.

Image formation and quality depends on the limited amount of radioactivity that can be administered to the patient. It is necessary to use low levels of radioactivity, so that the radiation potential hazard to the patient can be kept to its minimal.

In this chapter it is briefly considered how to choose radionuclides which are useful in nuclear medicine imaging and how they are produced. The imaging system is described from the emission of gamma photons from the patient, through their

interaction with tissue to their detection by gamma camera. The effects of different factors on the image quality are considered along with some methods of evaluating image quality. The applications of nuclear medicine images are also considered and thus the motivation for image processing and its usefulness for diagnostic purposes. In addition the proposed work which is going to be described in this thesis is presented. More information on the ideas reviewed in this chapter can be found in Blahd 1971, Aird 1975,1988, Gottschalk et al 1976, Parker et al 1978, Sharp et al 1985, and Sorenson and Phelps 1987.

1.2 Choosing the Radionuclide for Imaging

Only a small number of radionuclides are clinically useful in nuclear medicine imaging. The principal factors which need to be considered when selecting a radionuclide are the type of radiation emitted, the energy and abundance of gamma rays and the half-life. It is necessary that the radiation used should be sufficiently penetrating to be externally detected. The radiation resulting from the decay of radioactive materials consists of either particles (alpha, beta, positron) and/or photons (gamma). Charged particles and very low energy photons have a very limited range in tissue, because the energy they carry is dissipated within the patient and so can not be used for imaging. In contrast, higher energy photons may traverse several centimetres of soft tissue without interacting with it. Thus they can be detected outside the patient's body using an external radiation detector and used to form an image of the in-vivo distribution of radioactivity in the organs of interest. This limits the choice to radionuclides which emit gamma, x-rays and positrons (Robertson 1982). One class of radionuclide which is particularly useful in imaging consists of those which have a metastable state. In these radionuclides the excited state, following beta emission and prior to gamma emission, has a relatively long half life. This is an important process for imaging, because if the product nuclide can be physically separated from its parent while in the excited or "metastable" state, then it is possible to obtain an almost pure gamma emitter; which undergoes the decay by isomeric transition (IT); e.g., Technetium-99m (Sorenson and Phelps 1987). Another good source for imaging is those radionuclides which decay by

electron capture (EC); which will emit x-rays characteristic of the daughter nuclide, in addition to gamma rays, e.g., ^{123}I, ^{201}Tl. Some radionuclides decay emitting a positron, such as ^{15}O, ^{11}C, ^{13}N, and ^{18}F. These positron emitters have been used in positron emission tomography (PET). The emitted positrons annihilate with a nearby electrons emitting two gamma photons, each of energy 511 keV, travelling in opposite directions.

In radionuclide imaging it is important that the radiation given off should be sufficiently penetrating to allow it to be detected externally. The energy of the radiation will affect its ability to penetrate tissue. However, high energy gamma-rays, are difficult to stop in the external imaging device, (detector) and in the collimation of radiation. In contrast, low energy gamma-rays will be subject to more scattering and absorption in the patient tissue. Therefore, it is possible to use gamma-rays with energies between 50 keV and 500 keV. The optimal energy range which is preferred is between 120 keV and 200 keV.

The half life of the radionuclide determines how quickly the radioactivity will decay. It is a useful measure of the rate of decay of a radionuclide being the time taken for a pure radionuclide to decay to half its initial activity. Obviously, if a short life radionuclide is used, then the imaging time should be considered. If the half-life is very short then the activity will have decayed to a very low level before imaging has started, if it is too long then the patient will remain radioactive for a considerable time, which means, an increased radiation dose to the patient. Therefore, as a general rule the half-life of the radionuclide should be comparable to the length of the investigation in order to minimise the radiation dose to the patient.

1.3 Radiopharmaceutical

The principle of the use of radiopharmaceuticals in nuclear medicine imaging is that very low levels of radioactivity are added to biological compounds to label them, so that they can be administered into the patient usually intravenously and followed through the body in various ways (Eckelman 1988). The path or accumulation site of

the labelled compound is determined with an external radiation detector. A labelled compound has one or more of its atoms substituted by a radioactive atom. The compound to be labelled must be a substance that is non-toxic in the concentration to be used and free from micro-organisms.

1.4 Production of ^{99m}Tc

Nuclear medicine imaging requires radionuclides, which are easily available and simple to use. Technetium-99m is currently the most popular radionuclide for nuclear medicine imaging studies. It is a metastable radionuclide, which emits a certain number of conversion electrons, thus it is not a pure gamma-ray emitter; however, the ratio of photons to electrons emitted is greater than for beta emitters which have an accompanying gamma-ray (Sorenson and Phelps 1987). This is an advantage for studies requiring detection of gamma-rays from internally administered radioactivity. Obviously, the production of Technetium-99m from a generator has different important advantages, the gamma-rays energy produced (140 keV) are very useful for the detection with gamma camera, it's short half-life (6 hours), ready availability, low cost and easy labelling to different variety of imaging agents.

Radionuclide generators work on the principle that a parent nuclide with relatively long half-life decays to produce a short lived daughter nuclide. Where the chemical nature of parent and daughter are quite different, it allows separation of the daughter from the parent. Molybdenum-99, ^{99}Mo, (parent) has a half-life of 2.8 days. It decays to it's daughter nuclide ^{99}Tc in the form of pertechnetate, $^{99}TcO_4^-$ through the metastable radionuclide ^{99m}Tc. Molybdenum-99, (^{99}Mo) is produced by an (n, γ) reaction or fission in a nuclear reactor. It decays to ^{99m}Tc by beta (β) decay (Figure 1.1). This radionuclide has a half life of 6 h and decays to ^{99}Tc.

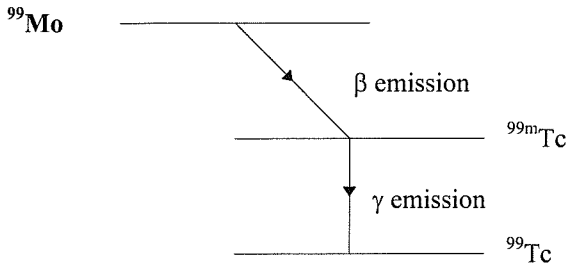

Figure 1.1: The decay scheme of ^{99m}Tc.

1.5 The Gamma Camera

1.5.1 Basic Principle of Operation

Measurement of the distribution of a radionuclide within the body can provide important diagnostic information to aid in clinical decision making. Medical radionuclide imaging developed with the introduction of the rectilinear scanner by Ben Cassen in the early 1950s (Cassen et al 1951 and Mayneord et al 1951). The image was obtained by moving the detector in a rectilinear manner over the patient, by scanning point by point and observing the variation in count rate produced. This is a relatively time consuming process, which restricted the use of radioisotope scanners. The use of radionuclide imaging has become increasingly widespread with the development of the gamma camera, which has become a standard equipment in nuclear medicine. The gamma camera was introduced in 1958 by Hal Anger using a single large area of NaI(Tl) crystal and an array of photomultiplier tubes (Anger 1958). He utilised a stationary detector which viewed a larger area simultaneously. This enabled images to be obtained in a shorter time. The Anger camera has been continuously improved most recently through the addition of digital processing to the analogue detector electronics.

The gamma camera consists of two units (Figure 1.2), the collimated detector and the console containing pulse processing electronics and displays. The basic principle of operation and image formation with the gamma camera is as follows. In the camera's head, a collimator is positioned, to limit the gamma-rays which are emitted from the patient that are allowed to reach the detector. Since the emission of gamma-rays will be emitted isotropically in random directions, the collimator is used to allow only the gamma-rays which are travelling perpendicular to the detector to pass through it. Thus, collimated gamma-rays from the patient strike the thallium-activated sodium iodide [NaI(Tl)] crystal, which is located at the back of the collimator, producing a scintillation of light. The scintillation is detected by a large number of photomultipliers (PM) tubes (typically 37-91) arranged in a closely packed hexagonal array, and optically linked to the crystal.

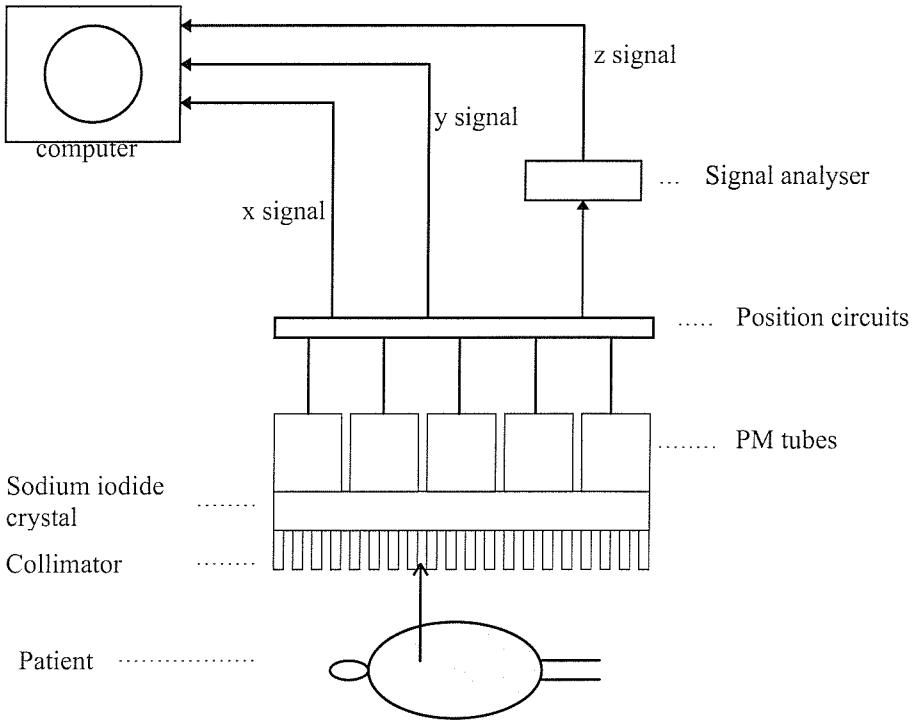

Figure 1.2: Schematic diagram of the Gamma Camera

The light from the scintillation divides among the PM tubes; those tubes close to the event receive the more light than those further away. Each tube converts the light into a voltage pulse, each pulse being proportional in amplitude to the amount of light each tube has received. The pattern of voltage pulses from all PM tubes determines the original scintillation position on the crystal. The computer receives the pattern of voltage pulses and produces three major output signals. Two of these output signals, the x and y positioning signals correspond to the position of the original gamma-ray scintillation on the NaI(Tl) crystal detector. The third signal from the computer (z signal) is a summation of the pulses from all of the PM tubes and is proportional to the energy loss from the gamma photon which produced the original scintillation. This signal is fed to a pulse height analyser set to pass only the voltage pulses which correspond to the photopeak of the spectrum of radiation. When a photopeak event has occurred (i.e., when the z signal gives the permission) it is allowed to contribute to the image. The final display shows the radiopharmaceutical distribution within the patient, as projected onto the detector plane. The image can either be recorded by photographing the pulses on a CRT screen or by storing them in a digital matrix on computer.

1.5.2 Acquisition of Data

In the past most gamma cameras recorded images in analogue form on photographic film. However as early as the 1960s devices were developed to convert the images to digital form on a computer. There are many advantages of digital over analogue images and these include control over the image display for better visualisation and the ability to quantify images.

A digital nuclear medicine image is essentially an array of numbers representing the variation of number of counts detected across the field of view of the gamma camera. Each event is recorded in the memory by adding it at the appropriate x and y location in the 2D matrix. This may be subsequently displayed as a grey-scale image for further analysis. The storage of the events is performed, by computer, in matrix mode covering the field of view of the camera. Each element of a square matrix (n ×

n) represents a small area of the field of view, called a pixel, that registers photons from a small specific region of the object. Therefore, the pixel intensity at any point in the image is related to the activity in the corresponding region in the subject being imaged. The width of this element is given by dividing the field of view by the matrix size. The pixel size used is determined by the resolution of the gamma camera. The Nyquist theorem requires that the pixel size must be less than half the resolution of the imaging device.

The field of view on the ADAC Dual Head Genesys gamma camera is 50.8 × 38.1 cm, which corresponds to a pixel width of 0.467 cm or 0.94 cm in 128 × 128 or 64 × 64 matrix respectively. In this investigation the resolution was at best about 11 - 12 mm and therefore a 128 × 128 matrix was used with a pixel size of 4.7 mm .

The production of digital nuclear medicine images involves routing x, y and z analogue pulses that go to the CRT in analogue cameras to the computer interface input. These analogue pulses are converted to digital form by an analogue-to-digital converter (ADC). The gamma camera interface converts the signals from the camera into digital form and the data is then transferred to a computer where it is stored as a matrix of numbers. This allows the image to be processed and manipulated for the different studies.

A nuclear medicine computer system consists of hardware components combined with software programs. The hardware components consist of gamma camera interface, CPU and memory, hard disk and magnetic tapes for storage, display and copy facilities. The software controls all data acquisition and processing. It includes image display manipulation and analysis and specific clinical application routines.

1.6 Factors Affecting Image Quality

In the image formation of a radionuclide within a patient there are many factors that contribute to the formation of a good radionuclide image with correct interpretation.

The nuclear medicine image quality is affected by several different factors, spatial resolution, attenuation, scatter and noise.

1.6.1 Spatial Resolution

Image spatial resolution describes the sharpness or detail of the image. In a gamma camera the total or system resolution is composed of the intrinsic or detector resolution and the geometric or collimator resolution (Knoll 1979, Sharp et al 1989) . The limit of spatial resolution achievable by the detector and the electronics is known as the intrinsic resolution of the camera. It is caused primarily by the statistical fluctuation in the distribution of pulse sizes between PM tubes from one scintillation event to the next. Multiple photon scattering within the detector, is another factor which has a much smaller effect. The intrinsic resolution will get worse with decreasing the energy of gamma-rays, because fewer light photons per scintillation event will occur, which result in large relative fluctuations in their distribution.

The collimator hole geometry, length, shape and diameter affect the collimator resolution and efficiency. The septal penetration by gamma-rays crossing from one collimator hole into another must be very small, to get a reasonably accurate gamma-ray image projected by the collimator onto the detector. The thickness of the septa will be determined by the energy of the gamma-ray being imaged. A collimator with thick septa, can be used for higher energy gamma-rays and thin septa for low energy. For a given septal thickness, collimator resolution will be improved at the expense of decreased collimator efficiency and vice versa.

The spatial resolution can be measured by the line spread function (LSF) or point spread function (PSF). These are the graph of net count-rate, of point or line image, as a function of the x-coordinate when the line source is placed parallel to the y-axis in a plane parallel to the collimator face and at a given distance from it (i.e., the counting-rate profiles recorded across the images of point or line source). Although the complete LSF or PSF is needed to fully characterise spatial resolution, a partial

specification is provided by the full width at half-maximum (FWHM) of the LSF or PSF (Figure 1.3).

The most detailed specification of spatial resolution is provided by the modulation transfer function (MTF). The MTF is a method of assessing the performance of any imaging equipment. The evaluation of an imaging system could be measured with a sinusoidally varying activity distribution. The activity distribution varies with distance at a specific frequency (cycles/mm). This called the spatial frequency ν of the test pattern. The contrast, or modulation, of the test pattern is defined by:

$$C_{in} = (I_{max} - I_{min}) / (I_{max} + I_{min}) \qquad 1\text{-}1$$

where I_{max} and I_{min} are the maximum and minimum radiation intensities emitted by the test pattern. C_{in} is the input contrast and it ranges from zero ($I_{max} = I_{min}$, no contrast) to unity ($I_{min} = 0$, maximum contrast). Similarly, output contrast C_{out} is defined in terms of the modulation of output image (e.g., image density or counting rate recorded from the test pattern). The ratio of output to input contrast is the modulation transfer function for the spatial frequency ν of the test pattern,

$$MTF(\nu) = C_{out}(\nu) / C_{in}(\nu) \qquad 1\text{-}2$$

The MTF can in fact be measured in a much simpler way by measuring a line spread function (LSF), the response of the camera to a line source of radioactivity. A Fourier Transform of the LSF describes it as a summation of sine waves of different frequencies. This equates it to the MTF.

For an imaging system a flat MTF curve with a value near unity produces an image that is a faithful reproduction of the imaged object. Good low-frequency response is needed to outline the coarse details of the image and is important for the presentation and detection of relatively large but low-contrast lesions. Good high-frequency response is necessary to portray fine details and sharp edges. This is of obvious importance for small objects, but also sometimes for larger objects because of the

importance of edges and sharp borders for detection of low-contrast objects and for accurate assessment of their size and shape.

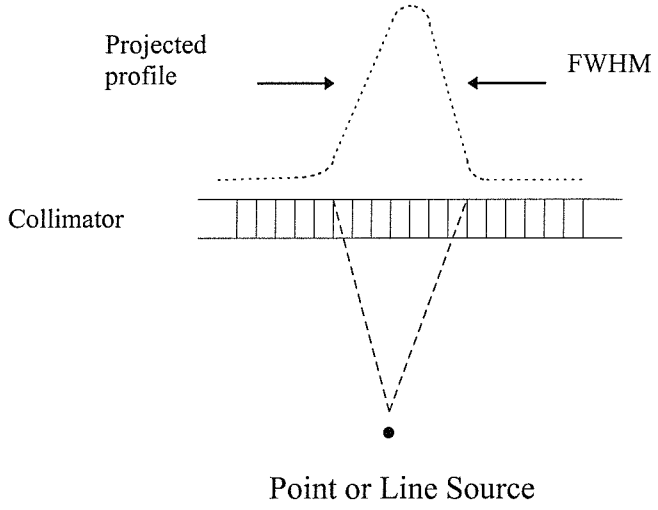

Figure 1.3: Radiation profile (point or line spread function) for a parallel-hole collimator. The FWHM (full width at half-maximum) of the profile is used to characterise collimator resolution.

1.6.2 Attenuation and Scatter

The tissues of the patient have an effect on the emitted gamma photons, where attenuation and detection of scattered photons cause significant problems in the formation and interpretation of images. Attenuation and scattering are mainly caused by Compton scatter in the patient, where the direction and energy of a gamma photon is changed by interaction with electrons (Figure 1.4). A relatively small contribution to attenuation (at about 140 keV) is caused by photon absorption in tissue due to the photoelectric effect. Attenuation is where a photon is going towards the detector, but doesn't reach it because it is stopped by absorption or scatter. The

attenuation of photons that would have reached the detector will result in fewer photons being counted in the detector. This will increase the noise and lead to an emphasis of structures with little intervening tissue over deeper structures.

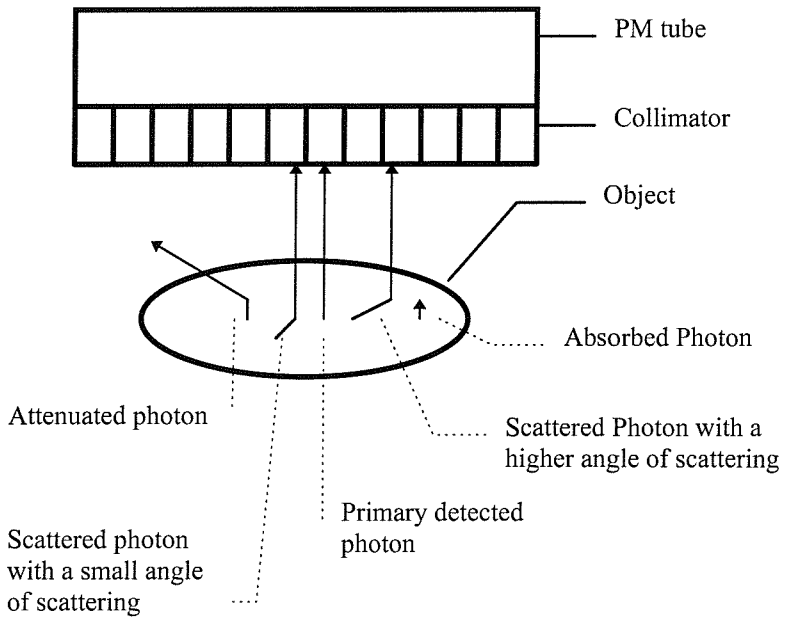

Figure 1.4: The interaction effects between Photons and Tissue.

The term scatter usually refers to the detection of photons following a Compton scatter event, which were originally not travelling in a direction to be detected. This leads to the possibility of detecting malpositioned event. The photons will deviate from their path in travelling towards the detector and lose energy. Therefore, most scattered photons will be rejected by the energy window because they have a lower energy and lie outside the energy window. However some of scattered photons will be within the energy window and will be accepted. The NaI(Tl) detector will therefore not reject all scattered radiation, especially for gamma-ray energies below 200keV. Scattered photons can form around 20% of the count in an image. It has

been determined that the best trade-off between noise and scatter rejection is obtained with a 20% energy window centred on the gamma-ray energy of interest.

So, scattered radiation and septal penetration are additional causes of contrast degradation. Both have the effect of adding a background counting rate to the image in the vicinity of radiation sources.

Decreased contrast results in poorer detectability of both large low-contrast objects as well as fine details in the image. Figure 1.5, for example, illustrates the effects of scattered radiation (or septal penetration, which has similar effects) on the point-spread function and MTF of an imaging system. The addition of long tail to the PSF results first in the suppression of the MTF curve at low frequencies. This is reflected in poorer contrast of large objects which makes large low-contrast objects more difficult to detect and define. There also is a suppression of the high-frequency portion of the MTF curve that has the effect of shifting the limiting frequency for detection of high-contrast objects, e.g., bar patterns, to lower frequencies. Thus, the contrast-degrading effects of scatter and septal penetration decrease the visibility of all structures in the image, particularly those that are near the borderline of detectability. Background radiation, e.g., from over- and underlying activity, has similar effects. These effects will result in a perceptible loss of image sharpness as well as overall image contrast when overlying activity or scattered radiation are present.

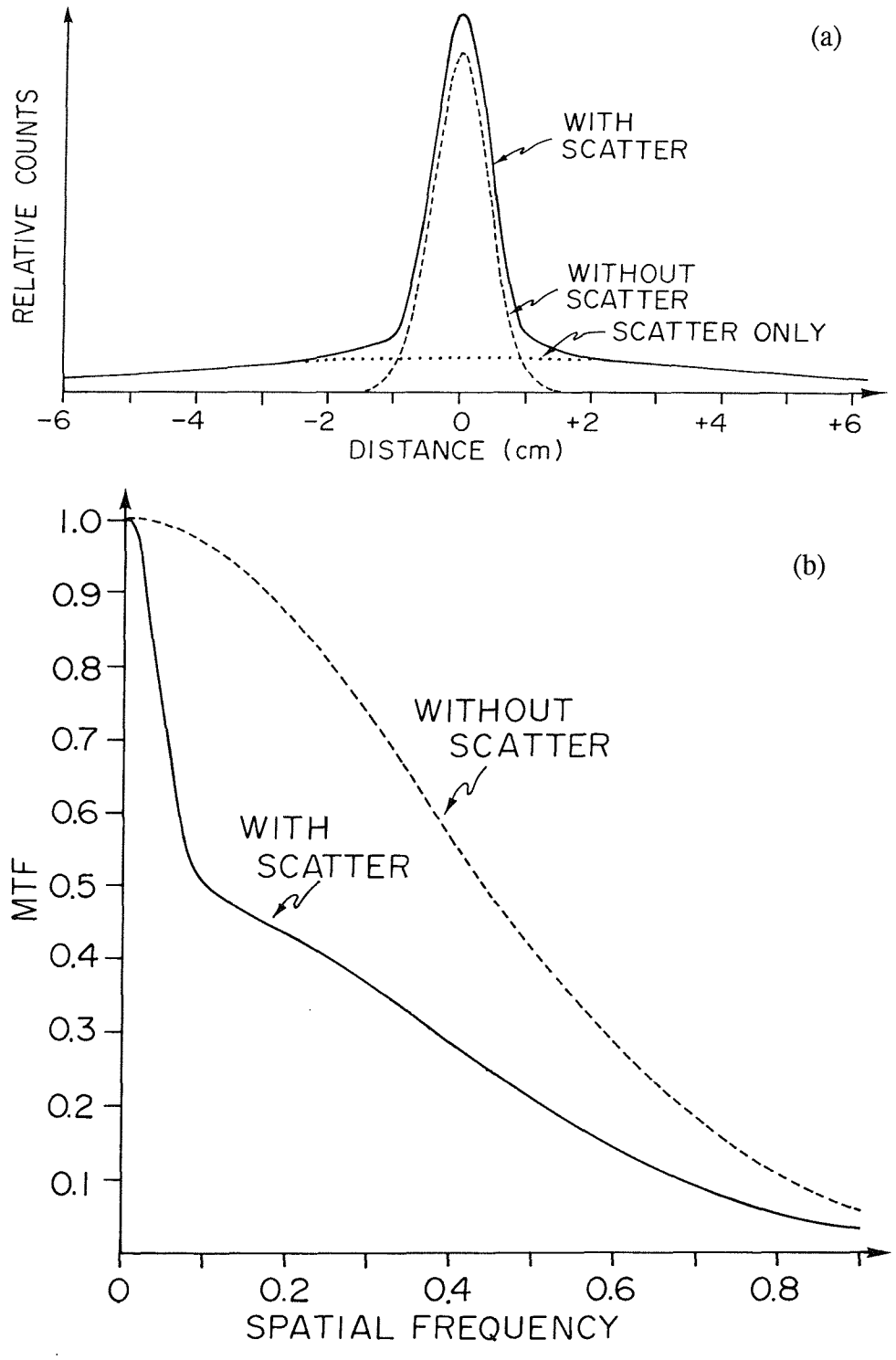

Figure 1.5: Demonstration of the effects of scatter and/or septal penetration on (a) point spread function and (b) MTF of an imaging system. The long tails on the PSF have the effect of suppressing the MTF curve at both low and high spatial frequencies.

1.6.3 Noise

Nuclear medicine images contain noise which limit their quality. This noise may be either random or structured. Random noise in an image occurs due to random fluctuations in radioactive decay and attenuation. It is the statistical fluctuation of the count rate. Structured noise occurs due to non-random variations in counting rate superimposed on the object of interest, it also can be caused by imaging system artefacts. In most clinical radionuclide images, noise has an effect on image quality. There are certain factors which influence noise in an image. The physical process of gamma photon emission is random in nature, because it is impossible to predict at any given time which one if any of the radioactive nuclei will decay. Also scintillation events in the crystal and their detection by the photomultiplier tubes are processes with random errors and these effects combine to give a source of Poisson distributed random noise in the image.

Random noise is directly related to the information density of the image, which is the number of counts recorded per unit area of the image. The relative amount of noise, or variation in photon concentration, is inversely related to the number of photons used to form the image. Information density of images can be increased by increasing the counting rate or the imaging time. Information density has important effects on the minimum detectable size and contrast of lesions in nuclear medicine images.

Assuming the number of counts, N, recorded in an area, A, of an image, where the information density is ID counts cm^{-2} , thus the number of counts and the standard deviation in counts are given (Sorenson and Phelps 1987), by:

$$N = A \times ID \tag{1-3}$$

$$\sigma = \sqrt{A \times ID} \tag{1-4}$$

The percentage standard deviation in counts, P_n or noise, is given by:

$$P_n(\%) = (1/ \sqrt{A \times ID}) \times 100\% \qquad (1\text{-}5)$$

Therefore in order to detect a lesion of size A, one should distinguish it from random noise in the image of magnitude given by equation (1-5). For this purpose, a lesion contrast should be much higher than the noise, defined as the standard deviation of counts per pixel.

Noise can be reduced by using a high sensitivity collimator or smoothing at the expense of resolution. A compromise has to be made between sensitivity and resolution. Reducing noise by increasing the number of counts may increase the absorbed dose to the patient.

1.7 Methods of Evaluating Image Quality

The gamma camera images are not perfect images of the underlying radionuclide distribution. There are certain inherent imperfections that arise from the performance characteristics of the detector, the electronics and the different types of collimators (Sorenson and Phelps 1987). The causes of these imperfections, and their effects on the image quality are affected by a number of different factors. Image quality can be evaluated by two methods. Firstly, by the physical camera performance assessment that can be measured or calculated for the image or imaging system. Secondly, by image performance assessment, where it is divided into two types (i) a subjective assessment, involving measurement of the ability of observers to detect objects with different imaging systems and under various conditions, (ii) an objective assessment, involving measurement of quantitative parameters such as the contrast to noise ratio. This acts as an intermediate stage between physical performance and subjective assessment.

1.7.1 Physical Camera Performance Assessment

1.7.1.1 Image Non-linearity

Image non-linearity, means a distorted image, where a straight line objects appear as curved line images. This occurs when the x- and y- position signals do not change linearly with displacement distance of a radiation source across the face of the detector. It results from random and systematic errors in the calculation of events detected by the detector. On properly functioning cameras, the non-linearity is almost undetectable and rarely interferes directly with image interpretation; however, it can cause image non-uniformity in regions of uniform count density. Non-linearity is assessed by imaging a parallel-line bar phantom or orthogonal hole phantom.

1.7.1.2 Image Non-Uniformity

When a uniform distribution of activity is imaged on a gamma camera, it shows areas of above and below average count density. There are two major causes for image non-uniformity: (i) nonuniform detection efficiency which arises from small differences in the pulse-height spectrum for different photomultiplier tubes, (ii) image non-linearity. The non-uniformity assessment is performed by obtaining an image of a flood-field source.

1.7.1.3 Sensitivity

Sensitivity is considered as the camera detection efficiency. It is defined as the count rate obtained per unit radioactivity. It is affected by the type of collimator and deteriorates as collimator resolution improves.

1.7.1.4 Energy Resolution

Energy resolution determines the accuracy with which the energy of the radiation can be measured. It is an important parameter in the gamma camera, where the measurement of gamma-ray energy will determine whether or not the event will be rejected as a scattered photon. A convenient measure for the energy resolution is the width of the photopeak in the energy spectrum, which is known as the full-width at half-maximum (FWHM).

1.7.1.5 Count-Rate Performance

The relationship between observed and true count-rate is referred to as the count-rate characteristic. The count-rate performance is influenced primarily by the dead-time, which is the minimum time interval that separates two events in order they are recorded as two separate pulses. Dead time gives rise to a systematic underestimate of count rates, the magnitude of which increases with count rate.

1.7.2 Image Performance Assessment

1.7.2.1 Human Perception and ROC Methods

Images are rich in information and in deciding what an image represents, an ideal observer will take account of all the relevant information present. The human visual system is a fundamental part of medical image interpretation. Human observers are disturbed by the presence of noise and unsharpness in the image and these defects impair perception. Usually performance is measured in terms of what the observer can detect. Detecting a feature in an image means, to observe its presence but not necessarily specifying its form. There are three aspects of perception performance, (i) detection, where a decision is made as to whether some abnormality is present, (ii) recognition, where features such as size and shape of an abnormality are quantified and (iii) identification, where decisions are made as to likely disease

patterns that correspond to the recognised, detected abnormalities. The measurements can be performed by the so-called 'receiver operating characteristic' (ROC) methods (Metz et al 1976, Kelsey et al 1985, Herman et al 1989, Metz 1989, Chesters 1992, Gooley et al 1992). It is used in measuring the perceptual performance and yields a measure of inherent detectability. It relies on having a definitive diagnosis on which to base the performance of image interpretation. The method consists of determining the true-positive and false-positive rates at different criterion levels. The true-positive rate is the fraction of positive images correctly identified as positive by the observer. The false-positive rate is the fraction of negative images incorrectly identified as positive by the observer. The result will be constructed on a graph (ROC curve), as a plot of true-positive rate against false-positive rate and each point on the curve corresponds to a different criterion level. Therefore, the ROC analysis can be used in assessing the success of an image processing technique in improving detectability of abnormalities.

1.7.2.2 Contrast-to-Noise Ratio

The ability to distinguish features within a nuclear medicine image depends on differences in uptake of radioactivity. The detectability of that feature will depend on the contrast between the counts in the feature compared to that in the surrounding count. Image contrast refers to the differences in density or intensity between areas of the imaged object containing different concentrations of radioactivity. Since the physical processes of gamma photon emission are random in nature, the information density (the number of counts recorded per unit area of the image), can be subject to random statistical variations in counting rate (random noise). It is known that there is noise in the image and this will influence how well features will be seen. In order to detect a region of any size in an image, it would have to distinguish it from random noise fluctuations in the image. Increasing noise makes features more difficult to identify.

Image contrast is the difference between the surrounding activity and the average count in the object. It is reduced by background and scatter. A region in an image

will generally be surrounded by radioactivity, so that in a planar imaging a background count is added to the image. Background is the overlying and underlying activity that contributes to the number of counts in a region of interest. Thus even when there is no activity in a feature in the body there will be counts detected at the corresponding area in the image leading to a decrease in contrast of visualisation of features. Image contrast can also be reduced by scattered radiation, leading to a decrease in the visibility of all the features in the image.

Detectability depends on both contrast and noise. Therefore image detectability can be measured by contrast-to-noise ratio. It is an objective measure used as a criterion of assessing how well a particular objects can be visualised. The parameter calculated is known as a 'Figure of Merit' (FOM), of visual detectability of detail in an image (Herman et al 1989, Furuie et al 1994).

1.8 Applications of Nuclear Medicine

The nuclear medicine images which are produced from the distribution of the radionuclides within the body have different applications, which are useful for diagnostic purposes. The images produced are usually planar images of the accumulation of the radiopharmaceutical in the organ of interest. In bone imaging for example, a compound named MDP (methylene-diphosphonate) can be labelled with ^{99m}Tc and injected intravenously into the patient. The radiolabelled compound will localise in bone, areas of rapidly growing bone taking up more of the compound than other areas. In detecting the increased activity in the localised area, by using gamma camera, a clear image of the lesion will be obtained, such as fractures, tumours or healing bone.

A sequence of images can also be obtained displaying the changes in the tracer distribution with time. In renal scan for example, ^{99m}Tc is attached to a compound named DTPA (diethyltriamine-penta-acetic acid), which is rapidly excreted by the urinary system to image the kidneys and measure their function.

A very large number of similar tests exist assessing the function of many organs. In general, morphology and structure of certain organs are best studied using other modalities techniques; such as x-ray computed tomography (CT scan) or magnetic resonance imaging (MRI). However, the information obtained from nuclear medicine radionuclide images are useful diagnostic tool, since the ability of an organ or tumour to take up a radiopharmaceutical is related to its function.

Another method of nuclear medicine imaging is single photon emission computed tomography (SPECT). In this a series of images will be acquired by rotating a gamma camera around the patient. The images obtained are used for the production of a three dimensional image (multi-cross-sectional images) of the distribution of radioactivity. The images produced will give more detailed information, of a better contrast images. e.g., in brain and cardiac imaging (MacIntyre et al 1994). The role of imaging in nuclear medicine has also developed with a new technique of positron emission tomography (PET). The technique provides a unique information on regional tissue physiology. It enables physiologically important elements such as ^{11}C, ^{13}N, ^{15}O, and ^{18}F to be used for radiolabelling and to measure regional blood flow and a variety of metabolic processes. Nuclear medicine images have lower quality than other medical imaging techniques and therefore, any improvements brought about by image processing could be of value.

1.9 The Proposed Work

The radioactivity that can be administered to the patient in radionuclide imaging is limited, by consideration of patient radiation protection, in that it must not give rise to an unacceptable risk of detriment to the patient. In the United Kingdom ARSAC (Administration of Radioactive Substances Advisory Committee), defines the maximum recommended radioactivity for each type of study and also explain the legislation relating to the administration of radioactive substances (Notes for Guidance... 1998). This will have an effect on the quality of the images produced, by limiting the number of gamma photons detected within an acceptable imaging time. Image quality is also degraded by the physical processes in the imaging system.

Image processing might improve this situation and it is important, that the technique used is capable of dealing with a situation of high noise in the image. The hypothesis to be tested is that image processing should improve the image quality of any given image.

The maximum entropy data processing technique, has been found to be useful as a powerful and generally applicable image processing method for reconstructing images from noisy and incomplete data (Gull et al 1978, Gull and Skilling 1984, Livesey et al 1985, Skilling 1991). It uses knowledge of the available image data and the point spread function (PSF) of the imaging device to give an improved image quality. The maximum entropy deconvolution technique (Gull 1989, Daniell 1991), has been developed to solve the problem of processing nuclear medicine planar images (Simpson et al 1995). It showed an improvement in image quality assessed by several criteria. However, the technique requires further development to make it robust for routine clinical use. Therefore, the proposed work is going to be performed according to the following plan of investigation:

(1) Optimisation of the technique:
Operation of the processing technique requires several parameters to be set up manually. These values must be correct for optimal performance of the processing. Therefore, a variety of different phantoms will be studied and the optimum parameters will be chosen by studying the figure of merit (FOM) of the quality of the images.

(2) Experimental evaluation of the technique:
To evaluate maximum entropy technique in a phantom study, using ROC analysis as a subjective assessment for detectability. The aim will be to demonstrate improved performance using maximum entropy or equivalent performance using a lower count processed image.

(3) Clinical evaluation in planar images:
With a positive outcome obtained from the experiments, an evaluation of the maximum entropy technique was made in a nuclear medicine clinical study, using

ROC analysis. In this part of the project, experienced nuclear medicine clinicians and nuclear medicine physicist were used as the observers to interpret both processed and unprocessed nuclear medicine planar images.

This thesis will determine the efficacy of the maximum entropy technique in improving image interpretation. It is hoped that the clinical benefits will be (i) improved diagnostic accuracy (ii) reduced imaging time resulting in improved cost effectiveness of the service or (iii) reduced radiation dose to the patient.

Chapter Two

Image Processing in Planar Nuclear Medicine Imaging

2.1 Introduction

Nuclear medicine images suffer from poor quality that arises from different factors, which have already been mentioned in section 1.6. Image processing techniques might be used to overcome this problem by transforming the acquired data to an improved representation of the physical distribution of activity. In this chapter an introduction to image processing is provided with particular emphasis on maximum entropy processing as applied to planar nuclear medicine images.

2.1.1 The Image Formation Process

In image formation, the ideal planar image is a projection (a two dimensional representation) of the three-dimensional distribution of radioactivity. However, in practice a perfect image is not obtained, due to the effect of several processes (see chapter one). Degradation due principally to attenuation, blurring and noise causes the real image (data) to be of poorer quality than the ideal one. As mentioned in chapter one, attenuation groups together the loss of photons from absorption and Compton scatter. The blurring has contributions from intrinsic resolution of the gamma camera, the imperfect nature of the collimator geometry and Compton scattered photons accepted by both collimator and energy window. Attenuation and

blurring are complicated, interdependent effects dependent on the shape and size of the patient and the distribution of activity. Blurring increases the number of data elements influenced by each element of the activity distribution. As the degree of the blurring depends on the depth of the emitting radioactivity, the description of the image formation process in two dimensions requires an approximation to be made (Simpson et al 1995). An average depth for the activity is assumed so that the acquired image (data), d(x,y), can be considered as a convolution of the ideal image or map m(x,y) with a point spread function (PSF) p(x,y) (Figure 2.1). This point-spread-function is the response of the system to a point of radioactivity at some average distance from the camera through an average thickness of scattering material. The Poisson noise can be considered an additive function. Therefore the image formation process is described mathematically as:

$$d(x,y) = m(x,y) \otimes p(x,y) + n(x,y) \qquad (2\text{-}1)$$

where $\otimes$ represents the two-dimensional convolution process and n(x,y) is the noise.

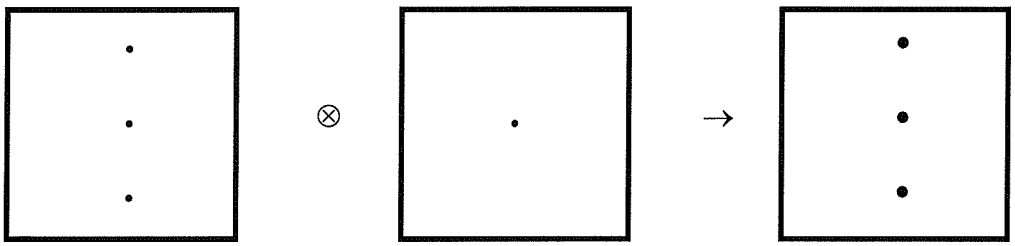

Figure 2.1: Convolution process blurring the real image distribution by the point spread function.

2.1.2 The Principle of Image Restoration

In general any data processing problem can be thought of as a mathematical transform from the physical quantity wished to be determined (map, **m**) to the actual measurements (data, **d**). In the image processing example the data is the acquired image and the map is the processed image.

If the transform from map to data is linear, it can be described thus as,

$$d_k = \sum_{i=1}^{N_{map}} R_{ik} m_i \qquad k = 1, N_{data} \qquad (2\text{-}2)$$

where d_k is the data, m_i is the map (the conclusions or the set of values we wish to determine) and R_{ik} is the transform matrix. N_{data} and N_{map} are the number of elements in the map and data respectively. For image processing N_{data} and N_{map} are equal. This linear relationship may be complicated but, with knowledge of the system, it can be determined. The goal in processing the data is to use it to gain as much information as possible about the underlying distribution.

The above equation assumes the data to be noiseless, but as stated in chapter one noise is influenced in an image by certain factors. Thus it can be considered as an additive factor (n_k) to the image, therefore:

$$d_k = \left(\sum_{i=1}^{N_{map}} R_{ik} m_i \right) + n_k \qquad k=1,N_{data} \qquad (2\text{-}3)$$

The aim of image restoration is to recover the ideal image as closely as possible. This is done by attempting to solve equation (2-1) for m(x,y). This process is known as deconvolution. It is the inverse of convolution and the process is often referred to as the inverse problem (Figure 2.2).

Image restoration involves the derivation of the map from the data and is therefore the inverse of the image formation process;

$$m = R^{-1} d \qquad (2\text{-}4)$$

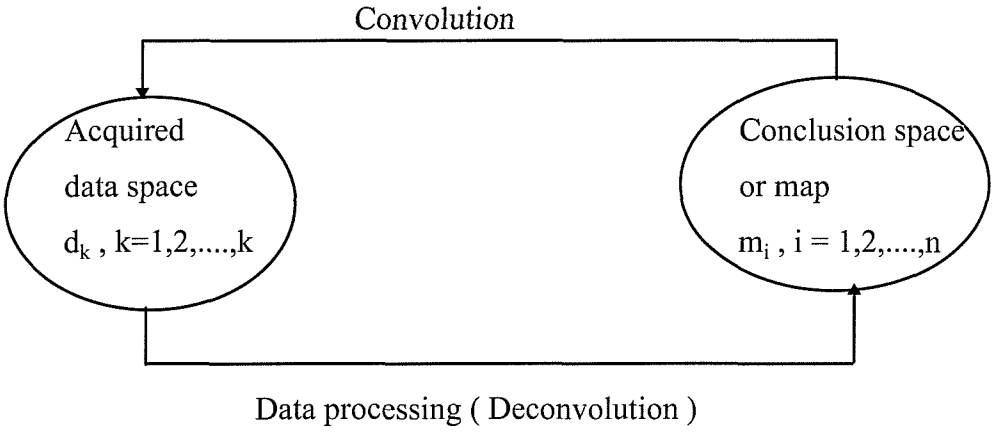

Figure 2.2: Image processing theory.

The requirement is to calculate the real distribution, **m** (ideal image) from the data, **d** and the point-spread-function, **p** which are known. The process of deconvolution is a complicated problem but can be simplified by using the Fourier Transform. This transforms the convolution equation to become a simple product, therefore, equation (2-1) will become;

$$\mathcal{D}(u,v) = \mathcal{M}(u,v) \cdot \mathcal{P}(u,v) \qquad (2\text{-}5)$$

where $\mathcal{D}(u,v)$, $\mathcal{M}(u,v)$ and $\mathcal{P}(u,v)$ are the Fourier transforms of d(x,y), m(x,y) and p(x,y) respectively, u and v are spatial frequencies in the x and y directions respectively. Since our data contains noise, n(x,y) it is included in the data, thus equation (2-5) will become;

$$\mathcal{D}_1(u,v) = \mathcal{M}(u,v) \cdot \mathcal{P}(u,v) + \mathcal{N}(u,v) \qquad (2\text{-}6)$$

where $\mathcal{Q}_i(u,v)$ represents real noisy data.

The noise being random is unknown but successful solutions have to make allowance for it. Its presence means that there are many distribution maps that are consistent with the data and the image reconstruction problem is how to select the best of these maps. Many different approaches have been used with varying levels of success. Maximum entropy has the ability to determine the most probable solution to such a problem and therefore its application to restoration in radionuclide imaging is worthy of investigation.

2.1.3 Techniques for Image Restoration

2.1.3.1 Filter Techniques

Image filtering offers a great potential for improving image quality. It is used in processing of images either to enhance a particular image feature such as the edge of a structure or to remove statistical noise (Ott et al 1988). It involves first Fourier transformation of the image to its spatial frequency components. Each of these components is multiplied by a weighting factor (the filter) and the inverse Fourier Transform is applied to convert this filtered data back into an image in real space.

Smoothing filters are used for reducing noise in images. Since noise in nuclear medicine images is most evident at high spatial frequencies, these filters are designed to attenuate high frequencies while sparing low frequencies (Sharp et al 1985). However reducing the effect of noise also reduces contrast of the image and thus the signal to noise ratio may not be maximised (Tanaka et al 1970).

Image restoration involves use of a filter enhancing the high frequency components that have been lost by the blurring of the imaging process. The problem with this approach is that the noise at these frequencies is also enhanced.

A number of different digital filter methods have been formulated in an attempt to produce optimum restoration of the inherent image quality lost during the imaging process while at the same time suppressing the noise (Andrews et al 1977, Pratt 1978, Castleman 1979). One of these methods uses the Wiener filter (King et al 1983). This approach assumes that the imaging system is linear and stationary and that the noise is additive with constant variance and uncorrelated with the object (Andrews et al 1977, Pratt 1978, Castleman 1979). With these assumptions the Wiener filter is derived as a filter which minimises the mean-square error between the original object and the restored image of the object (Andrews et al 1977, Pratt 1978, Castleman 1979). Its major problem is that it requires rather detailed knowledge of the object and noise and the blurring process (King et al 1983). Other techniques of filtering the image in a way which attempt to recover some of the resolution but also to minimise the noise have also been described (King et al 1984).

2.1.3.2 Iterative Techniques

An iterative technique is a process of successive approximations used for solving a mathematical problem. In image processing it is often used to carry out deconvolution. Its method (Figure 2.3) is to make an initial guess of the map by, for example, setting each image pixel count to the mean pixel count (total counts/total number of pixels) and then to use an iterative procedure to alter this map gradually by comparing the corresponding expected image data at each iteration with the actual raw data projections (Webb 1988). The expected images are calculated using knowledge of the physics of the image formation process, in the planar imaging case using convolution as described above.

One of the methods which is commonly used is **Maximum Likelihood Expectation Maximisation** (MLEM). The MLEM algorithm increases in every iteration the likelihood that the image estimate generated the measured data. The values in the images are constrained to stay positive. However, noise is uncontrolled when using MLEM and it increases with increasing iteration number. As the expected data gets closer to the actual data than the noise level, features appear in the solution which

are due solely to noise (Liang et al 1989, Green 1990, Herbert and Gopal 1992, Lalush et al 1992). Techniques have been described to avoid this problem using various smoothing constraints (Tsui et al 1991). The method has been extensively applied to SPECT reconstruction.

Another iterative method which is the main concern in this thesis is the **Maximum Entropy technique**. It has been applied to different image processing problems (Daniell 1991, Skilling 1991) and has proved very successful in handling noisy and incomplete data (Gull et al 1978, Gull et al 1984, Livesey et al 1985). It can be used to deconvolve the planar images with a point spread function. The idea of the maximum entropy technique is to select the most probable solution from all those which are consistent with the data considering the noise present. It is an iterative technique, starting from an input trial map and updating it until it converges on the maximum entropy solution. It has already been shown to give improved image quality in planar imaging (Simpson et al 1995).

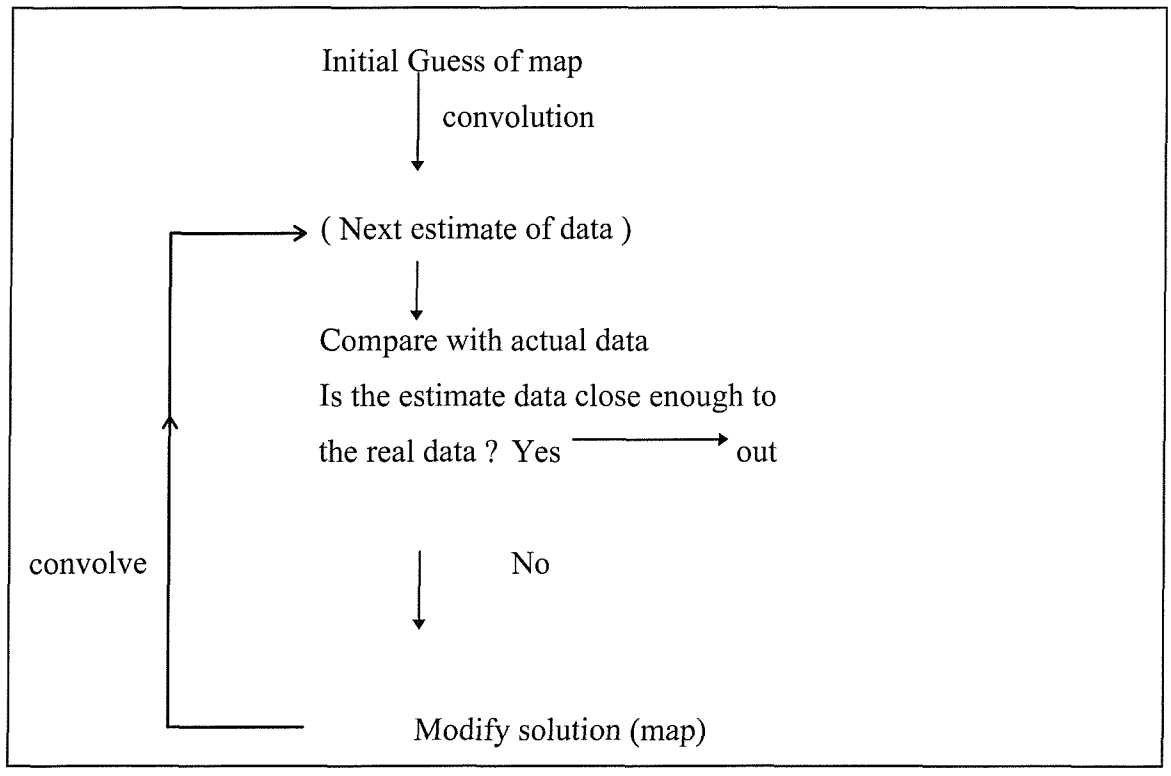

Figure 2.3: Description of the iterative process.

2.2 The Principle of Maximum Entropy

2.2.1 Baysian Interpretation

The maximum entropy technique is based on Bayes theory, which updates the probability of a conclusion based on new data (Cox 1946). Bayes theorem can be applied in different conditions where conclusions can be drawn depending on uncertain data. Bayes theorem can be stated that the probability of a conclusion or map, given the measured data is :

$$\text{Prob(conclusion\data)} \propto \text{Prob(conclusion)} \times \text{Prob(data\conclusion)}$$

The notation Prob(A\B) denotes the "Probability that A is true, given that B is true". In maximum entropy, the prior probability of a given distribution of activity is related to entropy. So the term Prob(conclusion) is the prior probability of the conclusion before measuring the data. The probability of the data can be calculated given an initial map knowing the PSF and knowing the data error. Then the term Prob(data \ conclusion) is known as the likelihood, measuring the probability of the data given a set of conclusions. The term Prob(conclusion\data) is called the posterior probability of the conclusions given the collected data. That can tell us how to change our conclusions based on the data.

2.2.2 Maximum Entropy Approach

2.2.2.1 Consistent Conclusions

The approach of Maximum Entropy uses the forward, conclusion to data, transform in solving the problem of the inverse transform. Maximum entropy will then choose the conclusion which is the most probable solution (i.e., choosing the conclusion which has the maximum probability).

In a perfect imaging system this transform is stable, thus given any set of conclusions or map m, it is possible to generate the noiseless data, g expected from the system in the absence of random errors,

$$g_k = \sum_i R_{ik} m_i \qquad (2\text{-}7)$$

where R_{ik} is the transform from map to data. If a conclusion or map **m** were the true underlying distribution, and noise in each datum (pixel) d_k was Gaussian with standard deviation σ_k then, on average, each noiseless datum g_k would be one standard deviation from the corresponding d_k.value.

2.2.2.2 χ^2-test

Thus if **m** were the perfect solution, the χ^2 statistic for g and d :

$$\chi^2 = \sum_{k=1}^{N_{data}} \left(\frac{d_i - g_i}{\sigma_i} \right)^2 \qquad (2\text{-}8)$$

would, on average, give a value of N_{data}. The χ^2 statistic is introduced as a test to provide a mean of judging whether a trial solution (map) is consistent with data (Press et al. 1992). Thus, for consistent solutions χ^2 must be equal to the number of data points N_{data}.

2.2.2.3 Entropy

There are a large number of different trial solutions (map) which are consistent with data. A criterion which can help us choose between these consistent conclusions is needed. Maximum entropy is an example of such a criterion giving the solution with

the highest entropy solution which is therefore the most probable of these consistent solutions (Skilling 1988, Daniell 1991). Entropy is used as a criterion to choose between solutions which satisfy all the data constraints. The entropy **S** as a property of our conclusion **m**, can be defined as follows;

$$S = -\sum_{i=1}^{N_{map}} m_i \log(m_i / b) \qquad (2\text{-}9)$$

where m_i are the different levels in the map, and b is a constant (i.e., the default solution) whose effect on the algorithm will be described in the next section.

2.2.2.4 The Maximum Entropy Algorithm

The maximum entropy algorithm is an iterative process. At each iteration both χ^2 and entropy S, are calculated and the new estimate of the distribution is calculated based on gradients of χ^2 and entropy with respect to the solution values. The algorithm searches for the conclusion, which fulfils the constraint $\chi^2 = N_{data,}$ and has the highest entropy.

The method requires the definition of a default level for the solution. This is usually taken as the most desirable value of the solution in the presence of poor data. This affects the constrained optimisation, pushing the solution towards this value. This leads to a distortion of the total count in the solution, tending to reduce total counts for the conclusion which is less than the mean of the data and increasing them for the one which is more than the mean of the data. This distortion was overcome (Simpson et al 1995) by changing from a uniform default level **b** to a nonuniform default level $\mathbf{b_i}$, modifying equation (2-9) to be,

$$S = -\sum_{i=1}^{N_{map}} m_i \log(m_i / b_i) \qquad (2\text{-}10)$$

The default solution b_i was obtained by making it a smoothed version of the original data, i.e. a convolution with some blurring function. It was achieved by repeatedly performing a nine-point smooth with weights 4, 2 and 1 (Lieberman 1977, Simpson et al 1995).

2.3 Practical Considerations of Applying Maximum Entropy

As mentioned earlier, for a particular maximum entropy problem several parameters need to be specified. The definition of these parameters is now discussed in detail.

2.3.1 Number of Iterations

It has been found (Simpson et al 1995) that the algorithm usually converges and gives each maximum entropy solution in approximately 6 iterations. Sometimes however the algorithm will produce sensible solutions with a larger number of iterations. In other situations the algorithm does not converge and therefore a maximum number of iterations has to be set to avoid the algorithm iterating for ever.

2.3.2 Definition of Errors

Since the χ^2 statistic is introduced (equation (2-8)), as a constraint in testing the consistency of a conclusion with the data, an estimate of expected errors is needed in its evaluation. The best estimate of the error datum d_k is a standard deviation of data point, σ_k.

Since the data comes from the radioactive emission process which is random, the errors will follow a Poisson distribution where,

$$\sigma_k = \sqrt{d_k} \qquad (2\text{-}11)$$

This allows an estimate of the standard deviation to be made. However, it has been previously found (Simpson et al 1995) that the algorithm did not converge with standard deviations calculated as above. This was considered to be due to the presence of systematic sources of errors: such as background error, and imperfections in the model. These systematic errors are difficult to quantify. Therefore, they were included in the model by introducing two parameters (C_1 and C_2) as constants in the standard deviation calculation. The error is then estimated using the following modified equation:

$$\sigma_k = C_1\sqrt{d_k} + C_2 \qquad (2\text{-}12)$$

The choice of C_1 and C_2 have an effect on the convergence of the algorithm and the properties of the solutions produced. Therefore these parameters must be correct for the optimal performance of the processing.

2.3.3 Definition of Default Solution

The default solution ($\mathbf{b_i}$) specifies the initial trial map for the algorithm for the first iteration. It specifies the solution that maximum entropy should produce when the data is so poor as to provide no constraint on the algorithm i.e., as to provide little or no information. A low constant value may be used as a default solution to minimise the occurrence of false positive interpretations of the solution. However in our

application of maximum entropy the default solution $\mathbf{b}_i$ has been made (Simpson et al 1995) a smoothed version of the original data **d**, (i.e., a convolution of **d** with some blurring function), to enable the total counts in the image to be maintained. The degree of smoothing used for the default solution will also influence the final conclusion and therefore this is another parameter requiring optimisation in the practical application of the technique.

2.4 Summary

In this chapter the image formation process has been considered to address the problem that affect the production of nuclear medicine image quality. Furthermore the principle of image restoration of this noisy and incomplete data has been considered. Different techniques for image restoration were mentioned and presented the maximum entropy technique as a possible approach to solve this problem.

Chapter Three

Investigations on the use of Maximum Entropy in Planar Radionuclide Imaging Deconvolution

3.1 Introduction

3.1.1 Previous Work

An investigation has been previously performed to evaluate the maximum entropy technique (Simpson et al 1995). The investigation studied one phantom as a test object. The phantom used was a planar source. Images of the phantom were obtained to investigate the effect of parameters C_1 and C_2 (Chapter 2 section 2.3) on image quality and evaluate the improvement in image quality obtained. The result showed that the convergence of the algorithm and the quality of the images depended heavily on the values of the error parameters C_1 and C_2. The technique was found to produce solutions close to the optimum over a wide range of error parameters C_1 and C_2 , although the values of C_1 and C_2 varied considerably with the number of counts in the image.

3.1.2 Summary of Proposed Work

The purpose of the work described in this chapter was to investigate thoroughly the parameters defining the errors on each data point, and also the default solution which is the most desirable solution in the presence of poor data. The aim is to find out how to define the errors and default solution to give the best solution. The performance of maximum entropy was also compared to the use of conventional smoothing and a technique using a combination of both maximum entropy and smoothing.

3.2 Investigation of the Validity of the Error Model

If the result of measuring the number of counts is N, it is known in theory that the error as estimated by the standard deviation of the counts, σ will be equal to $\sqrt{N}$. However, as has been mentioned earlier when this estimate is used in maximum entropy processing the algorithm doesn't converge. Therefore an experiment was carried out to confirm the validity of the error model.

3.2.1 The Aim of the Experiment

To prove that, the standard deviation of measured counts is equal to the square root of the count, for all count rates.

3.2.2 Method

A rectangular source (58 × 44 cm) containing a uniform activity of Co-57 (100MBq) was imaged using a Genesys dual-headed gamma camera (only one head is used) with a low energy general purpose collimator (ADAC, Milpitas, CA). A planar dynamic study was acquired with a short time per image (0.1 sec/frame), at 128 ×

128 matrix size. The acquired images were transferred to a Sun SparcStation2 to perform the processing. By summing different numbers of frames from the dynamic study, images of a uniform source with average count per pixel varying between 0.05 and 5.1. were created. A rectangular region of interest was drawn to cover the largest possible area while avoiding getting too close to the edge of the field of view of the camera. The PICS Program (Fleming et al 1991) was used to calculate the mean (N) and experimental standard deviation σ_e count per pixel. The expected standard deviation was calculated as $\sqrt{N}$, and compared to the measured standard deviation. The paired t-test was used to determine the significance of the differences between the experimental standard deviation and the theoretical standard deviation.

3.2.3 Results and Discussion

The experimental standard deviation for the acquired data was similar to the theoretical standard deviation (Figure 3.1a). The t-test proved that there was no significant difference between the experimental standard deviation and the theoretical standard deviation (P = 0.1). That was confirmed when the difference between both methods was plotted against the average (Figure 3.1b) (Bland and Altman 1986).

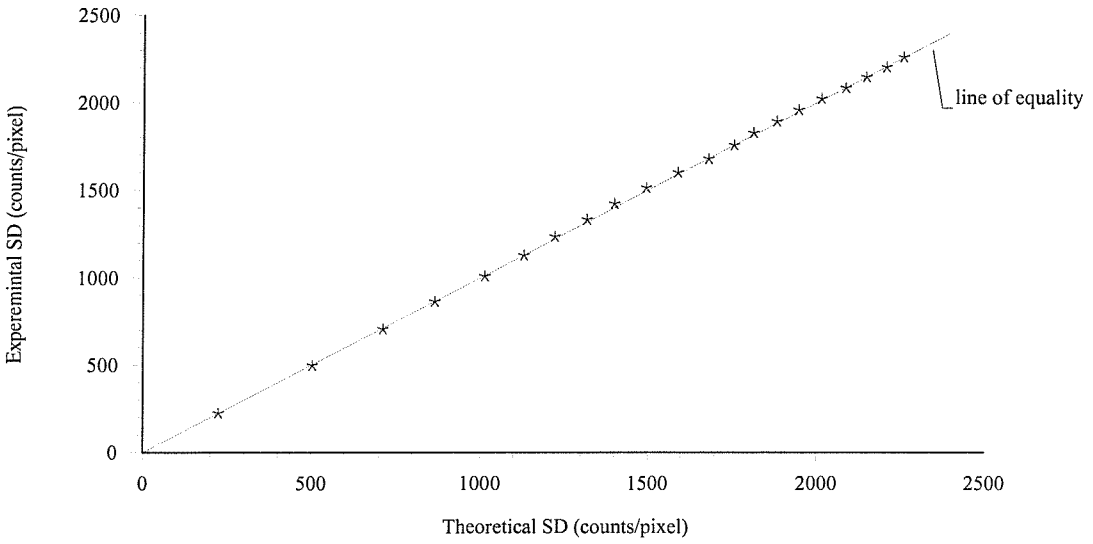

Figure 3.1a: A comparison between the assessment of the standard deviation theoretically and experimentally. The straight line is the line of equality.

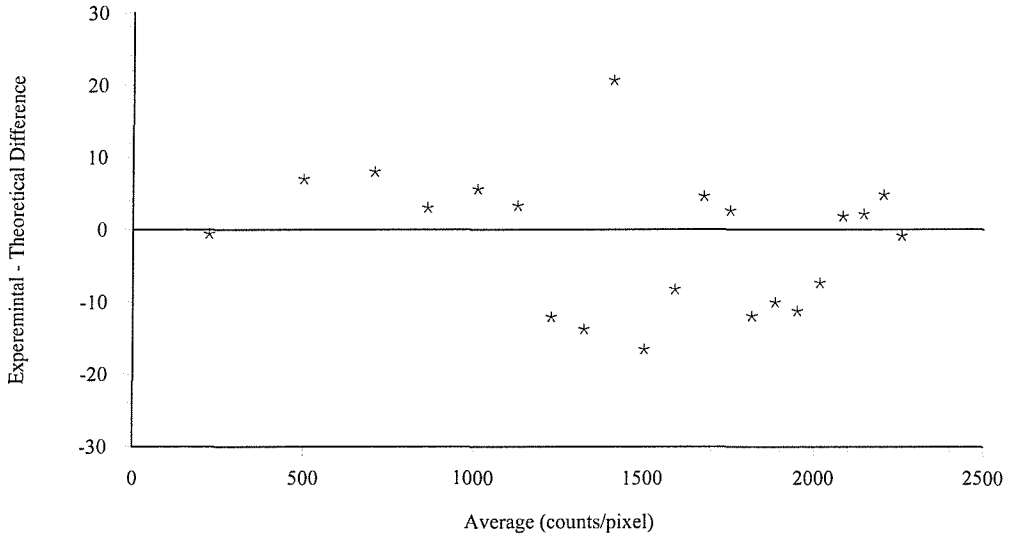

Figure 3.1b: Difference versus mean for the assessment of the standard deviation measured theoretically and experimentally.

The result of the experimental measurements on the gamma camera shows that the error is equal to $\sqrt{N}$ even at low count. This confirms the relationship expected from Poisson statistics. However the maximum entropy algorithm doesn't converge when using this error. That could be due to different sources of the errors. Although it has been confirmed that the theoretical estimate of the standard deviation of counts is correct, the distribution will be asymmetric at low counts as it follows the Poisson distribution. The current algorithm which uses χ^2- statistic does not take this into consideration and this could be a source of the problem of non-convergence. To correct for this would require a major revision of the algorithm and is beyond the scope of the thesis.

A further problem arises from using the actual measured count to estimate the error. With the Poisson distribution estimating the error from the square root of N is probably quite accurate at high counts, however, when it gets to very low counts (e.g., zero or one count) it results to a fallacious estimate. It is common in nuclear medicine images to have a significant number of pixels which have no counts. For these pixels the error is estimated at zero and this is clearly wrong.

In future work the intention is to deal with the problems at zero and low counts by using an iterative adjustment of errors. The process will be to create an initial maximum entropy image from which it can get a better estimate of the error. Then the new errors can be applied on another application of maximum entropy and iteratively improve the image.

3.2.4 Conclusion

The investigation of the validity of the error model proved that the assumption that the standard deviation of count is given by the square root of the count even at a very low count. However this does not imply that it is correct to estimate errors from measured counts at low count rate and improvement in the error model is the subject of current research (McGrath et al 1998). This will attempt to solve the low count error estimation by using an iterative adjustment of errors. The problem of an asymmetric distribution of error is a further problem in applying maximum entropy which is beyond the scope of this study.

3.3 Choice of Parameters for Assessing Image Quality

The aim of using the maximum entropy technique in nuclear medicine is to give an improved representation of image quality to aid in clinical decision making. The main concept of maximum entropy processing is to choose the optimal image for a given set of values for data, experimental errors and default solution. The best method of evaluating any technique is to test how successfully it aids performance of the task for which it is required. In the case of image quality this would be how well it allows clinicians to precisely identify and make their decision on any features in the image. As has been mentioned (see chapter 1), the receiver operating characteristic (ROC) analysis can be used to assess image performance. However for choosing the optimal parameters needed by the algorithm, ROC assessment is obviously laborious and time consuming. It is more convenient to use a measurable quantity of the image itself which can be related to observer performance. Image

quality can be assessed conventionally by measures of contrast, resolution and noise. Image processing techniques, however, often improve one aspect of image quality at the expense of another and therefore it is useful to use a single measure to express quality. Therefore a Figure of Merit (FOM) has been used, as a mathematical parameter to measure image quality (Herman et al 1989). The Figure of Merit is an objective measure of image quality, which doesn't depend on someone's opinion. It is considered to be related to the ability of an observer to detect an object on a uniform background in ROC analysis.

The general approach of the experiment is to vary the various parameters used by maximum entropy, and make corresponding measurements of the quality of the images produced and in this way to find the parameter values providing optimal image quality.

The figure of merit can be defined by calculating the number of pixels, mean and variance of a region in the image representing an object and the corresponding values for the surrounding background. Its incorporates both the contrast between object and background and the noise. There are various methods of calculating the figure of merit, and these are discussed in detail in the next section.

The FOMs do not directly include a consideration of resolution. However for small objects at the threshold of detection the measured contrast is closely dependent on resolution. The FOM, therefore, effectively includes the influence of resolution.

3.3.1 Description of Different Figure of Merits (FOMs)

Three methods of calculating the figure of merit which have been previously described are considered. Essentially they are contrast to noise ratios, but they are slightly different in expression. The three different figures of merit have been named as, FOM1, FOM2 and FOM3. They can be described in the following equations as follows:

The First equation,

$$FOM1 = \frac{\sqrt{n_o n_b}(m_o - m_b)}{\sqrt{n_o \sigma_o^2 + n_b \sigma_b^2}} \qquad (3\text{-}1)$$

where n_o, m_o and σ_o^2 are the number of pixels, mean and variance of the object region in the image, and n_b, m_b and σ_b^2 are the corresponding values for the surrounding background.

This equation has been used previously by Simpson et al 1995. It incorporates the contrast (m_o - m_b) and the noise in both the object and surroundings.

The Second equation,

$$FOM2 = \frac{\sqrt{n_o}(m_o - m_b)}{\sigma_b} \qquad (3\text{-}2)$$

This is the classical contrast to noise ratio (Chesters M S 1992) using only the noise in the background. The $\sqrt{n_o}$ is introduced to allow the FOM to reflect the greater detectability of larger objects.

This is the equation which will be used for this study, the reason for which will be explained in detail below.

The Third equation,

$$FOM3 = \frac{\sqrt{n_o n_b}(m_o - m_b)}{\sqrt{\sigma_o^2 n_b + \sigma_b^2 n_o}} \qquad (3\text{-}3)$$

This equation gives statistical measure of the significance between two means, based on the z-statistic. It therefore gives a measure of the statistical significance of the object having a different count from the background.

Since the concern is visualising a particular object to help in decision making, the figure of merit which will be used must be related to image detectability (Chesters 1992, Simpson et al 1995). FOM1 and FOM2 have previously been related to detectability of objects (Simpson et al 1995), FOM3 has not formally been related to

detectability but it is interesting to note the similarity of this statistical formula to the other proven FOMs.

In the following paragraph there will be a brief discussion on how the three figures have been calculated and why the FOM2 have been chosen for this study.

In a previous study by our group FOM1 had been used in calculating the detectability. The surrounding background noise was assessed as the standard deviation of pixel count in the surrounding background region. However it was noticed that when changing the size of the surrounding background on the same image, the value of FOM1 will vary. This makes it difficult to compare the results when measuring and comparing different phantoms. FOM3 also depended on the area of the background region and therefore has the same disadvantage. Thus the FOM2 has been used, as its calculation is independent of the value of the surrounding background size.

An alternative and more complete way of comparing quality of solutions was to use contrast to noise plots and these are also used extensively in describing the results.

3.4 Defining the Optimal Parameters for Maximum Entropy Processing in Planar Radionuclide Imaging

3.4.1 Phantom Measurements

The three physical phantoms which were measured as test objects are called the Williams phantom, Fleming phantom and Goddard phantom. All the phantoms (Figure 3.2) have been imaged through 4.6 cm of scattering material.

The Williams phantom is a flat perspex container of dimensions 23.8 × 16.9 cm, with parallel faces 0.9 cm apart. In between the faces it contains four circular recesses and four perspex pillars, of differing diameters, (0.5, 1.0, 2.0, and 4.0 cm).

It is filled with a radioactive material and viewed by a gamma camera as a planar source. The phantom image appears as an area with a uniform activity with the four circular recesses appearing as hot spots with double activity and the perspex pillars appearing as cold spots with no activity.

The Fleming phantom is a flat perspex container of dimensions 10 × 10 cm, with four perspex pillars, of differing diameters (0.25, 0.5, 1.0, and 2.0 cm). When this phantom was filled with a radioactive material and imaged by gamma camera, it showed a uniform area with four cold spots, representing the four perspex pillars.

The Goddard phantom also is a flat perspex container 34 × 34 cm dimension, containing 12 circular recesses and 12 perspex pillars, of differing diameters, (0.5, 1.0, 2.0 and 4.0 cm) and differing depths. This gave a series of hot and cold spots differing in both size and contrast.

All the three phantoms images were obtained using one head of a Genesys Dual-headed Gamma Camera with a low energy general purpose collimator. A dynamic study was acquired with a frame time of 5.0 seconds, at 128 × 128 matrix size (pixel dimension 0.467 cm). The acquired study was transferred to a Sun SparcStation2, to perform the processing. Images with a variety of counts was created by summing different numbers of frames. The maximum entropy program was used in processing the planar images of the phantoms.

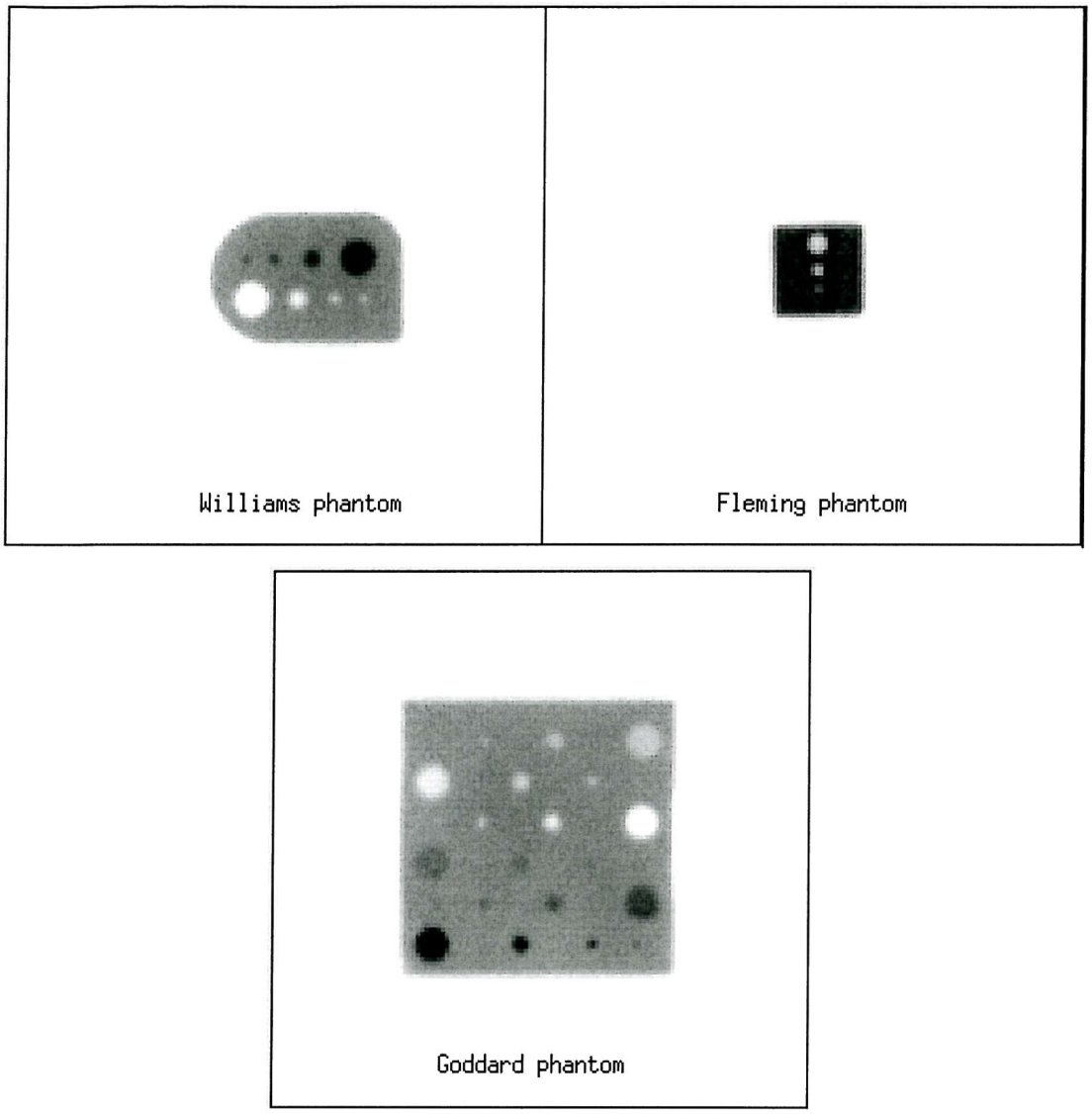

Figure 3.2: Images of the three physical phantoms, which are used as test objects.

3.4.2 Defining the Optimal Number of Smooths for the Default Solution

3.4.2.1 Method

A default solution is required by the algorithm for the purpose of providing an initial trial map for the first iteration and specifies the solution in the presence of poor data. Previous work showed that a smoothed version of the original data could be used as the default. The purpose of this experiment was to investigate how the degree of smoothing affected the quality of the maximum entropy processed images. The three phantoms (Figure 3.2) were used in this test. The 2.0 cm cold spot was chosen as the feature to be studied and a region was drawn around it and a background region in a selected area in the surroundings. Then 1, 2, 5, and 12 passes of a smoothing filter were used as default data. The filter applied was one commonly used for smoothing radionuclide images in which each pixel is replaced by a weighted sum of itself and the eight surrounding pixels with the following weighting scheme (kernel):,

1	2	1
2	4	2
1	2	1

These different defaults were tested with varying the error parameters C_1 and C_2, to select the optimal number of smooths for use as default data. The maximum entropy solutions, using each of the default data were obtained and compared to the original acquired data. Contrast and noise measures were used for the calculation of the image quality as follows,

$$\text{Contrast} = m_o - m_b \qquad \text{and} \qquad \text{Noise} = \sigma_b$$

where m_o and m_b are the mean count per pixel in the object and the surrounding background region respectively, and σ_b is the standard deviation of counts per pixel in the uniform area surrounding the object.

The PICS Program (Fleming et al 1991) is used to calculate the image quality which results from each solution using the FOM2 described above.

3.4.2.2 Results and Discussion

The result shows that using different levels of smoothing as default data gives varying solutions. For each level of smoothing a range of solutions was produced starting from a high contrast, high noise solution going down to a low contrast low noise solution (Figure 3.3). The different solutions were produced by varying the error parameter C_2 with C_1 at a constant value of 1.0 . The point representing the raw image is presented for comparison.

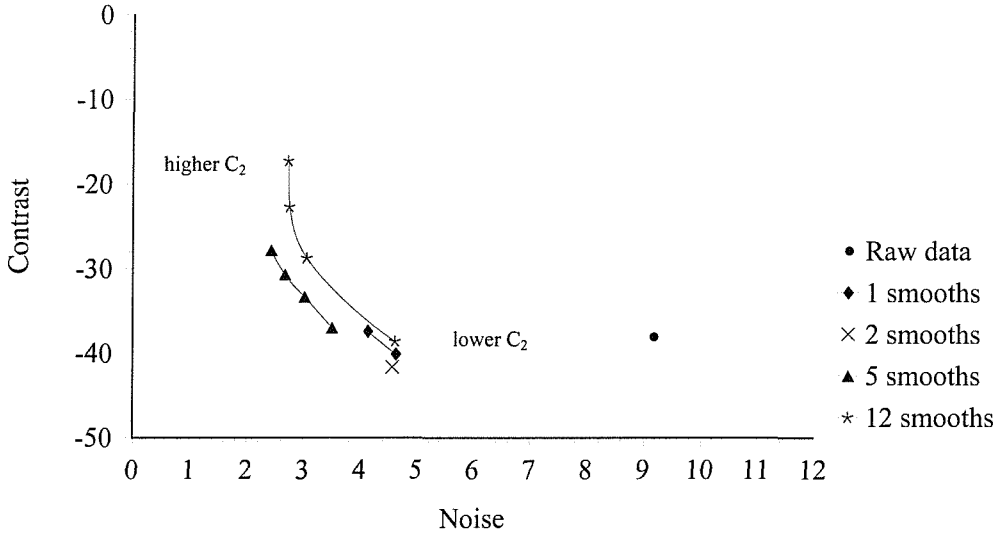

Figure 3.3: Maximum entropy solutions using a fixed value of C_1= 1.0 and varying the number of smooths used in the default solution. The image used was a Williams phantom with a total count of 108k.

The optimum figure of merit was obtained with a default solution of 5 smooths (Figure 3.4). A similar result is produced when investigating the same object using a lower values of C_1 (Figure 3.5a and 3.5b).

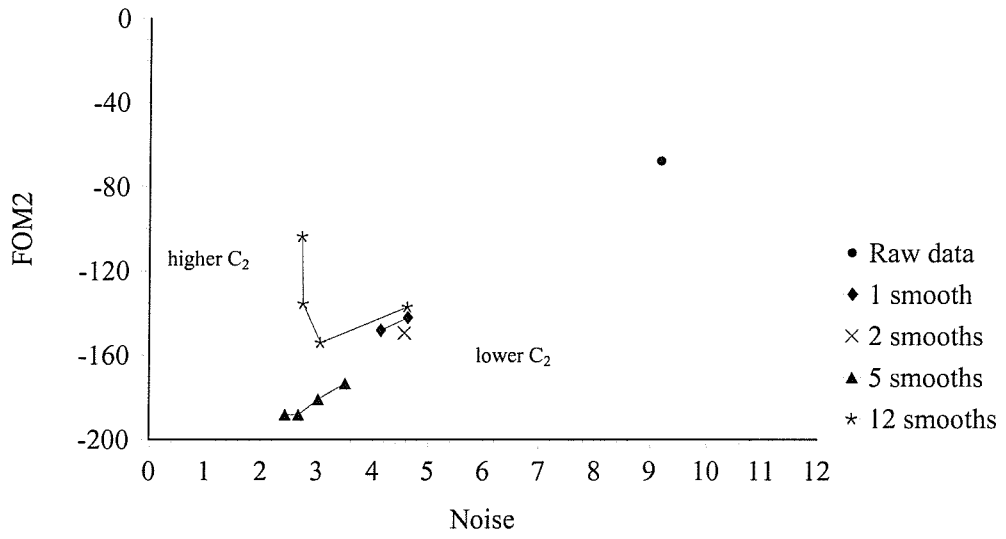

Figure 3.4: The FOM2 of maximum entropy solution when varying the number of smooths for the default solution, while using a fixed value of C_1 = 1.0, for the Williams phantom, total count is 108k. The highest numerical figure of merit (i.e., -200) indicates the optimum solution.

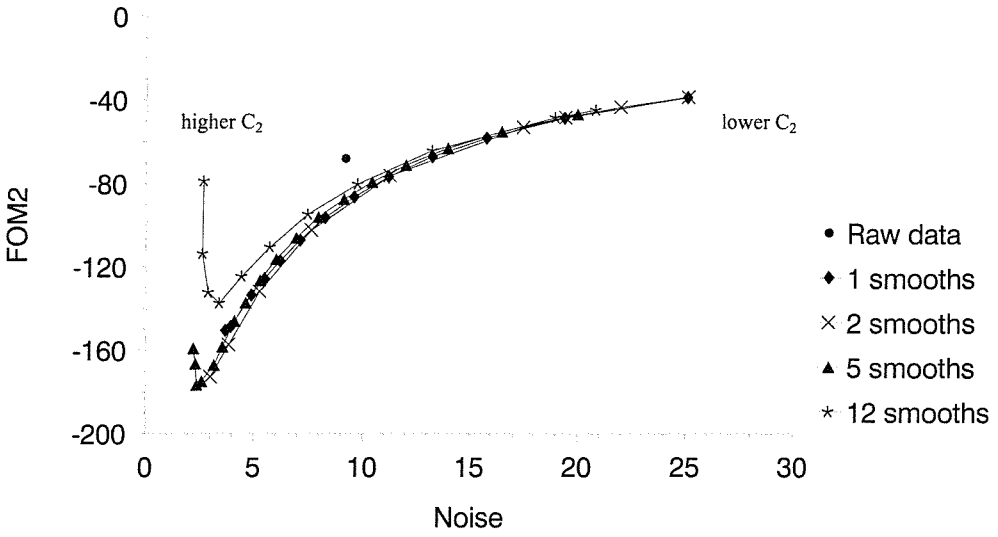

Figure 3.5a: The FOM2 of maximum entropy solution when varying the number of default smoothing using 1, 2, 5 and 12 smooths, while using a lower value of C_1 = 0.2 , for the Williams phantom, total count is 108k.

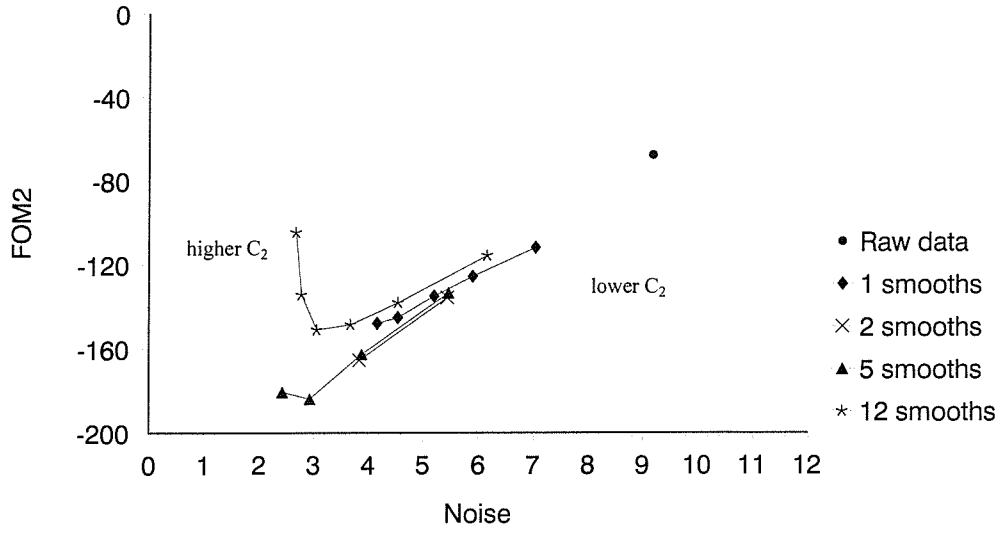

Figure 3.5b: The FOM2 of maximum entropy solution when varying the number of default smoothing using 1, 2, 5 and 12 smooths, while using a lower value of C_1 = 0.6 , for the Williams phantom, total count is 108k.

3.4.2.3 Conclusion

The investigation on defining the optimal number of smooths for the default solution b_i (equation 2.10), for which 1, 2, 5, and 12 smooths were used, suggested that the number of smoothing doesn't have a large effect on image quality. 5 smooths was considered the optimal number of smooths for the default solution according to the results so far, because it produced improved quality solutions compared to 1, 2, and 12 smooths. However lower count images might need a higher number of smooths. This needs to be investigated thoroughly in a larger variety of images.

3.4.3 Defining the Optimal Error Parameters

3.4.3.1 Method

To define the optimal error parameters which are required by the algorithm to specify the errors in the data, imaging of the 2.0 cm cold object in the Williams phantom has been investigated. The value of constants C_1 and C_2 have been varied over the whole range of convergence. Thus the value of constant C_1 was varied between 0.0 - 5.0, and the value of C_2 between 0.0 - 10.0 . The contrast and noise of the 2.0 cm cold object have been measured and the way they vary with the values of C_1 and C_2 studies. The image quality was calculated by measuring the figure of merit of the different solutions and the one with the optimal value determined.

3.4.3.2 Results and Discussion

The result shows (Figure 3.6a), that when applying maximum entropy on the raw data, using a fixed value of constant C_1 (C_1 = 0.3), and varying the values of constant C_2 (C_2 = 0.0 to 10), maximum entropy processing produced various different solutions but with certain values of C_2 (0.0 - 0.5 and 4.5 - 10), the algorithm did not converge and no solution was produced. The values of C_2 = 1.0 - 4.0, allowed the algorithm to converge and produce solutions which had different contrast and noise level. The contrast of each solution was increased when choosing a lower value of C_2, and at the same time the noise level was increased (Figure 3.6a). Therefore high contrast solutions were associated with high noise and vice versa.

Since the ideal solution has high contrast and low noise, the figure of merit is required to determine the optimal solution. The variation of FOM2 with value of C_2 is shown in figure 3.6b and with noise in figure 3.6c. As C_2 increased the FOM2 increased and the level of noise is decreased. The solution with the highest FOM2 was therefore in this case also the smoothest solution. The figure of merit of the raw data was about -67.9, which is well below the most of the maximum entropy solutions.

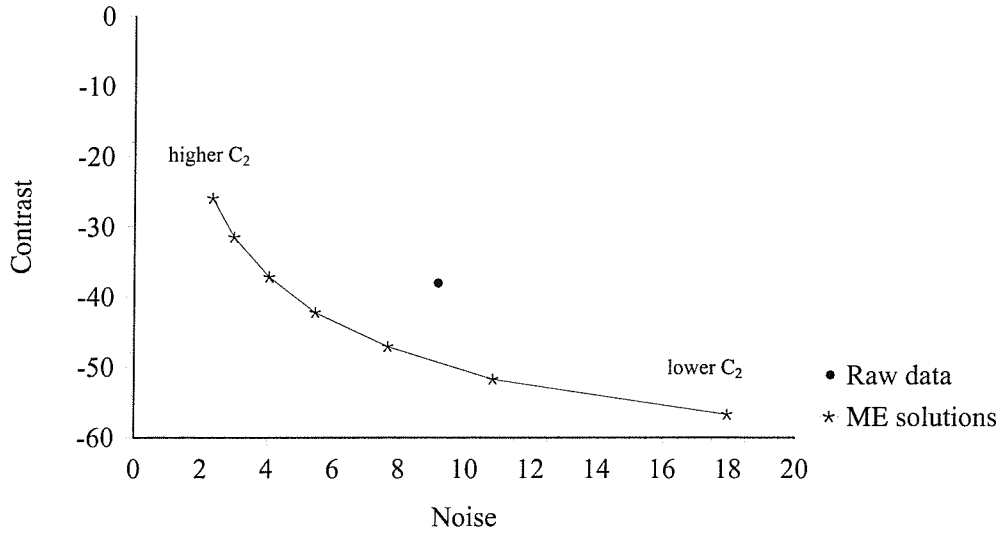

Figure 3.6a: Maximum entropy solutions of the Williams phantom, using a fixed low value of C_1 = 0.3 and varying the values of constant C_2 using 5 smooths for the default solution, where a high contrast solution is associated with high noise.

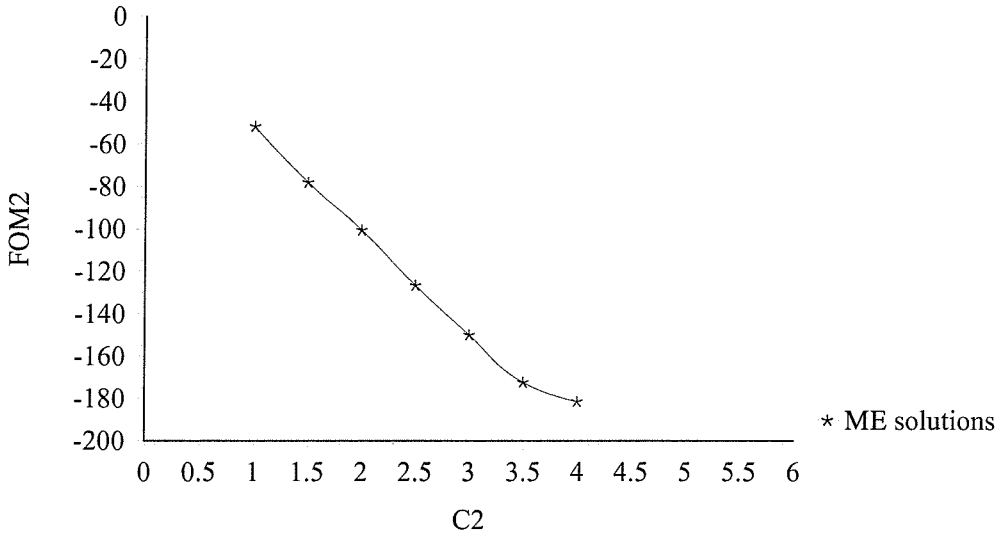

Figure 3.6b: The variations in the figure of merit of maximum entropy solutions with varying the values of error parameter C_2, and having a fixed value of C_1= 0.3.

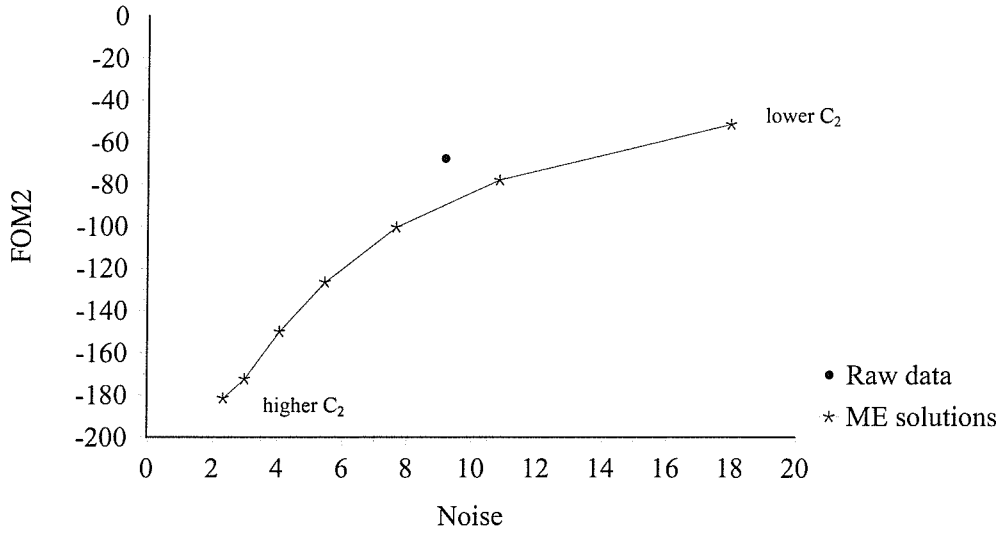

Figure 3.6c: The variations in the figure of merit and the level of noise of maximum entropy solutions, using C_1= 0.3, where the FOM2 of the raw data is well below the most of maximum entropy solutions.

The choice of the value of constant C_1 can be chosen based on the figure of merit. Theoretically the value of C_1= 1.0 is more acceptable. It has been found that the optimal figure of merit increased slowly as increasing the value of C_1 from zero until it reached C_1 = 1.0, then there was a rapid reduction in the figure of merit as the value of C_1 increased to more than 1 (Figure 3.6d). This will be explained in more detail in the next section (section 3.4.4).

Therefore the convergence of the algorithm and the figure of merit (FOM2) is dependent on the values of the error parameters C_1 and C_2. The variation in the figure of merit whether varying the constant C_1 or constant C_2 is illustrated more completely in table 3.1 .

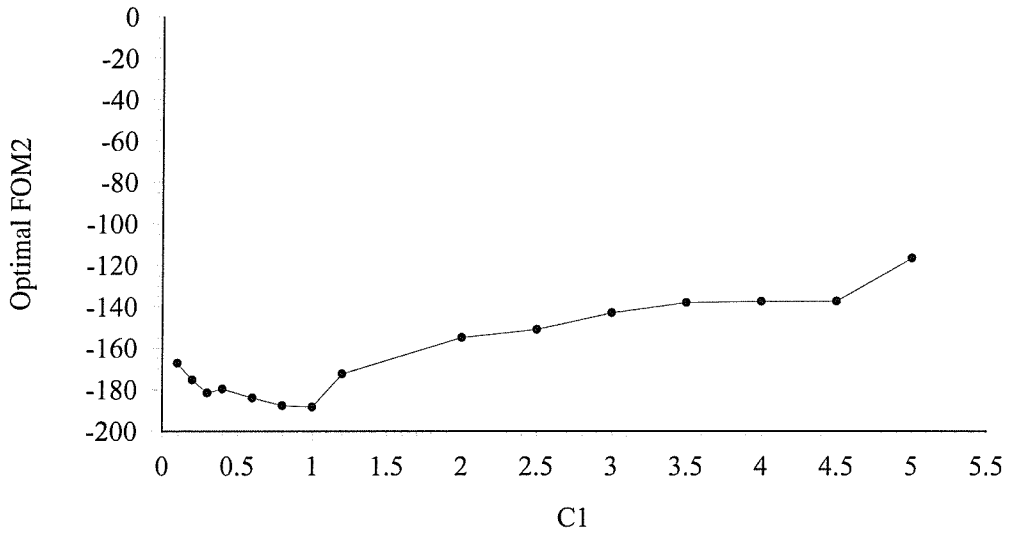

Figure 3.6d: The variations of the figure of merit 2 when we vary the value of C_1, while the drop off in the FOM2 can be noticed as we increased the value of C_1 to more than 1.

FOM 2

	/	/	/	/	/	/	/	/	**9.5**
*	/	/	/	/	/	/	/	/	**9.0**
*	/	/	/	/	/	/	/	/	**8.5**
*	/	/	/	/	/	/	/	/	**8.0**
*	/	/	/	/	/	/	/	/	**7.5**
*	/	/	/	/	/	/	/	/	**7.0**
*	/	/	/	/	/	/	/	/	**6.5**
*	/	/	/	/	/	/	/	/	**6.0**
*	-165.3	/	/	/	/	/	/	/	**5.5**
*	*-167.2*	-159.1	/	/	/	/	/	/	**5.0**
*	-155.6	*-175.3*	/	/	/	/	/	/	**4.5**
*	-129.4	-167.1	*-181.5*	/	/	/	/	/	**4.0**
*	-102.6	-141.4	-172.4	-177.0	/	/	/	/	**3.5**
*	-80.57	-116.3	-150.0	*-179.6*	/	/	/	/	**3.0**
*	-61.02	-91.51	-126.6	-158.6	-180.6	/	/	/	**2.5**
*	-43.87	-71.09	-100.6	-133.1	*-183.9*	#	/	/	**2.0**
*	*	-50.78	-78.16	-107.2	-162.7	*-187.6*	#	/	**1.5**
*	*	*	-51.78	-78.58	-133.6	-177.2	*-188.3*	#	**1.0**
*	*	*	*	*	*	*	-154.5	*-172.4*	**0.5**
*	*	*	*	*	*	*	*	*	**0.0**
0.0	**0.1**	**0.2**	**0.3**	**0.4**	**0.6**	**0.8**	**1.0**	**1.2**	

C_2

C_1

(*) Did not converge on maximum iterations (20) .
(/) Default solution fitted the data .
(#) Trial map fitted data on iteration 1 .

Table 3.1: The variations in the figure of merit 2, when the values of constants C_1 and C_2 are varied, using 5 smooths for the default solution, for the 2.0 cm cold object of the Williams phantom which has a total count of 108k.

3.4.3.3 Conclusion

The investigation of defining the optimal error parameters C_1 and C_2 which are required by the algorithm to specify the errors in the data, shows that the value of constant C_1 can be chosen based on the figure of merit. The optimal figure of merit was fairly independent of C_1 for values of C_1 below $C_1 = 1.0$. The decrease in the figure of merit for values of C_1 of more than 1, suggested that the theoretical value of $C_1 = 1.0$ would be acceptable. FOM2 depended heavily on parameter C_2 . In the example chosen the highest FOM2 was found at the upper limit of convergence, corresponding to the smoothest solution.

3.4.4 The Effect of Various Factors on Error Parameters

3.4.4.1 Method

There are various factors which have an effect on error parameters. This effect can be assessed by varying certain different factors on the image. These factors are the size of the object, and whether it is a hot or cold object, the total count in the image and the mean count (the number of counts/pixel) in the region of interest in the surrounding activity. The Williams phantom, Fleming phantom and Goddard phantom (see section 3.2.1), were chosen for the assessment of these effects. A selection of images of the phantoms with different total counts were obtained to enable the parameters to be varied. Regions of interest defining the object and background areas, were drawn on a high count image in which all the objects were clearly visible.

(i) *The Size of the Object*, The Williams phantom was used for assessing this effect. A region of interest for each cold object size (1.0, 2.0 and 4.0 cm) was drawn separately on the high count image and another region of interest was drawn in the surrounding area, as a background region. The same background region was used in conjunction with all three object sizes. An image with a total count of 108k count was used. The regions for each object and the surrounding background region were

first applied to the raw image. Using a fixed value of error parameter C_1 of 0.3, various maximum entropy solutions were obtained by varying the value of C_2. The image quality for each object was measured for all the solutions and the figure of merits were compared. In addition the optimal FOM2 value for each value of C_1 for which convergence was obtained was determined and its variation with C_1 studied for each object.

(ii) *Hot Objects*, Three hot objects in the Williams phantom (1.0, 2.0, and 4.0 cm diameter) were studied using the same procedure as in (i) above.

(iii) *The Total count in the Image*, For this measurement three images of the Williams phantom has been obtained with different total counts. The total counts were 216k count, 108k count and 46.5k count respectively. Investigating various values of constant C_1 of 0.0 - 1.2, different maximum entropy solutions were obtained by varying the value of C_2. The optimal FOM2 value for each value of C_1 for which convergence was obtained was also determined. The region of the 2 cm cold object and the surrounding background region (as drawn earlier) were applied on each distribution.

(iv) *Variation of Image Structure*, It was considered reasonable to hope that objective image parameters such as total count might be used to be able to predict the optimal error parameters in any particular image. For this to be useable the derived rules would have to be applicable to any image. Therefore the variation of FOM2 for the 2.0 cm cold object in the three different phantoms was studied. Two separate sets of measurements were carried out, (a) Where the total count was the same in the different phantoms and (b) where the counts per pixel in the surrounding region were constant (i.e., the mean count).

For all the measurements, the PICS Program (Fleming et al 1991) was used for calculating the image quality.

3.4.4.2 Results and Discussion

The result of the experiment on object size shows that the figure of merit for the three object sizes (1.0, 2.0, and 4.0 cm) in a Williams phantom are different. It can be noticed that (Figure 3.7a) the larger objects have a higher FOM2. This is expected since as increasing the object size, detectability should be higher. For all three objects the FOM2 is higher for low noise solutions corresponding to the higher values of C_2 for which convergence is obtained (Figure 3.7b). The values of C_2 producing the optimal FOM2 did however vary a little with the smallest object being optimally imaged with a slightly higher noise / higher contrast solution.

The results also show (Figure 3.8), that the optimal figure of merit does not depend very much on the value of C_1.

The measurements which were performed on the hot objects, show that hot objects are giving the same pattern of results (Figure 3.9), as the results of using cold objects as shown above, however there is a slight trend for hot objects to have a higher optimal FOM2.

The improvements in the image quality, when the maximum entropy processing technique was applied to the raw image is presented in (Figure 3.10).

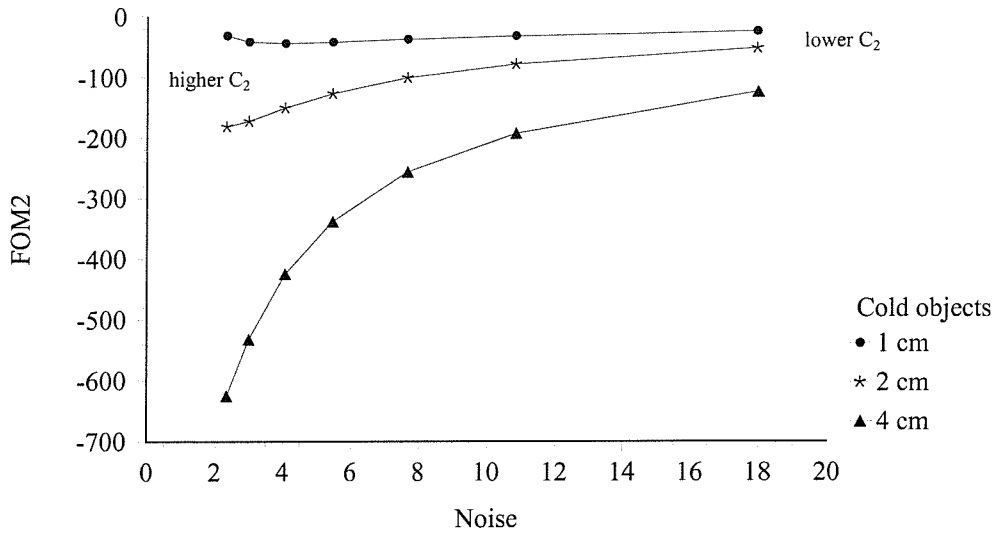

Figure 3.7a: The object FOM2 increases as the object size increase, for a given value of $C_1 = 0.3$ for the Williams phantom.

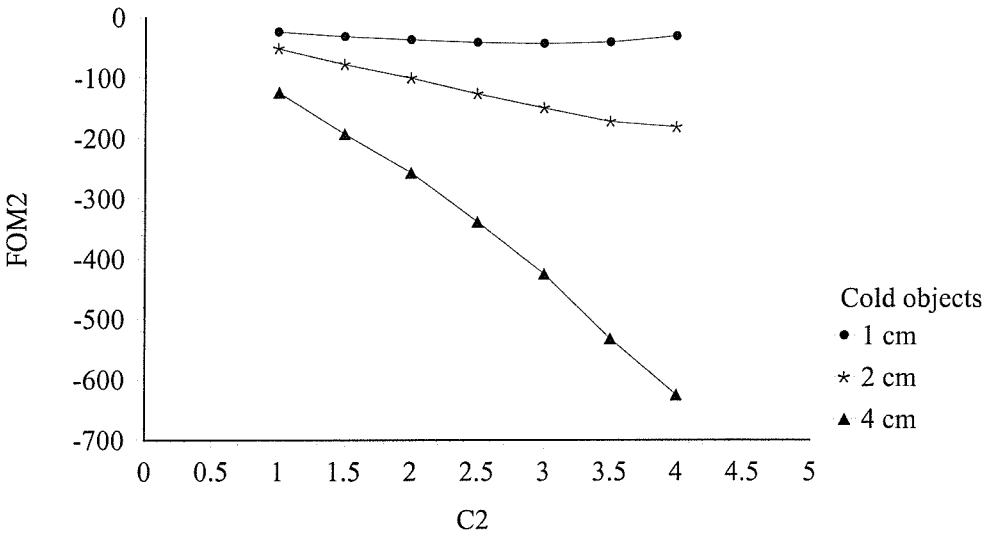

Figure 3.7b: When varying the value of C_2 for a given value of $C_1 = 0.3$ of the Williams phantom, the object FOM2 increases as increasing the object size.

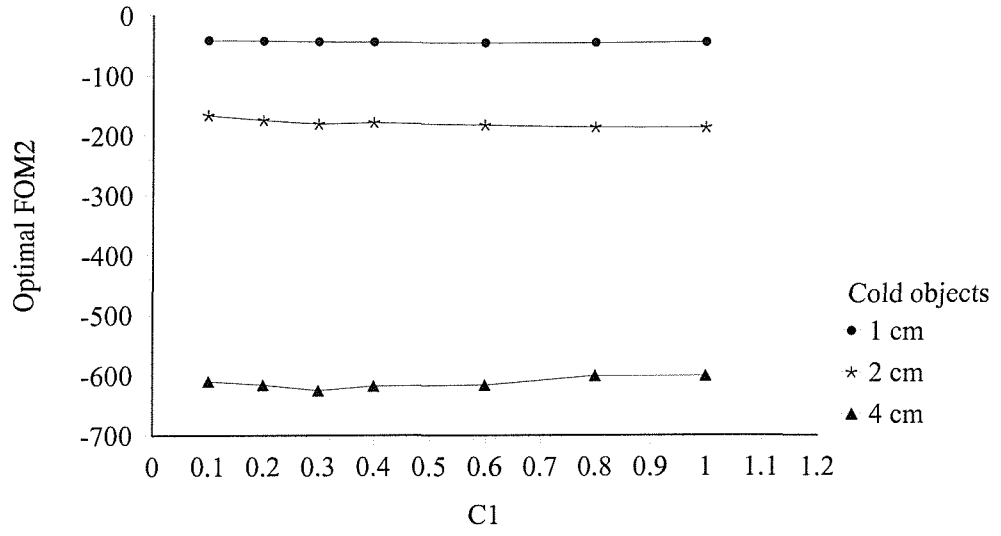

Figure 3.8: Determining the choice of C_1 for different cold objects sizes on the Williams phantom having a total count of 108k.

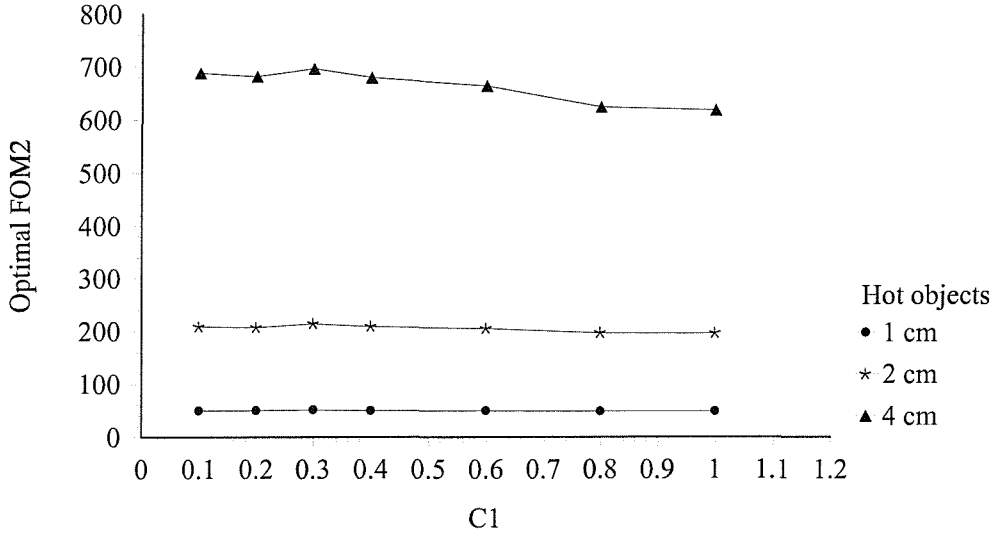

Figure 3.9: Determining the choice of constant C_1 for different hot objects, on the 108k count Williams phantom.

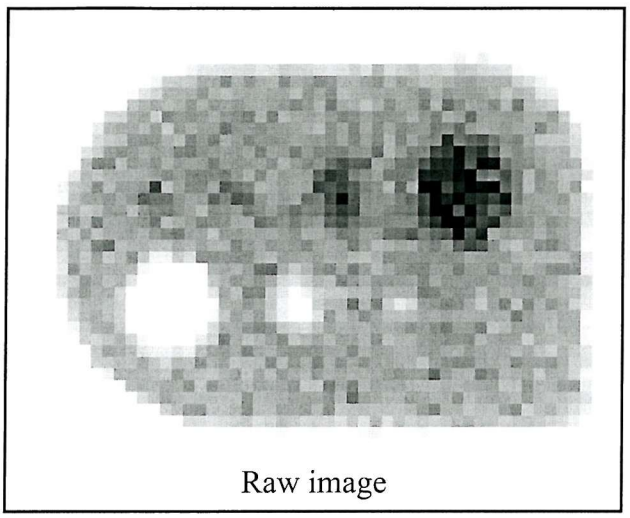

Raw image

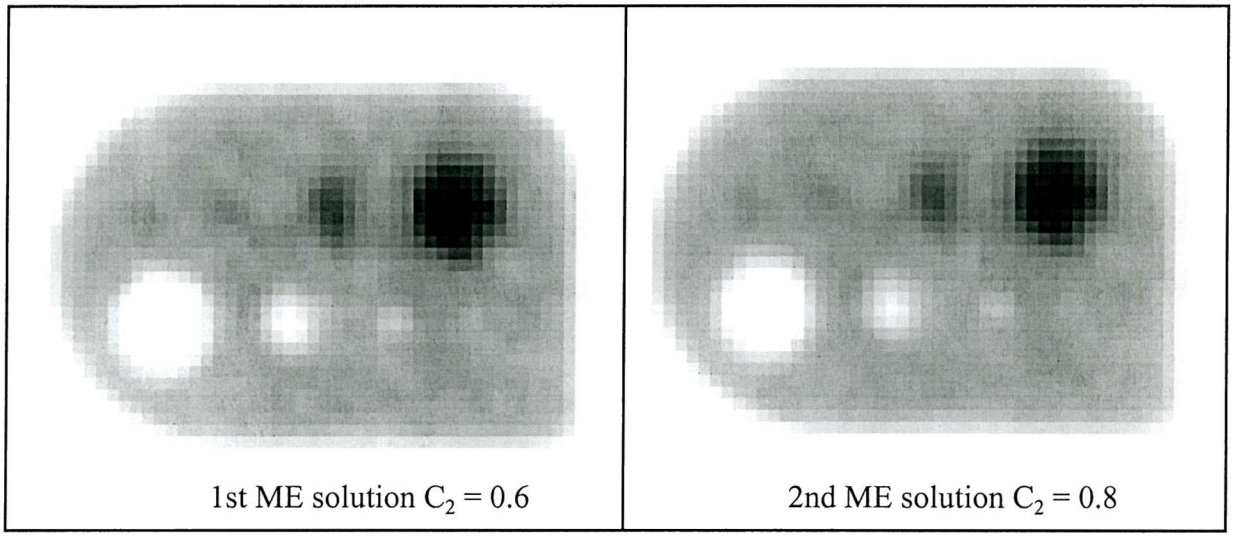

1st ME solution $C_2 = 0.6$

2nd ME solution $C_2 = 0.8$

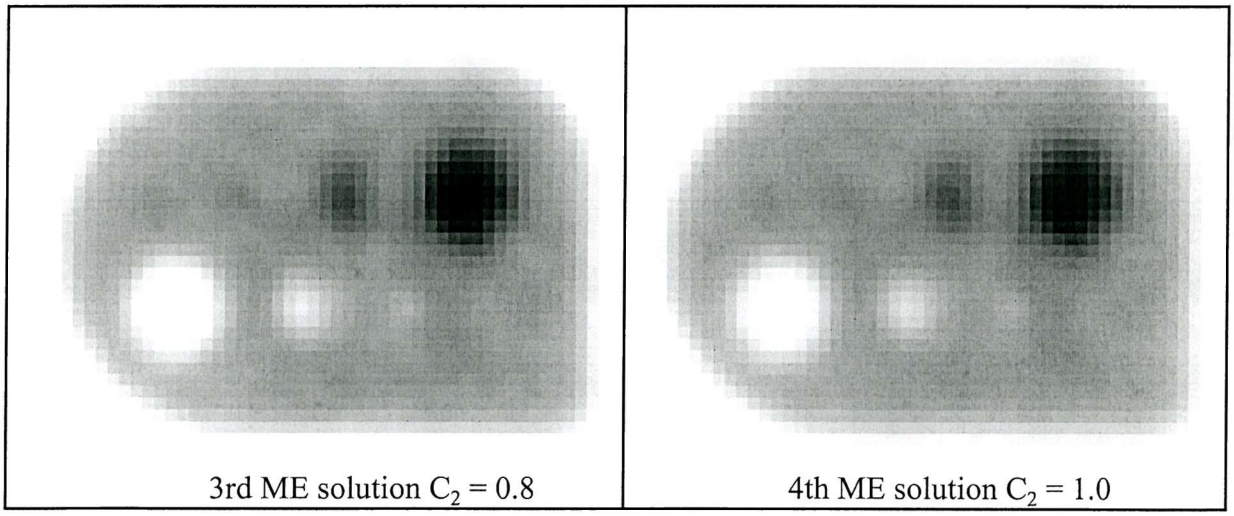

3rd ME solution $C_2 = 0.8$

4th ME solution $C_2 = 1.0$

Figure 3.10: The different solutions with an improvements in the image quality, when applying maximum entropy processing technique to the raw image, for the 2.0 cm cold object of the Williams phantom which has a total count of 108k count and $C_1 = 1.0$.

The effect of total count in the image on a 2.0 cm cold object of a Williams phantom shows (Figure 3.11a) that the optimal FOM2 for different values of C_1 are roughly constant. When choosing a fixed value of C_1 (C_1= 0.2 and 1.0), and varying the value of C_2 (Figure 3.11b and Figure 3.11c), a wide range of solutions for the three counts was found. However for C_1= 1.0 the range of solution is lower than when using a lower value of C_1 and therefore the FOM2 is more stable. The value of C_2 giving optimal FOM2 did depend on the total count for a given object suggesting that total count might be used to select C_2 .

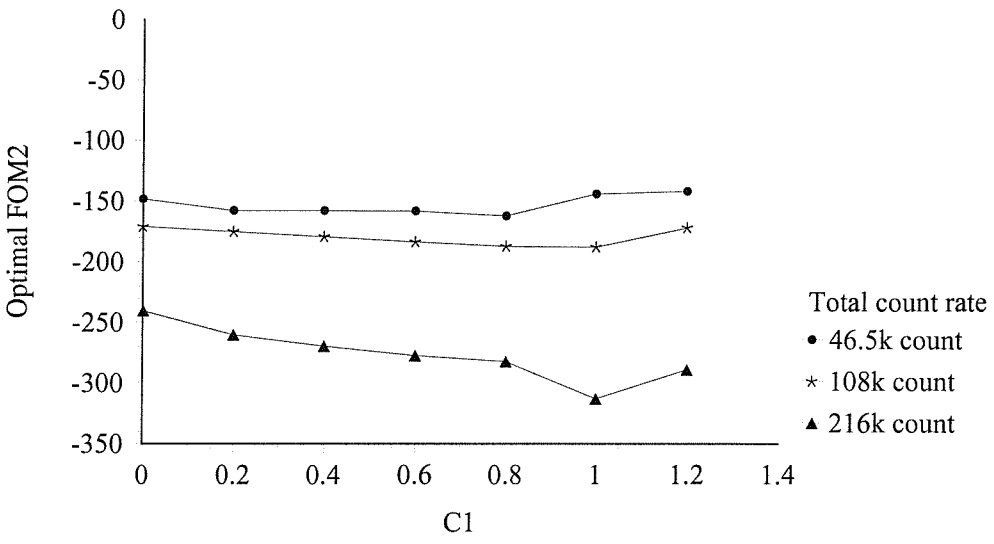

Figure 3.11a: The effect of total count on the error parameter C_1, for a 2.0 cm cold object of a Williams phantom. The optimal FOM2 is constant, showing the independence of the value of C_1 on the total count in the image.

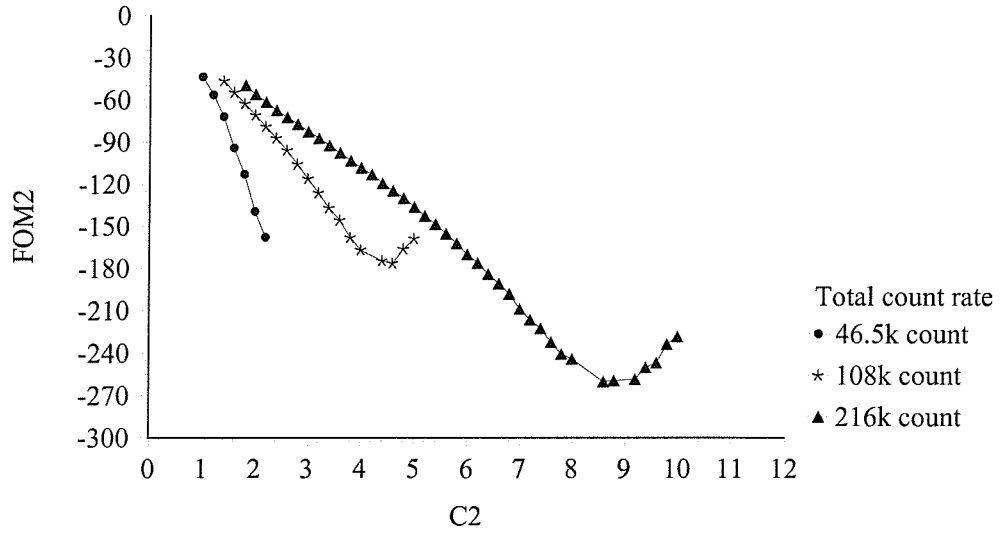

Figure 3.11b: The variations in the solutions of varying total count of a Williams phantom using C_1= 0.2 and varying the values of C_2 .

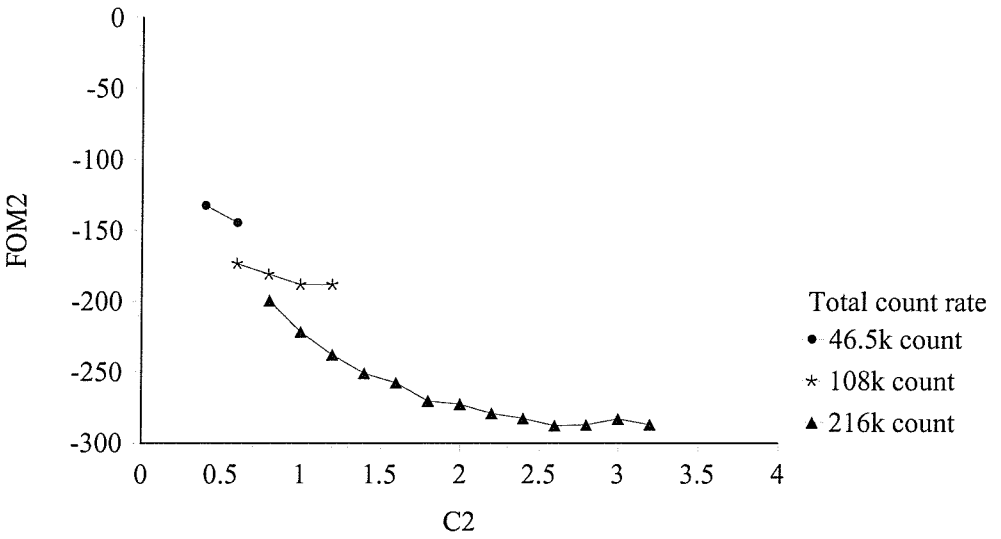

Figure 3.11c: The variation in the solutions of varying total count of a Williams phantom using a value of C_1= 1.0 and varying the values of C_2 .

The results of the measurement obtained using the same total count in the three phantoms shows that different FOM2 are obtained (Figure 3.12a). Here it is noticed that the three phantoms are varying in size, thus the Fleming phantom is the smallest in size, therefore that the mean number of counts per pixel in the Fleming phantom will be higher than the other two phantoms and hence the FOM2. Figure 3.12a, shows that for a given value of C_1 (C_1= 1.0), the optimal value of C_2 cannot be predicted from the total count because it is dependent on the environment. For the Williams and Goddard phantoms the best solutions were obtained at the upper end of the range of values for C_2 for which convergence was obtained. However for the Fleming phantom, the best solutions were obtained at the middle of the range of convergence.

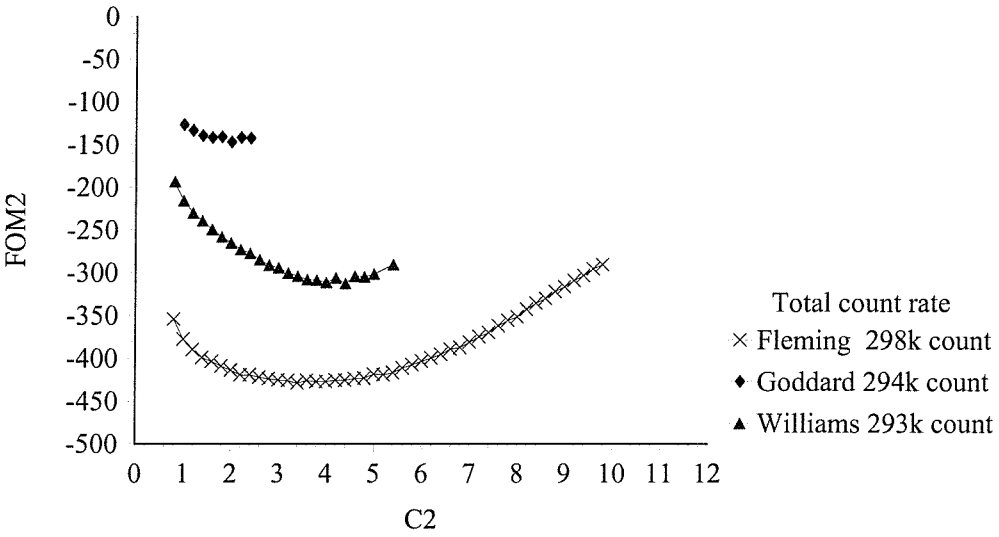

Figure 3.12a: The total count was kept uniform for the three phantoms at a given value of C_1= 1.0 and varying the values of C_2.

Having the same mean count in the surrounding background area in the three phantoms, gave similar optimal FOM2 values as would be expected (Figure 3.12b). However the value of C_2 giving the optimal solution was different for the three phantoms showing that mean count in surrounding area of the image cannot be used to predict the optimal C_2 value.

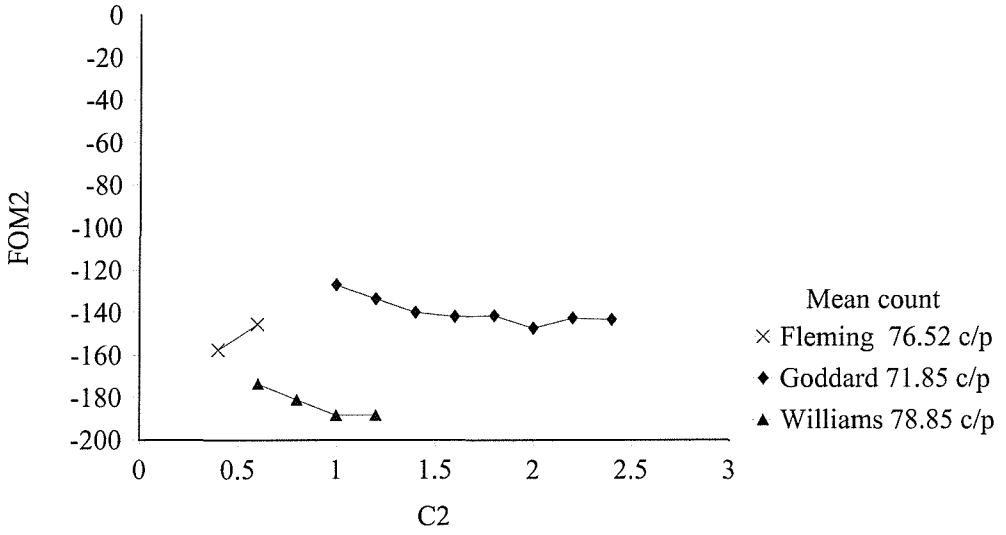

Figure 3.12b: The mean count (c/p) was kept uniform for the three phantoms at a given value of C_1= 1.0 and varying the values of C_2.

On the basis of the results obtained so far, the following method is suggested as a rule by which the value of error parameters C_1 and C_2 can be chosen. C_1 = 1.0 is a natural choice for that parameter. It is theoretically correct and although optimal solutions do not vary greatly with C_1, the result obtained with C_1 = 1.0 were slightly superior to other values in a number of solutions. In addition the range of solutions produced with C_1 = 1.0 is lower indicating that it will be more stable value.

In most of the examples studied to date with C_1 = 1.0, the value of C_2 giving optimal FOM2 was close to the higher limit of C_2 giving convergence (Figures 3.11 and

3.12). The only example where this was not the case was with the Fleming phantom with very high count per pixel where the optimal value of C_2 was closer to the lower limits of convergence. Therefore as a general rule it is intended to use the upper and lower limits of convergence, to calculate the optimal value of C_2, $C_{2\,opt}$.

Therefore, $C_{2\,opt} = L + 0.8\,(U - L)$ for $U < 5$ (3-4)

$C_{2\,opt} = 4$ for $U > 5$

where U and L are the upper and lower limits of convergence respectively.
This rule needs to be investigated thoroughly and tested in different situations.

3.4.4.3 Conclusion

The assessment of the effect of the various factors on the error parameters shows that as the size of the object is increased its FOM2 is increased. The values of C_2 producing the optimal FOM2 varied, with the smallest object being optimally imaged with a slightly higher noise / higher contrast solution. However the investigation shows that the optimal figures of merit were not dependent on C_1 for all three object sizes and for both hot and cold objects.

For $C_1 = 1.0$, the value of C_2 giving optimal solutions varied. However it was generally found that the best solutions were when C_2 was close to the upper limit of convergence. This enabled definition of a rule for the choice of C_2 based on the range of values giving convergence (equation 3-4). However this rule needs to be tested and investigated thoroughly for defining the optimal value of C_1 and C_2 in a variety of imaging situations.

The value of error parameter giving optimal FOM2 depends on the object size. The suggestion is that optimal FOM2 is at smoother end of a range of convergence. However error parameter C_1 does not affect the FOM2 severely.

Neither the total count nor the count per pixel could be used to predict parameter C_2 .

3.4.5 Comparing Maximum Entropy Solutions to Conventional Smoothing

3.4.5.1 Method

The purpose of this experiment was to compare the use of a simple data processing technique with the maximum entropy results described earlier. It was decided to investigate simple smoothing of the data (section 3.4.2.1). The Williams phantom image with 108k total count was studied. The conventional smoothing was obtained by applying a smoothing filter technique (see section 3.4.2.1). Eight solutions were produced corresponding to variation in the number of passes of the filter between 1 and 8 . A region of interest was drawn around the 2.0 cm cold object and a background region was drawn in the surroundings area. The image quality of the raw data, maximum entropy solutions and the conventionally smoothed images were calculated and their figures of merit were compared.

3.4.5.2 Results and Discussion

As previously maximum entropy produced a range of solutions in some of which both noise and contrast were improved simultaneously (Figure 3.13a). Image quality was increased significantly over the raw image (Figure 3.13b). The actual images were shown in figure 3.10 . The smaller hot and cold objects are more visible on the first two maximum entropy solutions. However the expected improvement in FOM2 in images 3 and 4 which have the highest FOM2 is not clearly apparent on visual inspection.

Smoothing always produce a decrease in contrast. However fair smoothing of the raw image reduces noise significantly without losing much contrast (Figure 3.13a)

and therefore the FOM2 increases initially (Figure 3.13b). However further smoothing of the raw data decreases contrast without further noise reduction (Figure 3.13a). Maximum entropy gave improved contrast compared to smoothing for higher contrast solutions but the highest, FOM2 for smoothing and maximum entropy are similar (Figure 3.13b).

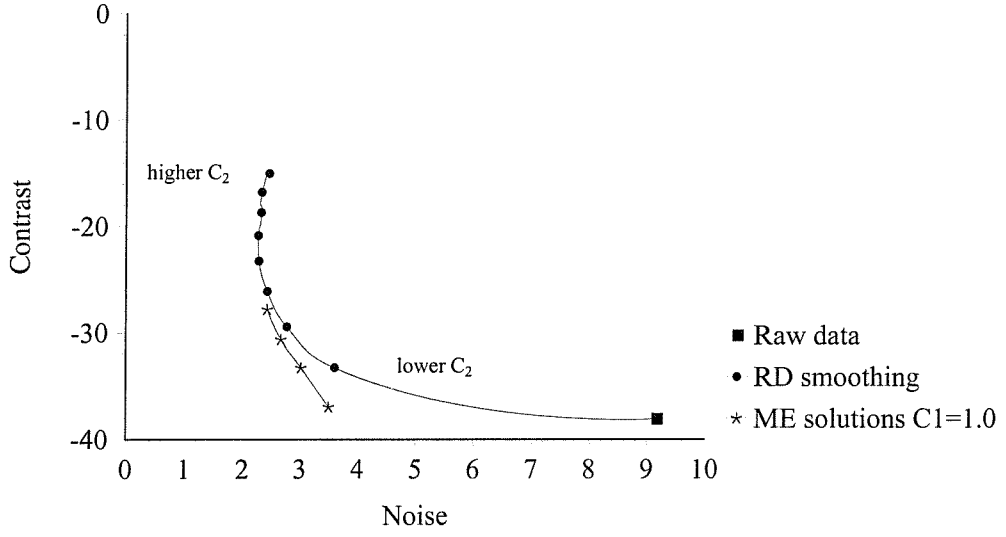

Figure 3.13a: The improvement in contrast and noise when applying maximum entropy processing and a conventional smoothing to the raw data, of the Williams phantom, total count is 108k count and using a value of C_1= 1.0 and varying the values of C_2 for maximum entropy processing.

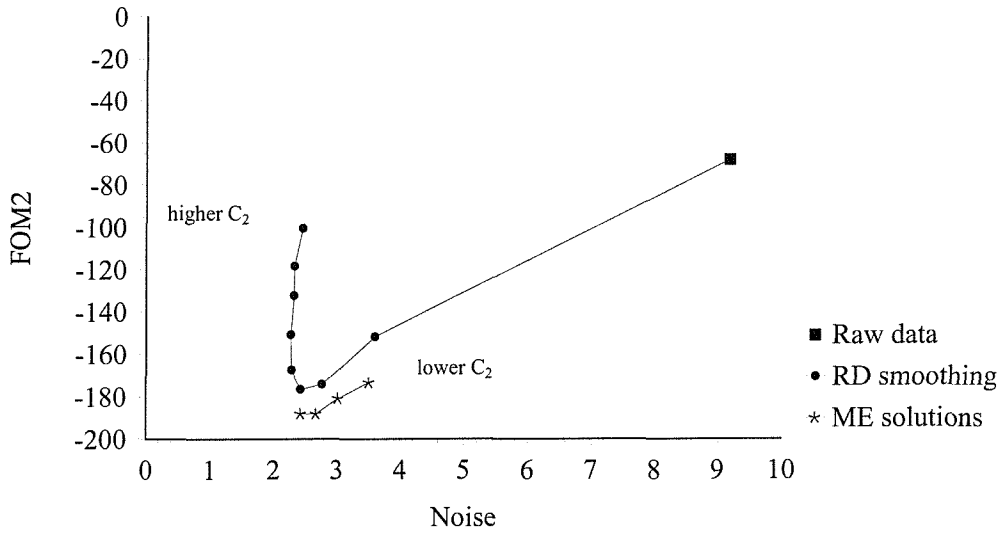

Figure 3.13b: The improvement in image FOM2 when applying maximum entropy technique and we can notice the similarity in the highest FOM2 of both techniques.

The actual images produced by maximum entropy and smoothing are shown in figure 3.14 .

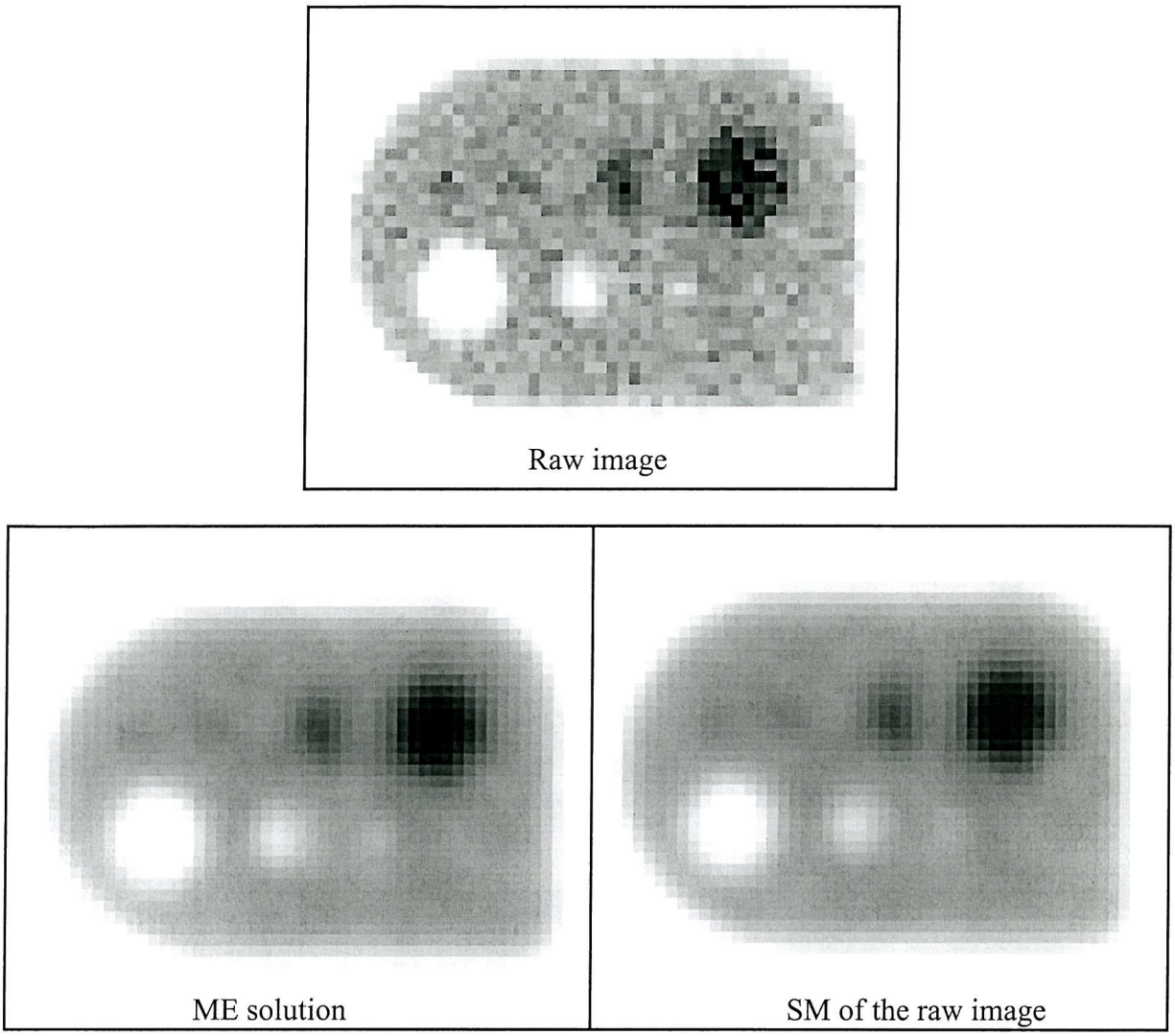

Figure 3.14: The improvement in contrast when applying maximum entropy processing to the raw image, compared to a conventional smoothing of the raw image.

3.4.5.3 Conclusion

The comparison of maximum entropy with smoothing showed that maximum entropy was able to produce a better contrast at relatively high noise solutions. However the maximum FOM2 which tended to be found at lower noise was very similar for the two techniques, although maximum entropy did give slightly higher values.

3.4.6 Investigation of the Value of Smoothing High Contrast Maximum Entropy Solutions

3.4.6.1 Method

The above results indicated that maximum entropy processing can produce solutions with increased contrast level, but also that smoothing is effective in reducing noise. This naturally leads to investigation of the effect of smoothing high contrast maximum entropy solutions. Therefore, maximum entropy solutions, which have the highest contrast for different values of C_1 were smoothed conventionally (as smoothing the raw data above), by a variable amount (Figure 3.15a). The image quality was calculated and compared to the raw data, maximum entropy solutions and the conventional smoothing of the raw data.

3.4.6.2 Results and Discussion

Here the results show that smoothing the maximum entropy solution which has the highest contrast level, for a given value of C_1, will produce images with a higher contrast than either maximum entropy or smoothing alone for a given noise level (Figure 3.15a). The FOM2 of the smoothed high contrast maximum entropy solution determined from the optimal FOM2 was clearly improved compared to the other two

processing techniques (Figure 3.15b). However an excessive smoothing of the high contrast maximum entropy solution will worsen the FOM2 of the images. The actual images produced by the three techniques are shown for comparison in figure 3.16 . The smoothing and maximum entropy techniques gave solutions with approximately equal optimal FOM2 and the corresponding images appeared similar. However the smoothed high contrast image with the highest figure of merit surprisingly looked somewhat inferior to the other two images. There is clearly some discrepancy between the figure of merit values and the visual appearance of the images.

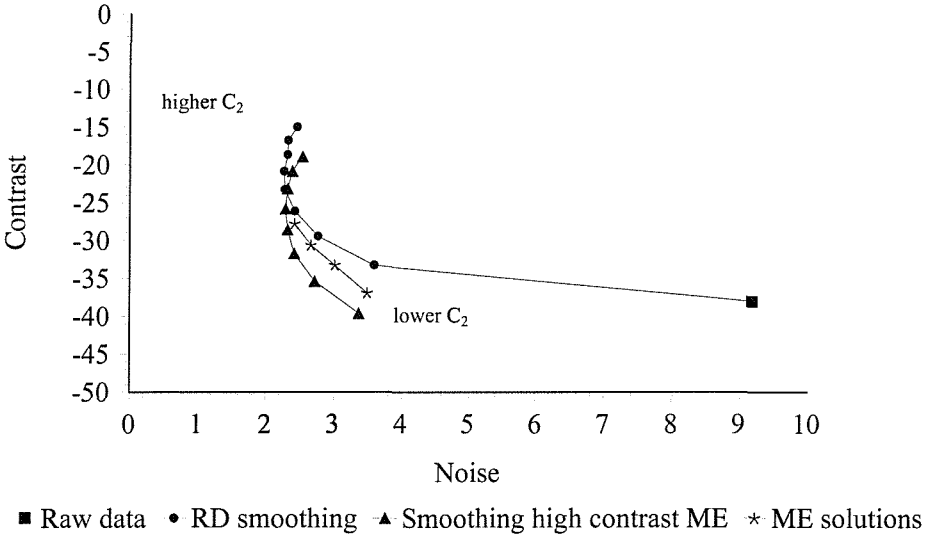

Figure 3.15a: The improvement in contrast when the technique of smoothing the highest maximum entropy solution is applied, over a conventional smoothing of the raw data, of the Williams phantom, total count is 108k count and using a value of C_1= 1.0 . For smoothing high contrast ME image, the value of C_1 = 0.6 is used, to allow a comparison with pure ME solution at C_1 = 1.0.

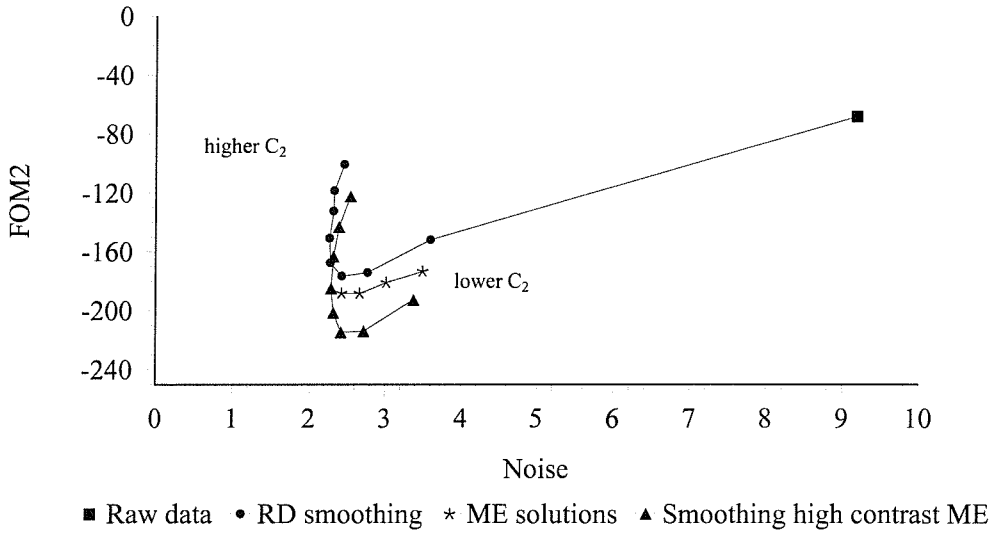

Figure 3.15b: The FOM2 of the solutions obtained using the technique of smoothing high contrast maximum entropy shows a higher FOM2 value, compared to pure ME solution and conventional smoothing of the raw data.

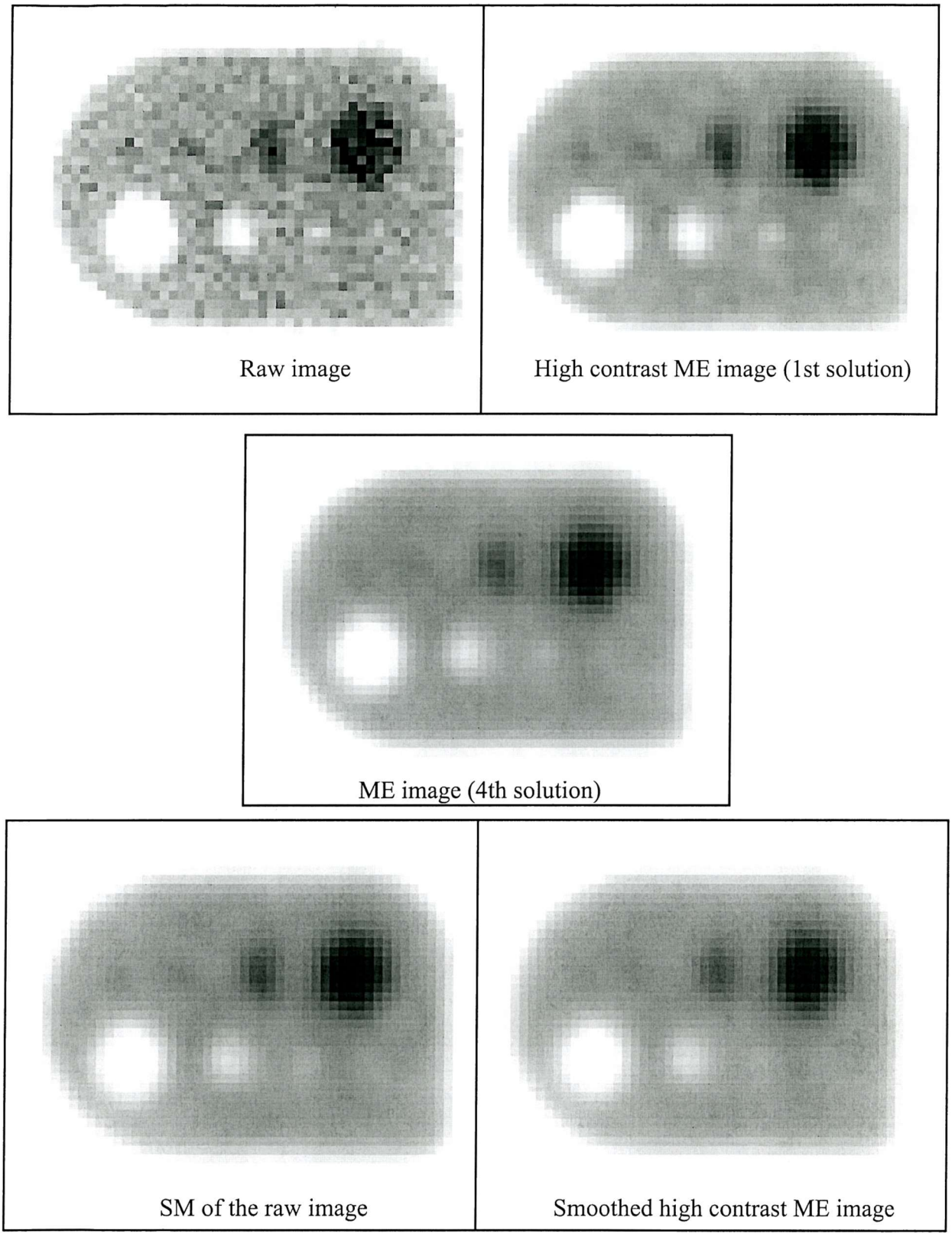

Figure 3.16: The images produced when smoothing the maximum entropy solution which has the highest contrast level, compared to the solution produced by maximum entropy or smoothing the raw data, at the same given level of noise (2.4 counts).

3.4.6.3 Conclusion

The success of smoothing in improving image quality led to the investigation of smoothing high contrast maximum entropy solutions. A high contrast maximum entropy solution was selected and smoothed by variable amounts. This produced solutions with higher FOM2 than the other two techniques (Figure 3.15b). For this technique the value of C_1=0.6 was used, in a since it is closer to C_1 = 1.0. However it will also be necessary to investigate the use of lower values of C_1 so the value producing the best quality solution can be found.

The qualitative appearance of the images of the Williams phantom following processing by all three techniques showed that there was very little difference in the visual clarity of the different object. This was somewhat surprising and disappointing in the case of the smoothing of the high contrast maximum entropy image, which according to the figure of merit should have been the best image.

3.5 Summary

The investigation of the validity of the error model proved that the assumption that the standard deviation of count is given by the square root of the count even at a very low count. Initial results suggest the algorithm should use 5 smooths for the default solution. A rule has been suggested for defining the optimal values of error parameters C_1 and C_2, which are required by the algorithm to specify the errors in the data. The assessment of the effect of the various factors on the error parameters shows that regardless of the size and state (cold or hot) of the objects, the optimal figure of merit is fairly independent of the value of C_1. The total count in the image and the mean count in the area containing activity (counts/pixel) could not easily be used in choosing the best value of error parameters C_1 and C_2 .

Smoothing produced optimal image quality comparable with maximum entropy although it was not able to produce images with contrast enhancement as was possible with maximum entropy.

Smoothing of a high contrast maximum entropy solution resulted in a better image quality parameter than the use of either algorithm alone. However this was not borne out in visual image inspection.

A study of the correspondence between the quantitative and visual assessment of the images will be the subject of further work in this thesis.

Chapter Four

The Effect of the Location of the Surrounding Background Region in the Calculation of Parameters of Nuclear Medicine Image Quality using Simulated Images

4.1 Introduction

An improved representation of nuclear medicine images can assist the observer in clinical decision making. The image quality is affected by many factors such as spatial resolution, scatter, and noise. Those interpreting (i.e., the nuclear medicine clinicians) are distracted by the presence of noise and unsharpness in the image and these defects impair perception. Our concern is visualizing a particular object in the image to help in decision making. An objective figure of merit (FOM) is a useful measure of image quality as it does not depend on subjective opinion. In this study, a FOM defined by contrast to noise ratio is used (Chesters 1992). Contrast and noise can be defined from the image by calculating the mean and standard deviation of count per pixel of both a region of interest and a surrounding background region. However, the values obtained may depend on the size and position of the surrounding background region. An investigation was therefore carried out to check the effect of different sizes of the surrounding background region on the image quality measurement. In this study a computer simulation was used to create the

images used for defining these regions. The advantage of using a simulated object is in the variety of distributions in the image that can be investigated and the ability to study systematically, the effects of various factors on the image.

4.2 Methods

4.2.1 Simulation Technique

The simulation of gamma camera imaging process which was used in this study used convolution of the activity distribution with a spatially varying the Point Spread Function (PSF) (Fleming et al 1994). The principle of this approach is to obtain the PSF of the gamma camera collimator system and its variation with distance from the collimator and thickness of intervening attenuating medium. The total PSF is the sum of the contributions from the primary photons and from scattered photons which are accepted by the collimator and detected in the energy window.

The primary photon PSF depends on the intrinsic resolution of the gamma camera detector and the geometric properties of the collimator. It accordingly depends on the distance of the point from the surface of the collimator face, attenuation thickness of the material between the point and the collimator and on the sensitivity of the gamma camera / collimator system in terms of count rate per unit activity. The scattered photon PSF also depended on the thickness of attenuation material between the point and camera, i.e., forward scattering material, but was assumed independent of the distance from the collimator and the thickness of backscattering material (Fleming and Simpson 1994).

The simulation technique requires definition of a three-dimensional distribution of activity and the corresponding map of attenuation coefficients of the distribution volume and its surroundings. The corresponding two-dimensional projection image produced with the camera in the x, y plane is composed of the sum of the primary photon and scattered photon contributions. The field of view of the gamma camera was

digitised as a 128 × 128 matrix with a corresponding pixel size of 0.467 cm (Fleming 1996).

4.2.2 Study on the Effect of Background Region Position

4.2.2.1 Image Simulation

The simulated image was a planar source of activity parallel to the camera face at a distance of 13.0 cm with 12.6 cm of water equivalent material between it and the collimator. The dimensions of the simulated images were 18.0 cm × 18.0 cm, area containing a uniform distribution of activity, with a square cold object of dimensions, 0.9 cm × 0.9 cm (2 × 2 pixel), in the middle of the image with no activity. The object was 1 pixel (0.467 cm) deep. Initially one image of the distribution was simulated without any noise and a second with a typical level of noise. Noise was added to each pixel count according to Poisson statistics. The simulated image appears as a square area with a uniform activity, in the middle it contains a cold object representing a square cold area with no radioactivity located in the centre of the image. The image obtained is a planar image produced with the camera in perpendicular plane and composed of the sum of the primary and scattered photons contributions. The first simulated image is a noiseless image used for defining the object region of interest and the surrounding background regions, whereas the second simulated image is a noisy image typical of those used for all the processing and image quality calculations in this study (Figure 4.1). The noise added is random and therefore several different images of the same imaging process can be simulated which will differ only in their noise content. These are referred to as different realisations of the imaging process.

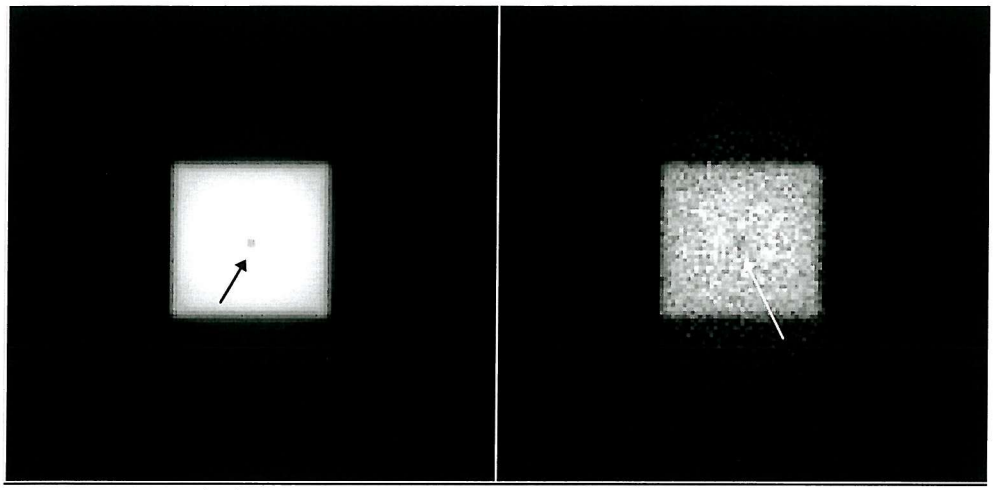

(a) (b)

Figure 4.1: The simulated images which are used in the investigation are (a) a noiseless image with a uniform variation in the count and (b) a noisy image. The 1.0 cm cold object is clearly visible in the centre of the noiseless image.

4.2.2.2 The Technique

A 2 × 2 pixel square region was defined representing the 0.9 cm simulated cold object. Surrounding background regions (SBKG region) of annular shape; 1 pixel wide and of varying radius, were also created (Figure 4.2).

The annuli regions were centered around the object. The annular region was chosen because all the points surrounding the object should have approximately the same count as they are the same distance from the cold object. The surrounding background regions were labelled (i.e. R02 - R18), (Table 4.1.) The radius of the largest region was 19 pixels (8.87 cm), which is very close to the edge of the image. For completion of the study another object with the same dimensions (i.e., 2 × 2 pixel square region), was simulated representing a 0.9 cm hot object. The count per pixel in the hot object was twice the count in the surrounding area.

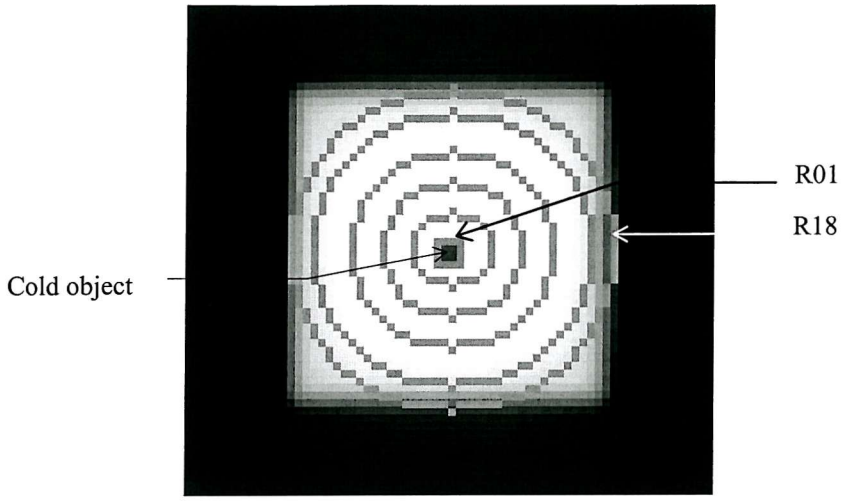

Figure 4.2: A representation of how the different SBKG regions were defined in this investigation, where the cold object appears as a square area in the middle and the first SBKG region (R01), is a square around it. The maximum size region, (R18), is shown on the border of the image. The SBKG region is a 1 pixel wide annulus.

Region Label (R)	The radius of the actual surrounding background region (SBKG region)	
	in pixel	in centimeter
R01	2	0.93
R02	3	1.40
R03	4	1.87
R04	5	2.33
R05	6	2.80
R06	7	3.27
R07	8	3.74
R08	9	4.20
R09	10	4.67
R10	11	5.14
R11	12	5.60
R12	13	6.07
R13	14	6.54
R14	15	7.00
R15	16	7.47
R16	17	7.94
R17	18	8.41
R18	19	8.87

Table 4.1: The radius for the different surrounding background (SBKG) regions, which were used in this investigation.

Contrast and noise measures were used for the calculation of the image quality. The contrast level is defined from the difference between the mean count per pixel in the object and the surrounding background region. The noise level is the standard deviation of counts in the uniform area surrounding the object.

For both hot and cold objects, 13 different realisations of the images were obtained to enable the variation of noise and contrast to be studied.

The image quality was measured using the defined object region and the SBKG regions for the raw data and the processed image. The processed image was produced by the maximum entropy processing technique.

4.3 Results

The level of noise for the raw data shows a variation in the standard deviation as the position and size of the 1 pixel wide SBKG region was varied (Figure 4.3).

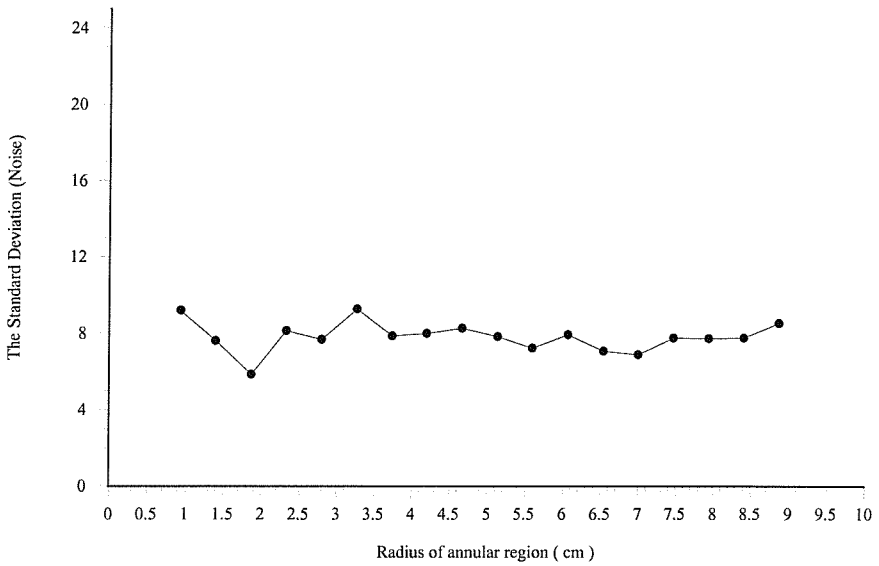

Figure 4.3: The level of noise (i.e., a standard deviation), for the raw data of a single 1.0 cm simulated cold object using different SBKG regions (R01 - R18), positioned in different areas surrounding the object.

Variations in the standard deviation occurred particularly in the regions which are closer to the object. However as the size of the SBKG region was increased which is evidently accompanied by a change in the position, the result shows an approximately constant value for the standard deviation of the raw data images. Some other realizations were therefore simulated (i.e., 13 different simulated images representing the raw data), with the same image parameters and the results were averaged (i.e., the mean) to get a better estimate of the standard deviation (Figure 4.4).

A paired t-test showed that there was a statistically significant increase in the noise with distance for regions close to the object border ($P < 0.05$). Noise was then kept constant with distance until there was a sudden increase for SBKG region R18, which was drawn very close to the edge of the image.

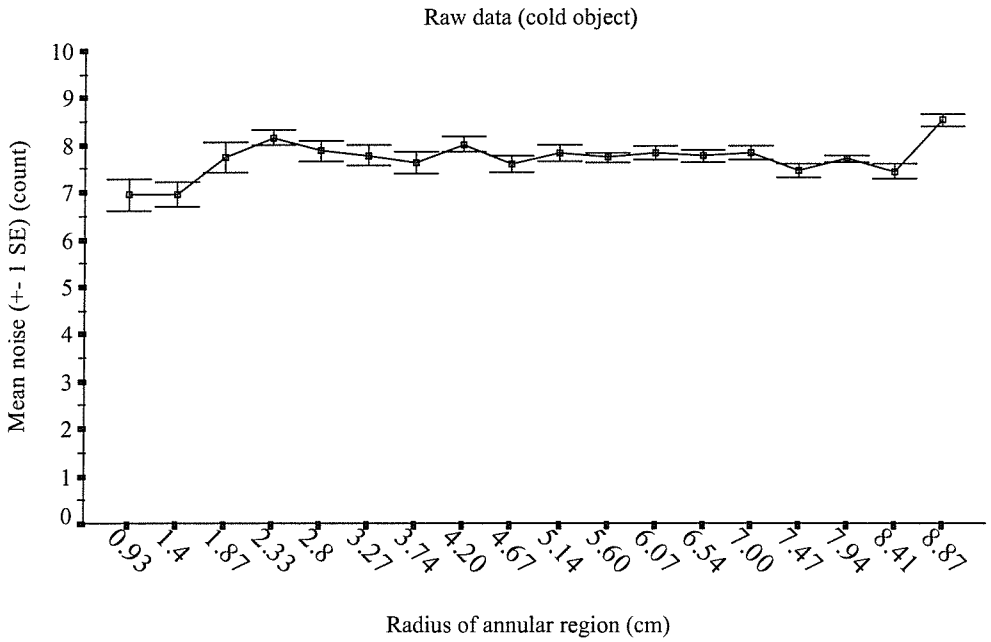

Figure 4.4: The standard deviation of count (±/ standard error on the mean) for the raw data of 13 simulated 1.0 cm cold objects, for annular regions of varying radius.

When the raw data was processed using the maximum entropy technique, the result (Figure 4.5) shows the same pattern of result as in figure 4.4, although the standard

deviation was less in the result produced when the maximum entropy technique was applied.

As the position of the SBKG region changed (Figures 4.6 and 4.7), the contrast level for the raw data and the maximum entropy solution shows similarity in the pattern results, although the contrast level for the raw data was less than when it was processed by maximum entropy technique. There was a significant increase in contrast level between R01 (0.93 cm) to R03 (1.87 cm), for both images. As the radius of the region increased to 4.2 cm, the contrast level was maintained at a reasonably constant level. Subsequently there was a drop in the measured contrast level as the size and position of the SBKG region was increased (i.e., R08 (4.20 cm) to R18(8.87 cm).

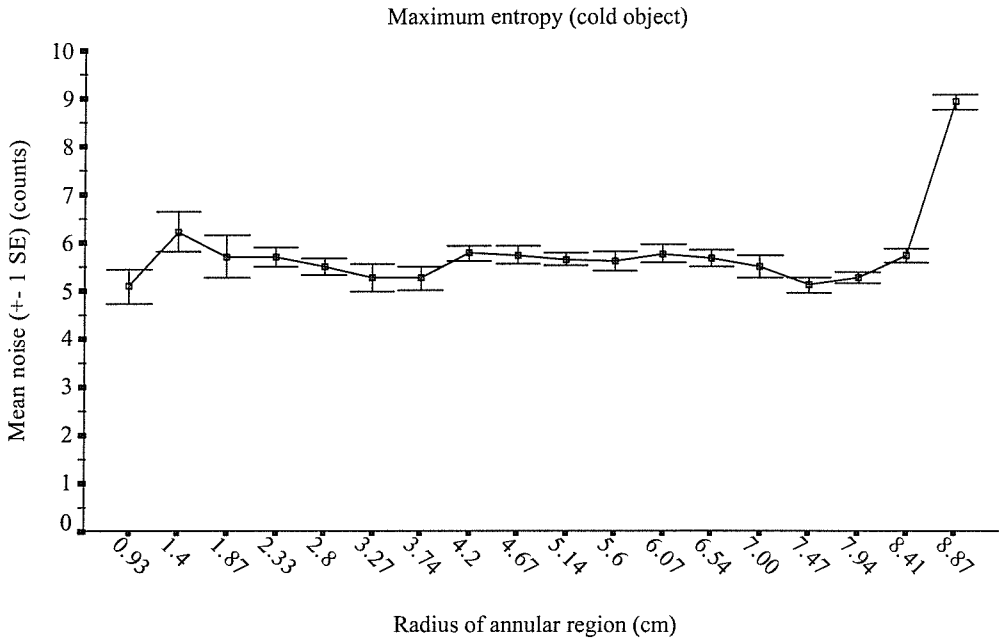

Figure 4.5: The standard deviation of count (±/ standard error on the mean) for the different 1.0 cm simulated cold objects for maximum entropy solution (ME), with changing the position of the SBKG region R01 - R18.

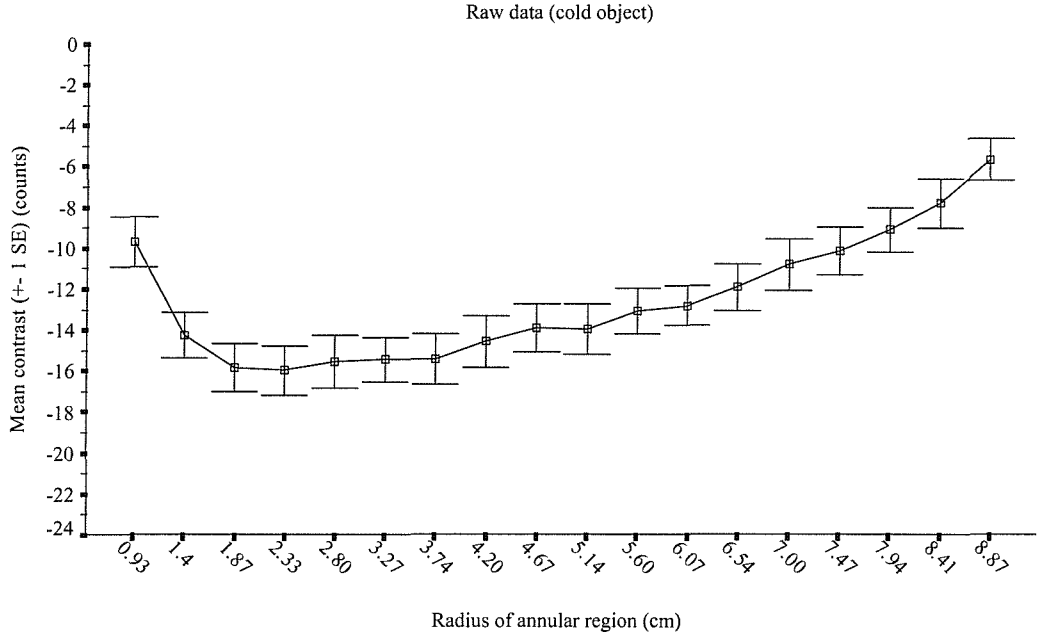

Figure 4.6: The mean for the contrast of the first solution for a 1.0 cm simulated cold object for the raw data solution using different widths for the different BKG regions.

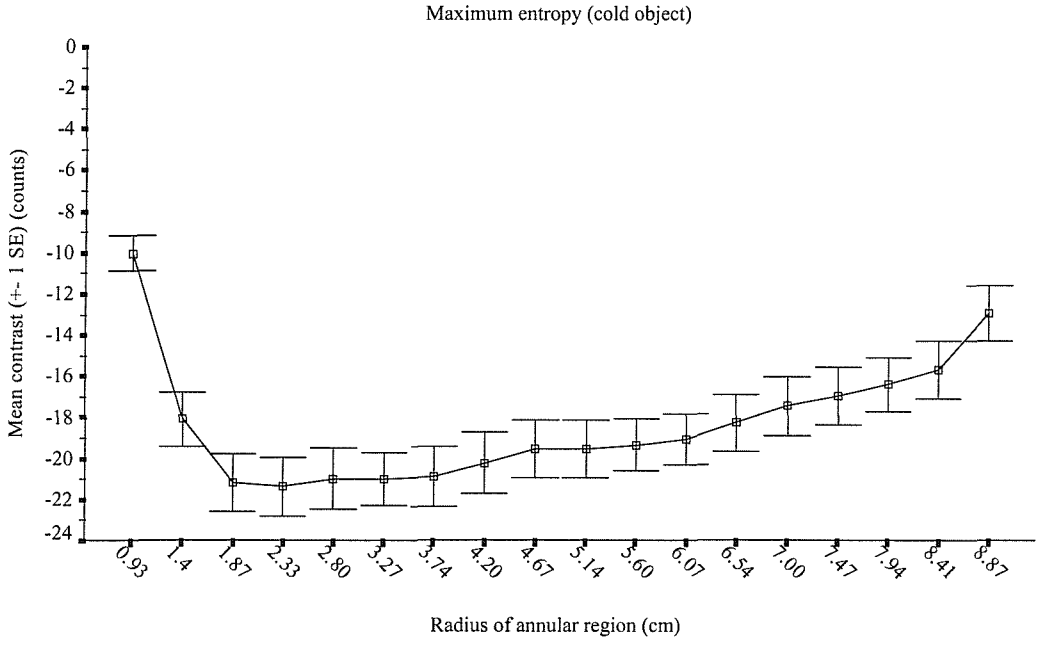

Figure 4.7: The mean for the contrast of the first solution for a 1.0 cm simulated cold object for maximum entropy solution using different widths for the different BKG regions.

The results for the FOM of the raw data and the maximum entropy solution shows substantial variations with the position of the surrounding region. These variations essentially followed the changes in contrast and were hence showed a decrease for regions drawn close to the object or at the edge of the image (Figures 4.8 and 4.9). The FOM for both results were reasonably constant in between 2.0 and 4 cm radius, however, there was a significant drop in the FOM for higher radii.

Similar results were also obtained when a simulated 1.0 cm hot object (Figures 4.10,4.11,4.12,4.13,4.14 and 4.15) was measured. However in this case the contrast increases for radii above 4.0 cm.

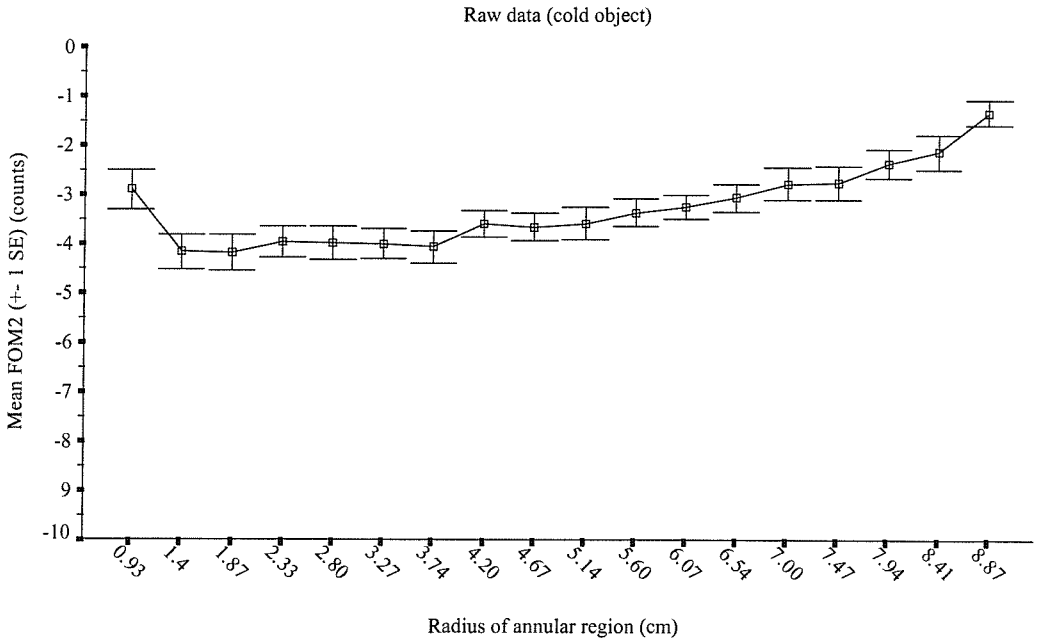

Figure 4.8: The mean for the figure of merit of the first solution for a 1.0 cm simulated cold object for the raw data solution using different widths for the different BKG regions.

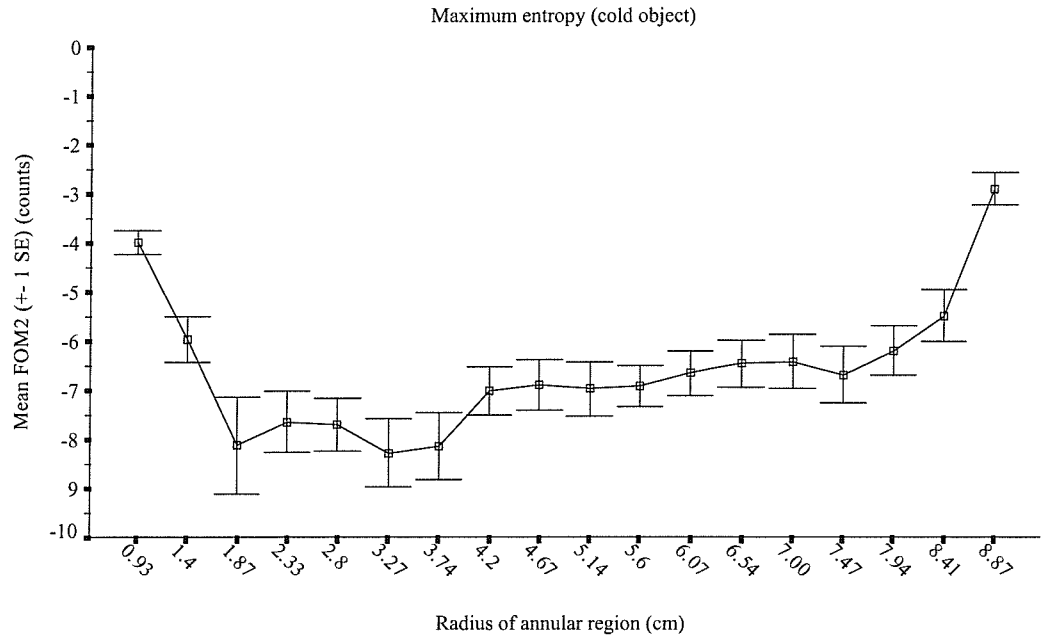

Figure 4.9: The mean for the figure of merit of the first solution for a 1.0 cm simulated cold object for the maximum entropy solution using different widths for the different BKG regions.

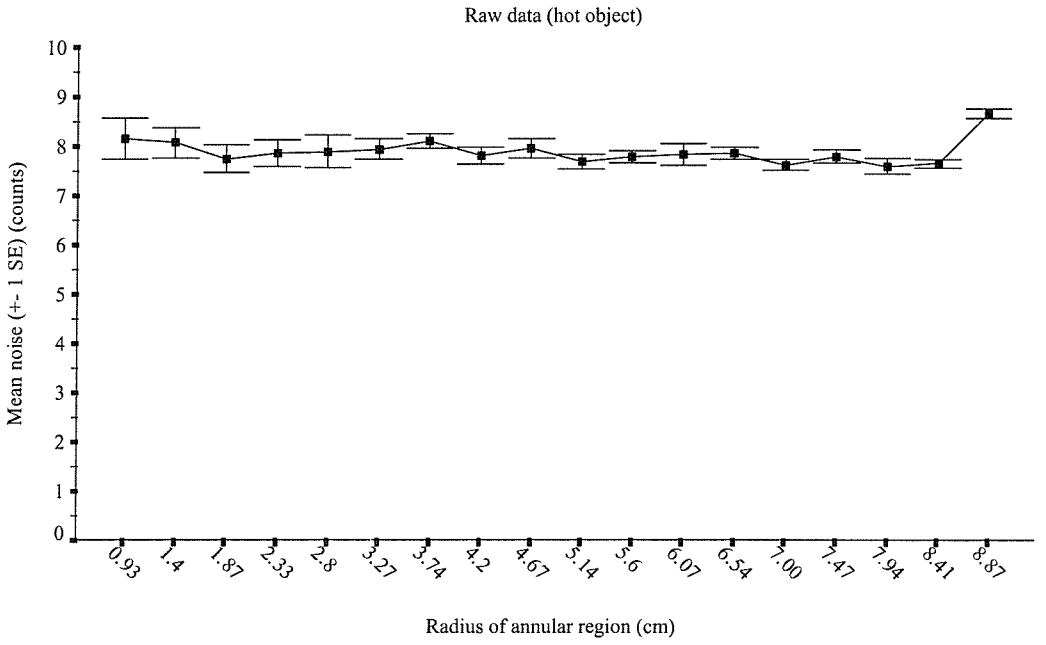

Figure 4.10: The standard error of the mean of the standard deviation for the raw data of 13 simulated 1.0 cm hot objects, for annular regions of varying radius.

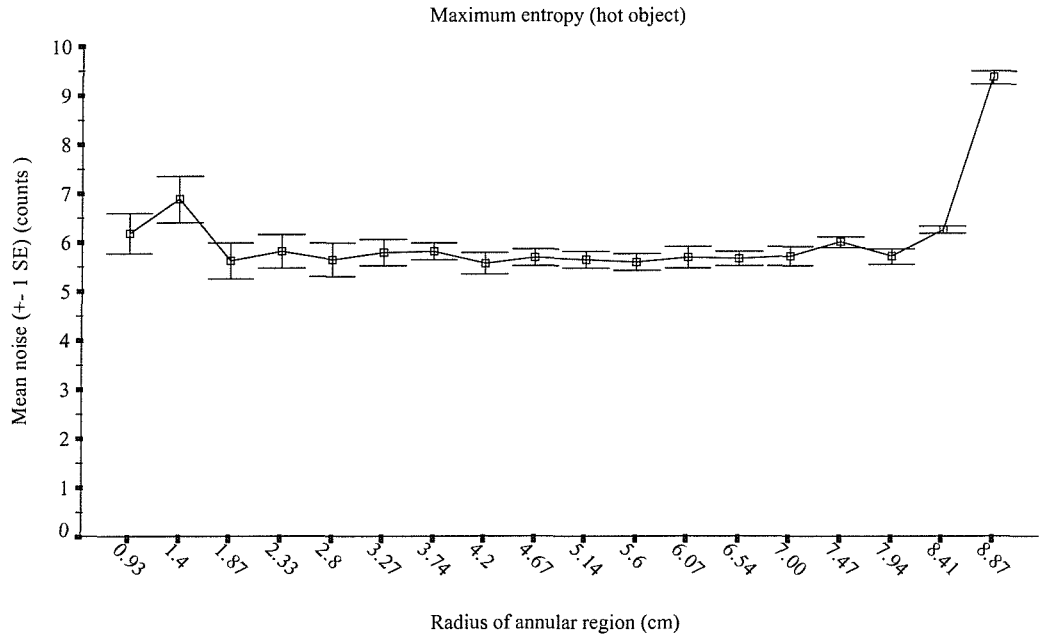

Figure 4.11: The standard error of the mean of the standard deviation for the maximum entropy of 13 simulated 1.0 cm hot objects, for annular regions of varying radius.

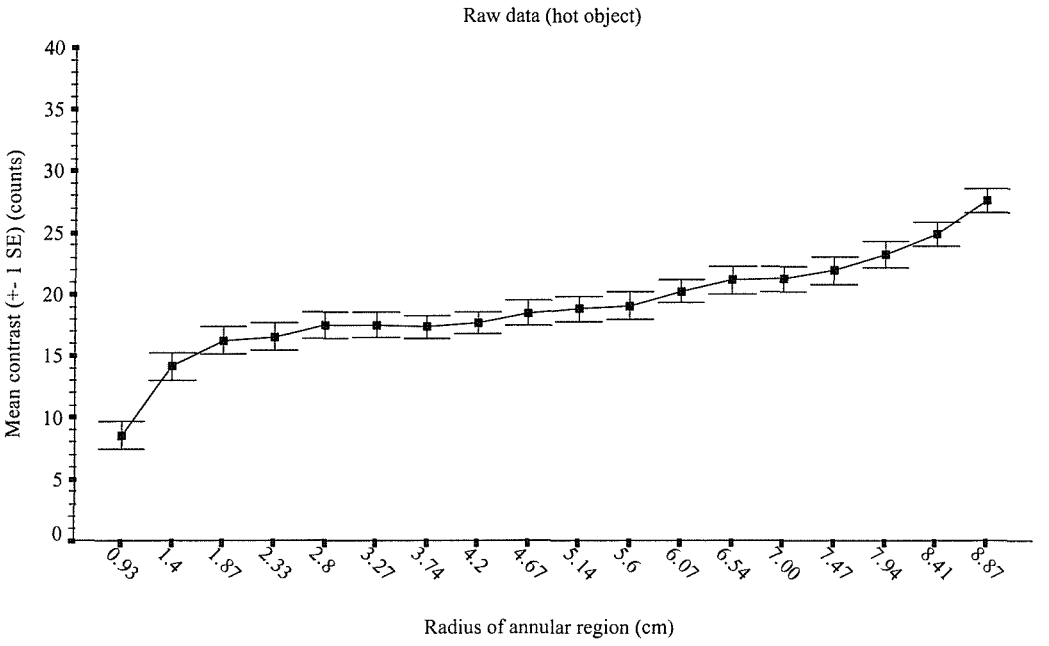

Figure 4.12: The mean for the contrast of the first solution for a 1.0 cm simulated hot object for the raw data solution using different widths for the different BKG regions.

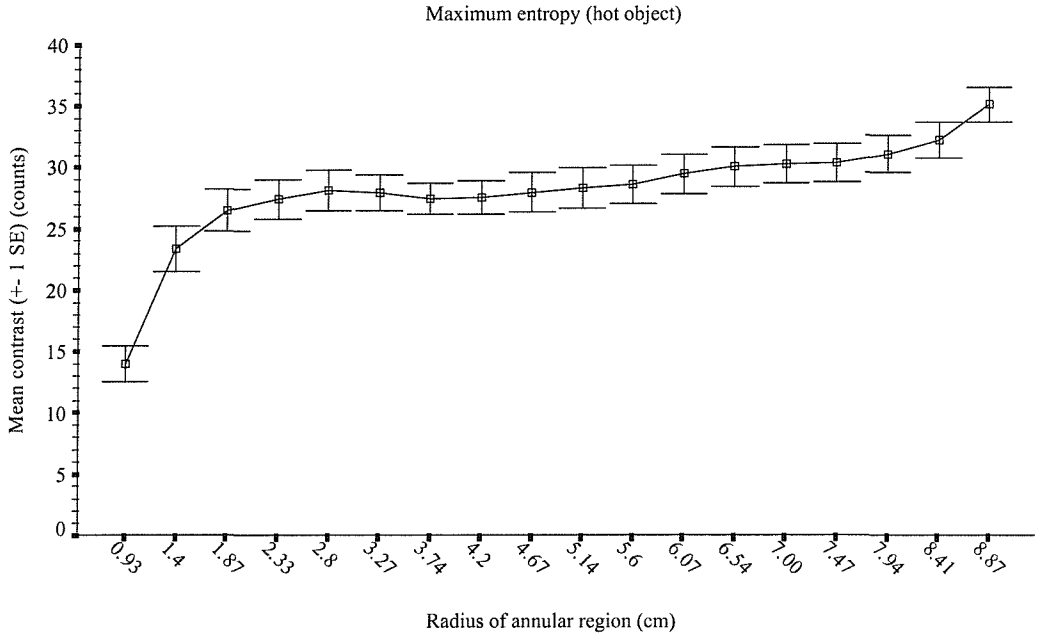

Figure 4.13: The mean for the contrast of the first solution for a 1.0 cm simulated hot object for the maximum entropy solution using different widths for the different BKG regions.

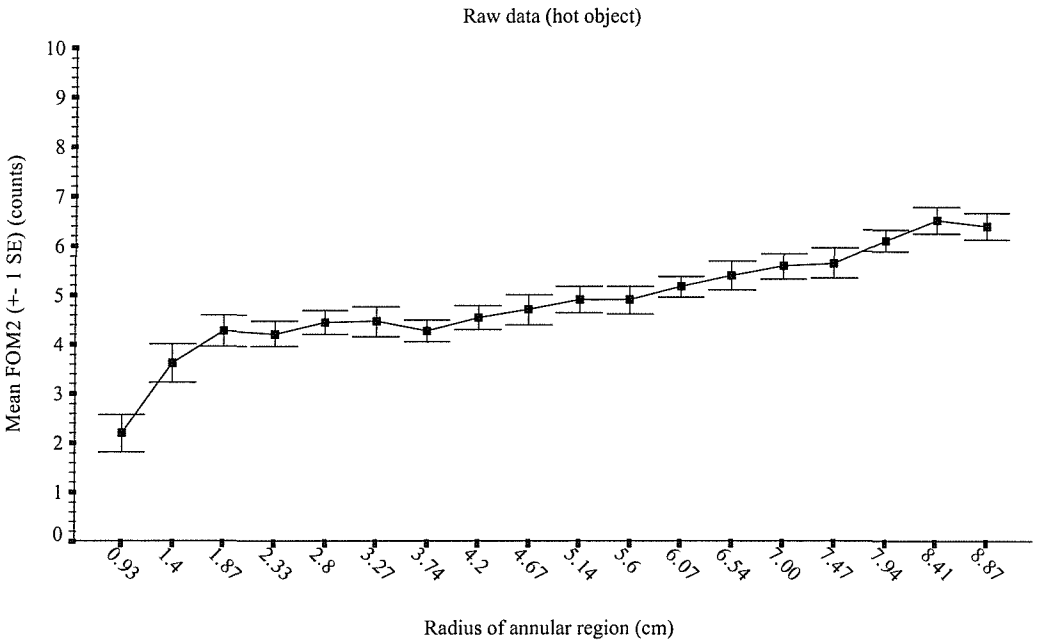

Figure 4.14: The mean for the figure of merit of the first solution for a 1.0 cm simulated hot object for the raw data solution using different widths for the different BKG regions.

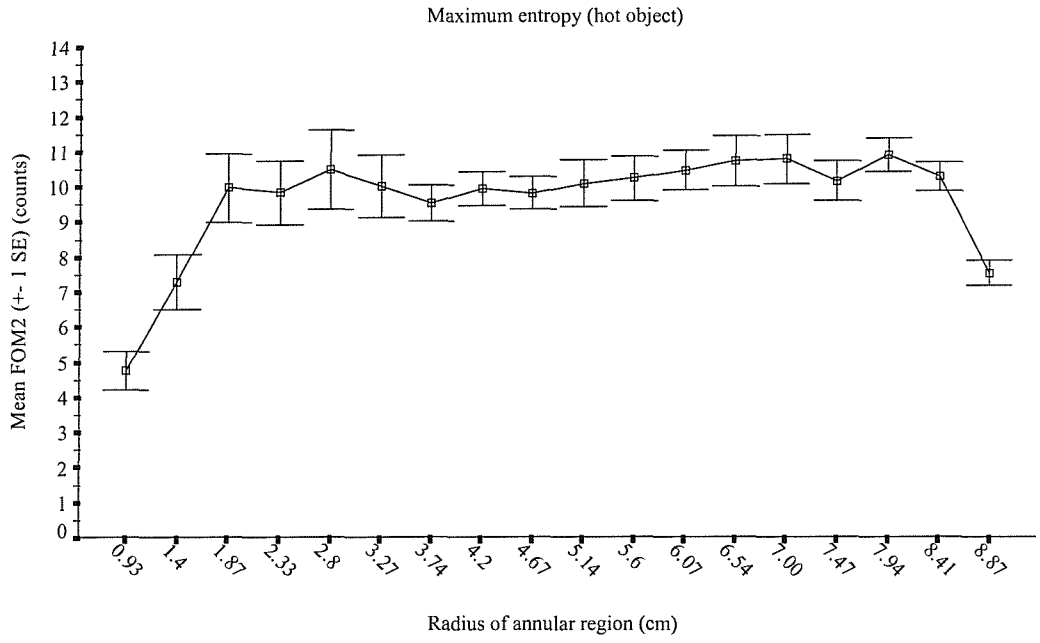

Figure 4.15: The mean for the figure of merit of the first solution for a 1.0 cm simulated hot object for the maximum entropy solution using different widths for the different BKG regions.

4.4 Discussion

For the figures of merit to be of value in providing a measure of object detectability they must be reliably determined. The figure of merit used in nuclear medicine image quality calculation depends on defining a surrounding background (SBKG) region. In this investigation influence of the location of the surrounding background region was studied by altering the size and position of these regions.

The noise level in this study was defined as the variability in the count in the chosen surrounding background area measured by the standard deviation of the counts in this area. The calculation of the standard deviation of the counts in the raw data

shows essentially a constant result as the size and position of the SBKG region was changed. As the area surrounding the object is uniform and the standard deviation is the square root of counts per pixel in that area, it is expected to be constant. When the SBKG region was close to the cold object the counts tended to be less due to the proximity of the object. That meant by getting closer to the object the level of count was less and hence lower standard deviation (Figure 4.4). This resulted from the limited gamma camera resolution. Also the regions closer to the object are smaller in size, therefore there was a greater variation in noise estimate due to random statistics (Figure 4.4). As the SBKG region was getting very close to the edge of the image the standard deviation was increased and this was due to the limited gamma camera resolution (Figures 4.2 and 4.4).

If only one study is considered (Figure 4.3), misleading results could be obtained. This was due to the considerable variation in the noise level due to random statistics particularly in the smaller inner regions. Different realisations were therefore simulated and the results averaged to obtain a more robust measurement of the noise (Figure 4.4).

The results of figure 4.6, shows how the contrast value is varying widely as the position and size of the SBKG region is changed. For the inner SBKG regions in the area very close to the object, there was a gradual increase in the contrast value, with the radius of SBKG region. This was followed by a reasonably constant contrast value for regions of radii between 2.0 cm and 4.0 cm . The reduction of contrast for SBKG regions close to the object was due to the limited gamma camera resolution influencing the counts in the region. The gradual decrease in contrast with radii between about 4.0 cm and 8.0 cm for the cold object can be explained by reduction in scatter contribution towards the edge of the image compared to the centre. The rapid drop in the contrast value for the cold object as the regions started to approach the edge of the image was due to the limited gamma camera resolution.

There were consequently substantial variations in the FOM (Figure 4.8), of the object. These findings will help in defining a reliable rules for drawing the SBKG region in a consistent manner.

When the hot object was used in this study it showed similar results compared to the results obtained with the cold object (Figures 4.10,4.12,4.14). The similarities were clear when figures 4.4, 4.6 and 4.8 were compared to figures 4.10, 4.12 and 4.14. However there was an apparent increase in the contrast value and the FOM, as the SBKG region approaches the edge of the image. This was an artificial increase due to the fact that the count level in the surrounding background is falsely low. There was a reasonably constant value of contrast and FOM for regions between R03 (1.87 cm) to R08 (4.20 cm), which was similar to the result obtained from the cold object. This evidently will help in defining the rule for drawing the SBKG region.

From this study it was clear that there was an improvement in the contrast value and the FOM as the raw data had been processed by maximum entropy technique (Figures 4.7 and 4.9 for the cold object and figures 4.13 and 4.15 for the hot object). There was an increase in the contrast value in the area between R03 to R08, from -16.7 in the raw data to -21.9 in the maximum entropy solution, (Figures 4.6 and 4.7). Similarly, the FOM was increased from -4.0 in the raw data to about -8.0 for maximum entropy solution (Figures 4.8 and 4.9). There was a lower drop in contrast value with maximum entropy than with the raw data (Figures 4.6 and 4.7), between 4.0 cm and the edge of the image. This is expected as the process of maximum entropy is restoring the scattered counts which give rise to this effect to their correct location.

4.5 Conclusion

This investigation has shown that the image quality calculation when using a measure of noise, contrast level and figure of merit, depends on the position of the surrounding background region in the image. Defining this region very close to the edge of the object or very close to the edge of the image, will affect the image quality calculation, by the influence of scattering and limited gamma camera resolution. The optimal or the most constant results were obtained in the areas between R03 to R08. Therefore a rule for defining the position of the SBKG region is recommended for the calculation of the image quality. The region should be

located at a distance between 2.0 cm to 4.0 cm away from the edge of the object. It should also not include pixels closer than 1.0 cm from the edge of the uniform area, to avoid the influence of the imaging system resolution.

Chapter Five

Investigations on the use of Maximum Entropy, Wiener Filter and Conventional Smoothing Techniques in Processing Simulated Images

5.1 Introduction

The earliest attempts at image processing in nuclear medicine used pure smoothing filters to improve the signal to noise ratio of images (Tauxe et al 1966, Budinger 1973, MacIntyre 1973, Berch et al 1974, Pizer et al 1978, Lange et al 1977). An example is the nine-point smoothing algorithm which is widely used (Starck and Carlsson 1997). Another class of image processing technique consists of those for correcting for loss of resolution caused by the imaging device such as Wiener filter (Skarsgard et al 1961, Iinuma and Nagai 1967, Di Paola et al 1983). One characteristic of clinical images, which has continually created problems, is that the required signal for detection or enhancement is very poorly defined. This complicates the evaluation of image processing techniques, because the true distribution of activity to be used as a gold standard is not known. For this reason image simulation studies were used in this investigation. Known abnormalities can be introduced during the simulation process and interpretation of the simulated images judged against this standard. The aim of this study is to evaluate the use of maximum entropy, Wiener filter and conventional smoothing in processing nuclear medicine images. Simulated images have been produced and processed extensively with the different techniques. Simulation was used

for the variety of distributions in the image that can be created and investigated and the ability to study systematically, the effects of various factors in the image, on detection and localization of features.

Image quality may be assessed quantitatively using a figure of merit based on contrast to noise ratios. From the previous investigation (Chapter 4), a consistent method of measuring a figure of merit (FOM) was developed. One of the questions we wish to address here is how the FOM relates to the visual detectability. As has been mentioned earlier (Chapter 3), there was a lack of correspondence between the figure of merit as a quantitative measure and visual assessment (i.e., visual appearance) of the images, therefore, a subjective assessment for the image detectability is essential for comparison. The different techniques will be evaluated in their ability to detect known abnormalities and compared both to each other and the raw unprocessed images. The evaluation will be carried out (i) by assessing the figure of merit of abnormality detection as described in previous chapter and (ii) by using Receiver Operating Characteristic (ROC) analysis of visual interpretation of the images. The confidence levels of visual detection found in the ROC experiment will be compared with the FOM determined using the techniques described in the previous chapter. This will allow FOM to be related to object detectability.

5.2 Methods

5.2.1 Simulation

All the images used in this study were produced using the simulation technique (Fleming and Simpson 1994, Fleming 1996) which has been explained earlier in chapter 4. A series of images in two sets were simulated. The first set consisted of images used for determining certain parameters which were required for the processing techniques. The second set of images consisted of images which were used for image interpretation. The first set of images had also been used previously for the investigation in chapter 4. It consisted of 13 realisations simulated with a single cold object of size 1.0 cm located in the centre of a planar area of uniform activity of size 18

× 18 cm. The second set consisted of 40 images, each simulated with one, two or three objects of variable size (0.5 cm and 1.0 cm) and variable contrast, and located in distributed planar area of uniform activity also of size 18.0 cm square. Objects of this size were close to the threshold of detectability. The object appears as a square cold area representing the cold object with no radioactivity located in the distributed area. The actual counts in the surrounding background area is 400. Accordingly, to have objects with varying clarity (true contrast), the number of counts in these cold object areas were varied. Ten objects had zero count in the object area (maximum contrast), 36 objects had 100 counts and 10 objects had 200 counts. The visual appearance of the objects with zero count is better than the objects with 200 count. The number of objects with different sizes and true contrast are presented in table 5.1.

Number of count in the object areas for the three type of object	Size and number of objects		
	0.5 cm	**1.0 cm**	
	number of objects	number of objects	Total number of objects
0 count	5	5	10
100 count	19	17	36
200 count	5	5	10
			56

Table 5.1: The numbers of objects with different sizes and level of contrast, which were used in the study. The visual appearance of the object decreases with increasing the number of counts in the object area.

The images were simulated so that the total count was 200 - 220 k. Statistical noise was added using Poisson distribution. The object area in the first set of images is an area without any activity and appears as a cold object. These images are known as abnormal cold images due to the presence of the cold object within the distributed area. The objects in the second set of images varied in contrast, to provide images both above and below the threshold of detectability and to check the ability of the different image processing techniques.

In order to compare the ability of the techniques to identify correctly images with no abnormality another similar series of 20 noisy images were simulated without any object in the distributed area. These images are known as normal images.

The simulation technique was based around the performance of an ADAC Pegasys gamma camera fitted with a low energy general purpose collimator.

The planar source was positioned 13.0 cm from the camera with 11.0 cm of water equivalent attenuating material between it and the camera face. A 128 × 128 matrix size was used which corresponded to a pixel size of 4.67 mm. The isotope modelled was ^{99m}Tc, collected with a symmetric 20 % energy window centred around 140 keV.

5.2.2 Image Processing Methods

The original simulated images are referred to as raw data images, as they did not undergo any image processing procedure. Afterwards each image was processed separately by maximum entropy (ME), Wiener filter (WF) and conventional smoothing (SM) techniques. A comparison of the maximum entropy processing technique was made with these commonly used image processing techniques. Conventional smoothing was an example of a pure noise suppression technique. The WF technique was chosen due to the similarity with ME technique. The WF method has been formulated in an attempt to produce optimum restoration of the inherent image quality lost during the imaging process, while at the same time suppressing the noise (King et al 1983, Sharp et al 1989).

5.2.2.1 Maximum Entropy

The maximum entropy technique requires the specification of a number of parameters for its operation. The first parameter to be specified is the initial solution for the algorithm known as the default solution. For this the raw data image was convolved with a smoothing operation using Fast Fourier Transforms, which is faster than spatial

convolution. The convolution produces a smoothed image, of the raw data. The number of smooths was set to 5 smooths for the optimum detectability as suggested in chapter 3. The use of a filtered image of the original data as the default enables the total count in the image to be maintained. The algorithm requires two parameters to be entered as constants, C_1 and C_2 which define the data errors (equation (2-12)). The choice of those two constants produces solutions with varying compromises between noise and resolution.

5.2.2.2 Wiener Filtering

The Wiener filter image processing technique, is an inverse filter. It enhances intermediate frequencies and reduces high frequencies.

This filter requires previous knowledge of the object and of the noise, in particular their power spectrum. Knowledge of the process of blurring is also needed, so it needs to know the transfer function (MTF) of the gamma-camera. The Wiener filter is defined (Pratt 1991) as :

$$F(u,v) = \frac{H^*(u,v)}{|H(u,v)|^2 + \frac{{}_n(u,v)}{{}_f(u,v)}} \qquad (5\text{-}1)$$

where H(u,v) is the MTF of the gamma-camera, which is the Fourier transform of the PSF, H* (u, v) is the conjugate of H(u, v), ${}_n$(u, v) is the power spectrum of the noise and ${}_f$(u,v) is the power spectrum of the object. So Wiener filtering attempts to recover a blurred object by incorporating the system modulation transfer function (MTF) and its noise characteristics.

Wiener filtering has been widely used for the problem of planar deconvolution of nuclear medicine images (King et al 1983, Boulfelfel et al 1992, Shao et al 1994). It has been used in gated cardiac blood-pool images of thallium-201 (Miller et al 1984), with heuristic modifications on the filter to adapt it better to this kind of image. Wiener filter

has also been applied to SPECT (Single Photon Emission Tomography) images (Hon et al 1989).

The Wiener filter image processing program which was used in this investigation was one of several software applications which were part of the Vision software package (SMV America, Software, USA). It required the point spread function FWHM (1.0 - 16.0 mm) to be input. It assumed that the ratio of the power spectrum of noise to that of the object was constant and equal to 0.15 [i.e., ($_n(u, v)$ / $_f(u,v)$ in equation 5-1].

5.2.2.3 Conventional Smoothing

Conventional smoothing as a simple data processing technique was also used for processing the simulated images. It is commonly used for reducing noise in radionuclide images. Conventional smoothing is different from maximum entropy and Wiener filter techniques, in that it is not a deconvolution technique but it reduces noise at the expense of some reduction in contrast. The smoothing operator replaces each pixel value by a weighted sum of itself and the eight surrounding pixels with the following weighting scheme:,

$$\begin{matrix} \frac{1}{16} & \frac{2}{16} & \frac{1}{16} \\ \frac{2}{16} & \frac{4}{16} & \frac{2}{16} \\ \frac{1}{16} & \frac{2}{16} & \frac{1}{16} \end{matrix}$$

Thus each image was smoothed four times, producing four solutions corresponding to variation in the number of passes of the filter between 1 - 4. As the number of passes of the filter was increased, the contrast of the image decreased. A typical contrast noise

graph for a defect in a simulated image as the number of passes of the filter is varied is shown in figure 5.3 (section 5.3.2.1). After one smooth the noise reduces rapidly with relatively little loss of contrast. Further smoothing reduces the noise considerably less than the first smooth and, therefore, it was recommended to use one pass filter for the comparison.

The smoothing filter used was incorporated within PICS Program (Fleming et al 1991).

5.2.3 Determination of Processing Parameters for Comparison

The purpose of the experiment was to compare the image quality of the different processing techniques. However each technique produced a range of solutions which had a different compromise between contrast and noise. In comparing them it is important to ensure that the solutions used in the comparison are chosen in a consistent manner. Ideally a measure obtained from the image itself should be used and in this study the level of noise in the image as measured by the standard deviation in a uniform area was chosen. It was decided to select a fixed value of noise and then to examine the solution from each technique giving that noise value. The value of noise chosen was that corresponding to one smooth of the data. The reasons for this choice were :-
(i) that one smooth considerably reduced the noise in the images with only minimal reduction in contrast and so was a reasonable choice for the smoothing process.
(ii) both the other techniques had continuously variable parameters to control the noise level of the solution. This could then be adjusted to give the same noise level as one smooth. The smoothing used in this study only gave discrete solutions based on the number of passes of the filter and could not have been used in this way if one of the other techniques had been used to set the noise level.

Accordingly the first set of images which consisted of 13 different realisations of each of the cold object distributions were created. The technique used for simulating these realisations was as explained above. Subsequently each of the 13 realisations were processed individually by maximum entropy, Wiener filtering and conventional smoothing techniques.

For processing the 13 realisations by maximum entropy the value of parameter C_1 was varied between 0.2 - 1.0 . and the value of parameter C_2 between 0.0 - 5.0 . That resulted in producing different images with varying quality.

For processing with the Wiener filtering technique, specification of the point spread function FWHM was required. Each image was processed with the FWHM value varying between 2 and 12 mm .

Afterwards image quality was assessed using PICS Program (Fleming et al 1991). Regions of interest were defined around the cold object and a background region (SBKG region) in the distributed area, according to the technique explained in chapter 4. The program calculated the object contrast and the standard deviation (level of noise) in the distributed region. The values for each type of processing were averaged over the 13 images to get a better estimate of the image quality measures. Contrast-noise plots of the averaged results from raw data, conventional smoothing, maximum entropy and Wiener filtering techniques, were plotted for the cold objects. These results enabled definition of the value of parameter C_1 for maximum entropy and the FWHM of point spread function for Wiener filtering which would give the same noise level found using a single pass of the filter for the conventional smoothing.

5.2.4 Defining the Value of Parameter C_2

As the value of C_1 was defined, subsequently the value of C_2 needed to be chosen according to the same principle. In this investigation it was decided to use the 40 realisations which were simulated earlier (section 5.2.1), for the variety of reasons. Each simulated image contains objects of diameter 0.5 cm or 1.0 cm, positioned within the distributed area. These objects also varied in contrast to test the similarity in results with different contrast levels. Each image appeared as an area with reasonably uniform activity superimposed by one or more areas of reduced counts representing cold objects. Normal images also need to be obtained for comparing these abnormal cases, therefore, another set of 20 realisations were simulated without any object in the distributed area. Each image was processed by ME using the value of C_1 defined by the above

experiment and several different values of C_2 covering the range of convergence. The image contrast and noise of each of the solutions was assessed using the standard protocol. The C_2 value at which the noise level equalled that of one smooth of the data was noted. The average value of C_2 from all images was calculated and taken as that to be used to create solutions for the subsequent observer interpretation study.

5.2.5 Image Evaluation

Image evaluation needs to be performed for measuring the effectiveness of different image processing techniques. As important as the development of a new technique, testing its ability to improve image quality is essential.

In medical image processing the ultimate test of the technique is its effectiveness in improving the clinical application of the images. However, such experiments are quite difficult to perform and relatively few have been carried out. The following reference contain some examples (Neill and Hutchinson 1971). The other general approach has been to look for objective quantitative parameters of image improvement. One approach which is widely used for image evaluation is that of distance metrics such as the root mean squared distance between the reconstructed images and known "true" images. However other workers restricted the use of this approach and append some conditions regarding its medical relevance and significance (Penney et al 1990). They found out that there was a lack of correspondence between normalised mean squared error and visual appearance.

Other groups have used image contrast (King et al 1984, Webb et al 1985), resolution (Arlig et al 1997), the level of noise in the image (Boulfelfel et al 1992) and signal to noise ratio (Kinahan and Karp 1994), as measures for image evaluation.

The approach taken in this study is to consider that the detectability of abnormalities depends on both contrast resolution and noise in the image and therefore, that it can be assessed and evaluated by measuring contrast-to-noise ratio.

The task in this study is to evaluate the difference between the three image processing techniques in detecting an abnormality in an image. This should be related to the relative quality or merit of the three image processing techniques. Measuring this merit with a high degree of confidence was recommended by Herman and Yeung 1989 and others (Hanley 1989). This can be achieved with the widely used receiver operating characteristic (ROC) analysis of subjective human observer performance. This approach is the ultimate test of observer ability in detecting an abnormality. The problem with ROC analysis, using human observers is its complexity and hence, cost. Therefore an alternative approach which is less complex and less costly, is the numerical observer (FOM). This approach is known as a "figure of merit" (FOM), of visual detectability of detail in an image (Herman and Yeung 1989, Furuie et al 1994).

The numerical observer approach (FOM), has been used previously for investigation in chapter 3, and it was shown that there was an apparent lack of correspondence between the figure of merit used (i.e., FOM2) and the visual appearance of the images. Therefore in view of the doubt over the ability of FOM to adequately predict detectability it was decided to carry out ROC analysis in addition to calculation of FOM2. Hence as part of this investigation it was possible to compare the results obtained from the FOM2 approach with these from the ROC analysis approach.

In this study the simulated images obtained by the maximum entropy image processing technique will be analysed and compared with the original images and the results obtained by using the other two image processing techniques: Wiener filtering and conventional smoothing. The set of 40 simulated images were used, each with one or more cold objects of variable size (0.5 cm and 1.0 cm), and located in the distributed area. Another set of 20 normal image were simulated accordingly for comparison.

Each image obtained was processed by the three processing techniques (conventional smoothing, maximum entropy and Wiener filter), using the required parameters as determined from the previous investigation (see sections 5.2.3 and 5.2.4). The total number of images obtained after the processing were 240, of which 160 were abnormal image, (images with cold objects abnormality) and 80 were normal image (images without any abnormality).

5.2.5.1 Figure of Merit

Measures of contrast and noise were used to calculate the figure of merit, as a mathematical parameter to measure image quality (Herman and Yeung 1989). An investigation described in chapter 3 has been carried out to compare three different figure of merits (FOM1, FOM2 and FOM3), in calculating the image detectability. It was found that FOM1 and FOM3 values were dependent on the size of the surrounding background region, and therefore the FOM2 was chosen to be used for the calculation of image detectability. It is a simple contrast to noise ratio (Chesters 1992) and is independent of the size of the surrounding background region. Thus FOM2 was calculated for all the images in this investigation using the method described in chapter 4, for selecting the surrounding background region. The parameters required by the processing techniques were chosen as described above, so that only one processed image was obtained for comparison from each technique.

In evaluating the quality of the images obtained, figure of merit (FOM2), was calculated for each of the 240 images, for both raw and processed data. The PICS Program (Fleming et al 1991) was used to calculate the image quality of the images obtained, following the same technique which was used for calculating the contrast level and the standard deviation of the images (Chapter 4).

5.2.5.2 Receiver Operating Characteristic (ROC) Analysis

Receiver operating characteristic (ROC) analysis is a procedure, derived from statistical decision theory, that was developed in the context of electronic signal detection (Green and Moses 1966). It is used to evaluate the accuracy of different diagnostic and prognostic technologies. It is particularly relevant for conducting observer performance tests, with real or simulated clinical cases to evaluate diagnostic systems that require subjective observer interpretation (Hanley 1989).

Receiver operating characteristic (ROC) analysis has been used in a broad variety of medical imaging studies (Metz 1986). It is an effective way of performing the task of

evaluating nuclear medicine image processing techniques (Houston 1985). ROC methodology accounts for the sensitivity and specificity of the image processing technique depending on the particular "decision criterion" or "critical confidence level" that a user chooses to adopt in distinguishing between nominally "positive" and nominally "negative" results (Metz 1989). In the diagnostic outcome there are two kinds of correct responses and two kinds of incorrect responses. Taking the distinction between abnormality and normality as example, the correct responses are termed true-positives (TP) and true-negatives (TN). In the former, for instance, the abnormality in question was present, and the diagnostic system indicated that it was present; in the second instance, the abnormality was not present, and the diagnostic system indicated that it was not present. The two kinds of incorrect outcome are termed: false-positive (FP) and false-negative (FN). In a false-positive outcome, the abnormality is absent, but the system decides that it is present; in a false-negative outcome, the abnormality is present, but the system decides that it is absent. So in this context any assessment of diagnostic performance requires some comparison of diagnostic decisions with truth. The simplest measure of diagnostic decision quality is the fraction of cases for which the observer (e.g., the physicians) is correct, which is often called "Accuracy". Therefore sensitivity and specificity represent two kinds of accuracy which gives the ROC plot: the first for actually positive cases and the second for actually negative cases. Thus both sensitivity and specificity can be calculated as follow:

$$Sensitivity = \frac{Number\ of\ true\ positive\ (TP)\ decisions}{Number\ of\ actually\ positive\ cases} \qquad 5\text{-}2$$

and

$$Specificity = \frac{Number\ of\ true\ negative\ (TN)\ decisions}{Number\ of\ actually\ negative\ cases} \qquad 5\text{-}3$$

The ROC curve is a plot of sensitivity (the true positive fraction) on the y axis against 1-specificity (the false positive fraction) on the x axis. The ideal ROC curve is the line

y = 1 at one level of discrimination all the objects are visualised with no false objects being detected.

ROC analysis has been used to evaluate the performance of a broad range of diagnostic systems. The first ROC curve in diagnostic radiology was calculated by Lusted (1960), who reanalysed previously published data on the detection of pulmonary tuberculosis to show that apparent differences in diagnostic performance could be explained in terms of the ROC model. Also ROC methodology has been used for investigation in chest radiography (Goodenough et al 1973, Lassen and Bloch 1978, Kundel et al 1979, Herman et al 1982, Kelsey et al 1982, Revesz et al 1982, Kelsey et al 1982, Kelsey 1983) and mammography (Ackerman and Gose 1972, Starr et al 1975, Goin et al 1983, Gohagan et al 1984). Several investigators have used ROC analysis to study the clinical utility of computed tomography in specific organ systems (Dendy et al 1977, Ritchings et al 1979, Meany et al 1980, Warren 1981, Abrams et al 1982, Hesel et al 1982, Fukushisha et al 1984, Judy et al 1985). In ultrasonography the utility has been assessed in pregnancy testing (Blackwell et al 1975, Uchida et al 1979, Niederau and Sonnenberg 1984). In radionuclide imaging ROC methodology has been used to compare a conventional scintillation camera and the Anger tomographic scanner for detection of brain lesions (Turner et al 1976a, Turner et al 1976b, Brown et al 1980). The diagnostic reliability of individual image features in liver scintigraphy (Simon et al 1981) and in lung scintigraphy (Sullivan et al 1983) has been investigated too. Myocardial perfusion imaging was studied as well (Cuaron et al 1980, Wiener et al 1980). Gated imaging technique in lung scintigraphy for the detection of pulmonary emboli was compared to other technique (Alderson et al 1979). Investigators at the University of Aberdeen evaluated single-photon emission computed tomography (SPECT) in brain (Carril et al 1979) and liver (Dendy et al 1981) imaging, using the ROC analysis. SPECT was compared with conventional scintigraphy in liver-spleen imaging by another group at the University of Michigan (Keyes et al 1984). A study by Hermann et al (1982) surveyed the ability of different laboratories to detect simulated lesions in a standard scintigraphic phantom. Various different studies have used ROC analysis to investigate the effectiveness of image processing techniques (Kundel 1972, Andrus et al 1975, Herath and Sharp 1976, Houston and MacLeod 1977, IAEA Third progress report 1977,

Houston et al 1979, Pullan et al 1980, Armstrong et al 1983, Miller et al 1984, Lehr and Capek 1985).

In simple ROC analysis the observer views images some of which contain a single abnormality and the rest of which are normal. However clinicians normally recognise that common diagnostic tasks are not equivalent to simple yes / no decisions. The correct diagnosis of a tumour or a microcalcification for example, also requires the accurate specification of its location. ROC analysis cannot take into account this location information. For example, an observer could miss a lesion that is present and mistake a noise feature located somewhere else on the image for a lesion, and this performance would be scored similarly to that of a observer who correctly detected the lesion without detecting the noise, that is, both responses would be scored as true-positive case. ROC methodology does not allow for multiple abnormalities per image. While some theoretically useful attempts have been made at overcoming these limitations (Starr et al 1975, Metz et al 1976), they have their own limitations and do not apply to clinical tasks in which the observers has to detect and locate multiple nodules on the same image. Thus location ROC (LROC) analysis has been used (Starr et al 1975) to directly measure the ability of an observer to detect the presence of a single case of a particular kind of abnormality in an image and to localise it. It has been suggested by Swets and Pickett (1982) that LROC analysis can also be used to measure the ability of observers to detect and classify abnormalities. A generalisation of the LROC approach, called free-response operating characteristic (FROC) analysis (Bunch et al 1978) applies to the situation in which a particular kind of abnormality may be present at more than one location in an image and the observer is required to detect the presence of the abnormality at each of its locations. Unfortunately, LROC and FROC analysis share two substantial practical limitations: no formal curve-fitting procedures and no generally applicable statistical tests for differences in performance have been developed. Thus as it has been suggested (Metz 1989), neither LROC nor FROC analysis can be recommended broadly.

In this investigation ROC analysis will be used to evaluate the results obtained from, maximum entropy, Wiener filtering and conventional smoothing, image processing techniques, in processing the simulated images. Applying ROC analysis to the results

obtained from the three image processing techniques will allow them to be compared based on the performance of the interpreter (i.e., the reader) using the images to give a diagnostic decision. The images used in this investigation contain more than one object located in different places within the images, therefore, a simple method has been developed using ROC analysis approach, to measure the ability of observers to detect and classify abnormalities present at more than one location in the image. This method treats each abnormality as an individual feature to be detected and the normal area in an image containing an abnormality as a separate normal feature. This means for example that an image with a single abnormality is treated as two objects one normal and the other abnormal. Conventional ROC analysis can then be applied to the results of observation on all the objects. This is equivalent to the so called AFROC approach described by Chakraborty (1990).

5.2.5.2.1 Design of Experiment

Comparing the different image processing techniques, using ROC analysis, the 240 images were saved in one file. The images were randomly ordered, to enable the observer reading the images avoiding any reading-order effect (Metz 1989). The randomisation was obtained by locating each of the raw data images and its processed images, in different location order in the file. This was done to avoid locating the raw data image and its processed images close to each other. The observers were instructed that the experiment was designed to test their ability to detect any abnormality on the images and also, to test the ability of the three different image processing techniques. In order to familiarise the observers with the nature of the experiment, a warm-up period was conducted on a training data set as a training session. Then each observer was provided with a two-page set of "Instructions to Observer", describing the task and defining carefully the nature of abnormalities to be reported in the real study, to clarify the procedure which needs to be followed in reading the images. They were instructed to interpret each image as follows:-

(i) To detect the object and its location in each image and subdivide his/her response to each image in the file, into five levels of confidence if using the discrete rating scale as the following rating scale:

1 = Definitely no cold object present.

2 = Fairly certain no cold object present

3 = Equivocal

4 = Fairly certain a cold object present

5 = Definitely a cold object present

Alternatively if the continuous rating scale was used a subjective probability estimate (ranging from 0% - 100%) was made as follows:

0% - 9%	= Definitely no cold object present
10% - 39 %	= Fairly certain no cold object present
40% - 75 %	= Equivocal
76% - 89 %	= Fairly certain cold object present
90% - 100%	= Definitely cold object present

(ii) The object is located in one of the locations in the image, A to I, as indicated in figure 5.1a .

(iii) If no object were detected and a decision were given such as " *Definitely no object present*" then that image box should be ticked (✓) only.

(iv) If a decision is made the observer needs to fill in the location of his/her response according to the corresponding level of confidence.

(v) There is no time restriction for interpretation of each image.

(vi) The observer is free to change the display size, the contrast and the brightness of the images according to his/her need (i.e., to use the workstation fully), however no image processing is permitted.

(vii) Each observer is free to repeatedly change his/her response to each image until a decision is made.

(viii) If any ambiguities are raised, they can be discussed individually with the researcher.

Also they were provided with a set of tables, for the 240 images which were to be completed so as to contain the level of confidence and the location of each object in the image (Figure 5.1b).

Two observers interpreted the data one using a Sun SparcStation 2 (Sun Microsystems, Mountain View, CA) to display the images and, the other a Vision workstation (SMV, BUC, France).

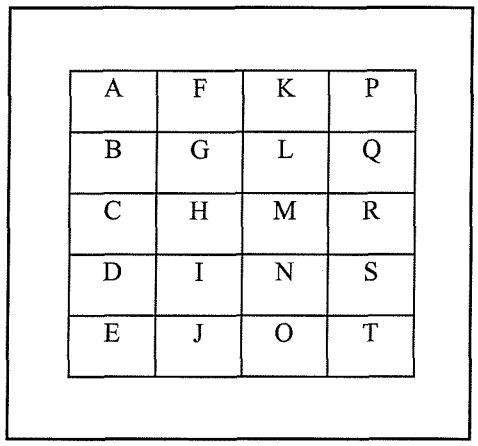

(a)

Image number : 1

Level of confidence	Percentage of confidence for each location (%)																			
	A	B	C	D	E	F	G	H	I	J	K	L	M	N	O	P	Q	R	S	T
Definitely no cold object present	✓		✓		✓	✓	✓		✓	✓	✓		✓	✓	✓	✓	✓	✓	✓	✓
Fairly certain no cold object present		20																		
Equivocal				45																
Fairly certain a cold object present								85												
Definitely a cold object present												100								

(b)

Figure 5.1: In this diagram (a): is an example of an image with different objects distributed within different locations in the distributed area and some of the locations does not have any objects. (b): is an example of a table filled with a decision made by an interpreter, indicating the level of confidence and the Percentage of confidence for each location (%).

5.2.5.2.2 Analysis Technique

Receiver operating characteristic (ROC) analysis was applied to the results of all the images obtained above. In this experiment, two experienced observers {one nuclear medicine physician (consultant) and one nuclear medicine physicist (consultant)}, each reported the 240 simulated unprocessed and processed images, according to the instructions given above. The result of the experiment from each observer was collected, categorized and then analyzed using the ROC program, developed by Metz et al (1990), which are based on the Dorfman and Alf approach (1969).

This program calculates maximum-likelihood estimates of binormal ROC curves, including the area under each curve and its standard deviation, from data collected on either discrete and continuous scales. The purposes of ROC program are to calculate the statistical significance of the difference between two ROC curve estimates using, (i) the **Area Test,** for testing the difference between the areas under the two ROC curves and, (ii) the **True and False Positive Test,** for testing the difference between the true- positive fractions (TPFs) on the two ROC curves at a selected false-positive fraction (FPF).

In this study both values have been recorded but more attention paid to the true positive fraction statistical test at a low value of false positive fraction as an operating point, as this was considered more representative of the clinical situation. The statistical significance was calculated between the result obtained from the raw data, conventional smoothing, maximum entropy and Wiener filtering. Six comparisons were made as follows:

(i) Raw data versus Conventional smoothing
(ii) Raw data versus Maximum entropy
(iii) Raw data versus Wiener filtering
(iv) Conventional smoothing versus Maximum entropy
(v) Conventional smoothing versus Wiener filtering
(vi) Maximum entropy versus Wiener filtering

5.2.5.2.3 Confidence-Rating Scales:

Receiver operating characteristic (ROC) studies comparing observer performance under different medical imaging conditions have involved data collected on a discrete or continuous scale. In the approach of a discrete confidence-rating scale, five categories (e.g., definitely absent, fairly certain absent, equivocal, fairly certain present and definitely present) can be used by the observers to report their confidence in performing a two-alternative decision task for each case. This will allow a smooth ROC curve to be fited to the data, if the scoring pattern is well-distributed (Metz 1989, Rockette et al 1990). The continuous rating scale allowed a subjective probability estimate ranging from 0% - 100%, that an abnormality was present (Swets et al 1991). An experimental comparison to measure observer performance in the detection of abdominal masses in a multi-observer ROC study has been performed comparing continuous and discrete confidence-judgment scales (Rockette et al 1992). The continuous rating scale has been found to be more reliable than discrete scale and therefore, it was recommended to be used for routine radiological studies, due to its potential advantages in approximating clinical reporting more closely and in increasing the likelihood of successful ROC curve fitting.

Finally as mentioned earlier in chapter 3, a lack of correspondence was observed between the figure of merit and the visual appearance of the images. Accordingly the figure of merit was studied for any correlation with receiver operating characteristic (ROC) analysis. This was performed by investigating any linear trend between the detectability of the images obtained from the calculated image quality (FOM2) and the perceptual interpretation that had been made for the images as part of the ROC analysis (Readers decision).

The SPSS software (Statistic program for social studies) was used to calculate these correlation's.

5.3 Results

The results will be divided into three parts. (i) the simulation of the images used in the study. (ii) the determination of the operating parameters for the image processing techniques which have been used in the study. (iii) the image evaluation experiment.

5.3.1 Simulation of the Images

Two set of simulated images were used in this investigation, the first set consisted of images with a single object located in the centre of the distributed area. The second set of images consisted of a mixture of normal and abnormal simulated images. Each image contained one or more objects located in the distributed area. These varied in size and contrast (Figure 5.2).

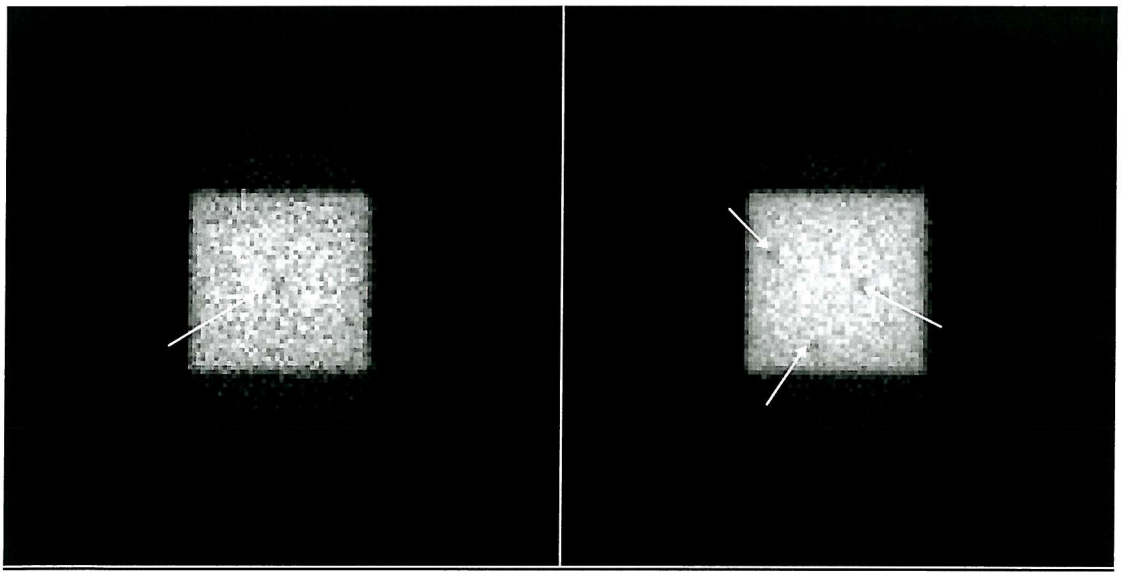

(a) (b)

Figure 5.2: Example of the simulated images used in the study (a) is a planar image with a single cold object located in the centre of the image (b) is another planar image with three objects different in size and located in the distributed area. The arrows indicate the location of the objects.

5.3.2 Determining the Parameters Required by the Processing Techniques

5.3.2.1 Conventional Smoothing

Smoothing the images conventionally using 1 - 4 passes of the nine point filter was studied. One smooth of the data numerically reduced the noise from 8.0 to 3.0 counts while only reducing contrast from 15.3 to 11.3 counts. Smoothing between one and four passes reduced contrast further while reducing noise at a much decreased rate (Figure 5.3). Therefore for conventional smoothing one pass filter was determined for processing the images. Contrast / noise analysis was also applied to the images in the second experiment in which variable contrast objects were studied. For one pass of the smoothing filter the average noise level was found to be 6.0 .

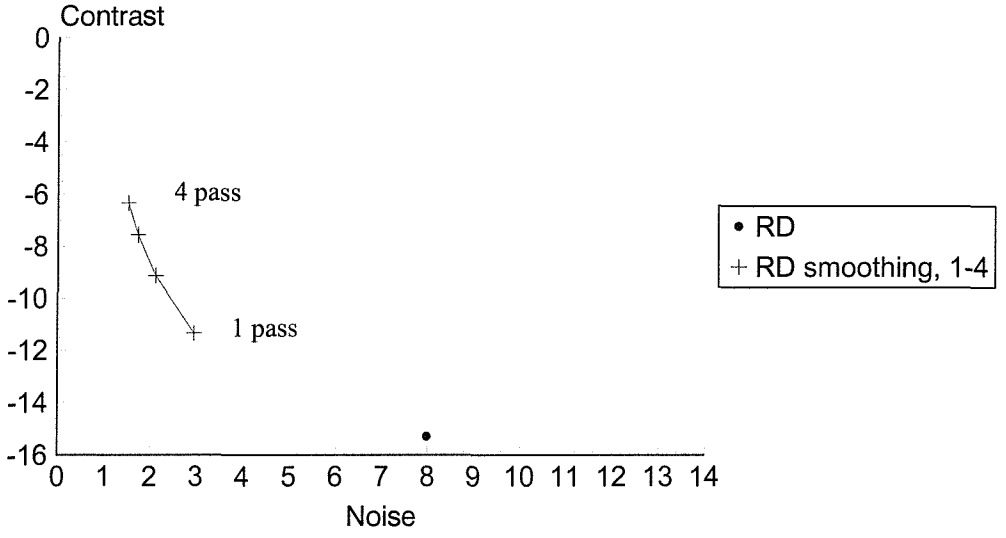

Figure 5.3: Variation of mean contrast with mean noise, with varying degrees on conventional smoothing applied to the data set with one cold object. Smoothing the raw data between one and four passes of the filter reduced the contrast while reducing noise at a much decreased rate.

5.3.2.2 Maximum Entropy

Maximum entropy image processing technique, gives various different solutions when varying the value of parameters C_1 between 0.2 - 1.0 and C_2 between 0.0 - 5.0. In some of these both contrast and noise were improved simultaneously (figure 5.4).

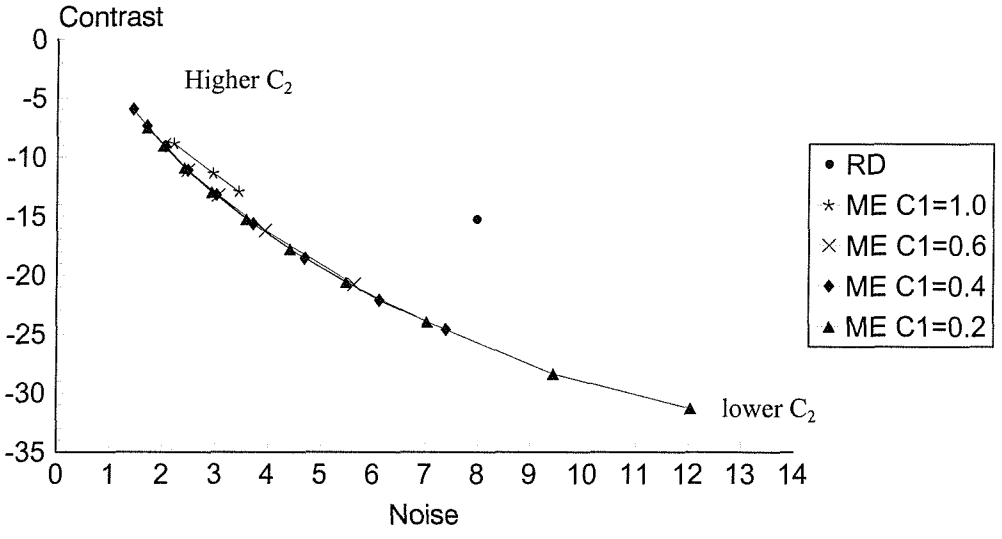

Figure 5.4: Plots of mean contrast against mean noise for maximum entropy processed images with varying the value of C_1 between 0.2 - 1.0 . Note that the contrast of the object is negative as it is a cold object.

At C_1 = 0.2 the range of convergence obtained with varying C_2 was high. However the image with the highest contrast (i.e., the value of C_2 = 3.4) was a very noisy image. As C_2 was increased the images became less noisy but had reduced contrast. The same pattern of results was obtained with varying the value of C_1, from 0.4 - 1.0, however the range of convergence was less. Although the value of C_1= 1.0 was theoretically correct, the image quality was not as good (the contrast at the equivalent noise level was lower) (Figure 5.4). The raw data was presented in all the graphs for the purpose of comparison to see how the image quality was improved when applying the different image processing techniques.

The level of noise for the raw data before applying any image processing was 8, which was higher than any solution of images obtained from maximum entropy image processing technique at parameter C_1= 0.4 - 1.0. However at C_1= 0.2 the level of noise for the first two solutions (i.e., at lower value of parameter C_2) were higher than the raw data, although they did have high contrast. It was decided to select the value of parameter C_1 at 0.6 which was the closest value to the theoretically correct value of 1.0 at which the contrast levels were not compromised.

For the maximum entropy image processing technique, it was essential at this stage to choose the best value for parameter C_2. The second set of realisations which consists of images with three different contrast levels in the object area (cn1, cn2 and cn3) was used for this part of the study. Variation of parameter C_2 between 3.7 - 5.0., gave solutions with a range of images differing in image quality. In these images one pass of a conventional smoothing filter gave a noise level of 6.0 . Therefore the aim was to find the value of C_2 which gave this noise level.

For maximum entropy processing a value of C_2 of 4.5 was found to give a noise level of approximately 6.0 for both normal and abnormal images with objects of different contrast (Figure 5.5).

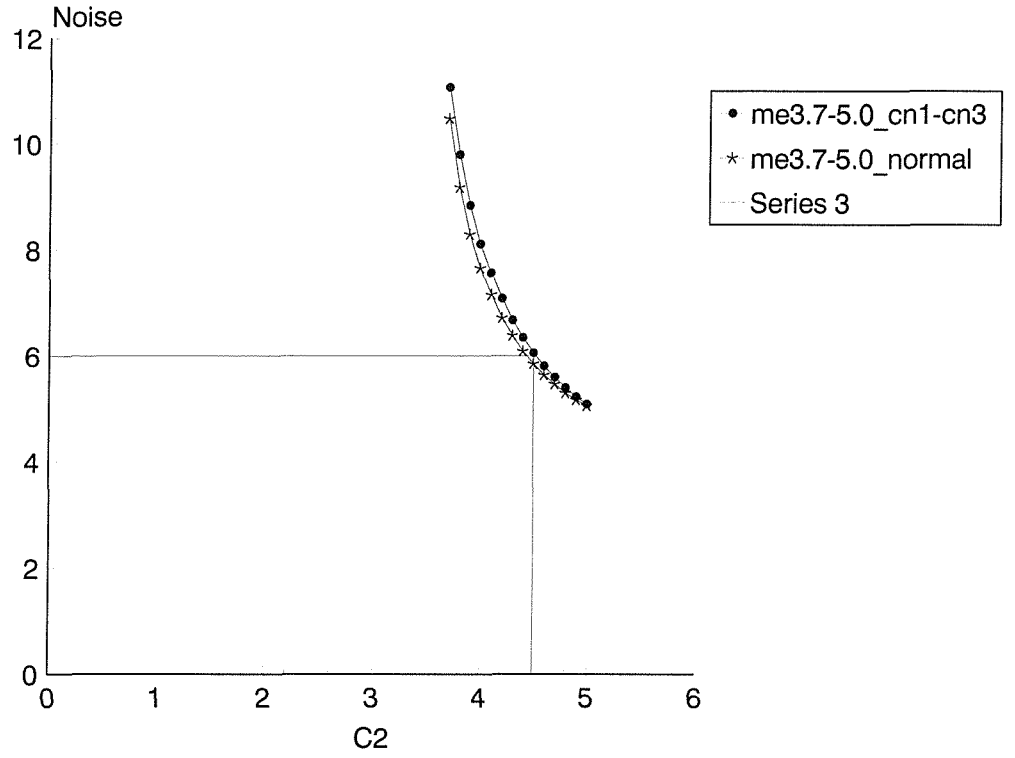

Figure 5.5: Maximum entropy processing at a value of C_2 of 4.5 was chosen at a noise level of approximately 6.0 for both normal and abnormal images with objects of different contrast. The noise values are presented in table 5.2.

5.3.2.3 Wiener Filter

The raw data were also processed by the Wiener filter image processing technique. This gave a variety of results when the point spread function FWHM value was varied between 2 - 12 mm (Figure 5.6). The mean of the level of noise for the raw data images before processing for the first data set was 8.0, while after Wiener filtering processing by varying the point spread function FWHM between 2 - 12 mm, the mean level of noise was varied. The noise was highest for FWHM = 2 mm, and decreased monotonically with increasing FWHM. This was accompanied with an increase in the level of contrast when the FWHM was between 2 - 4 mm. Then followed a rapid drop in the level of contrast when the FWHM was between 5 - 12

mm (Figure 5.7). The value of noise corresponding to one conventional smooth (i.e., 3.0) was used to determine the point spread function FWHM value for Wiener filter image processing technique. Accordingly the value of 6 mm was determined for Wiener filtering (Figure 5.6).

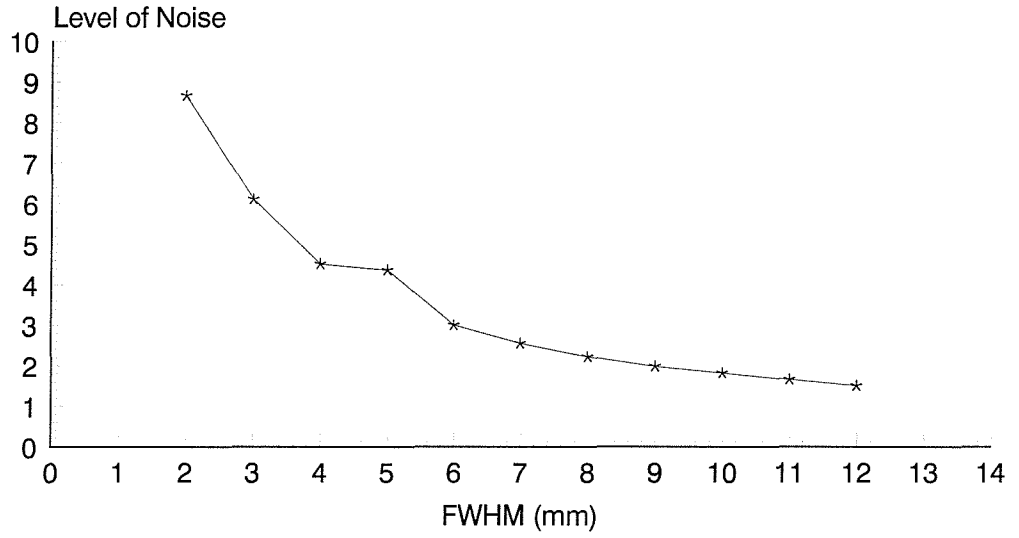

Figure 5.6: Plots of mean noise against mean point spread function FWHM for Wiener filter processed images.

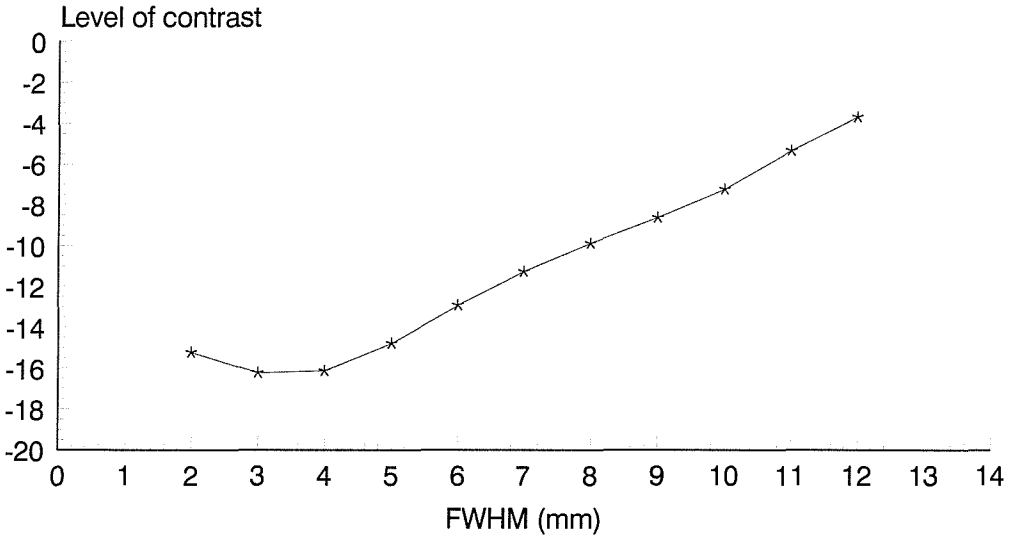

Figure 5.7: Plots of mean contrast against mean point spread function FWHM for Wiener filter processed images.

For the Wiener filter image processing technique, the point spread function FWHM value was obtained according to the above investigation at 6.0 mm. However when applied to the second data set, the level of noise obtained at the value of 6.0 mm FWHM, was slightly higher than the level of noise determined from the other two image processing techniques. Therefore all the images were processed at point spread function FWHM between 5.0 - 6.0 mm, so that an appropriate value could be chosen and a fair comparison obtained. The value for point spread function FWHM at 5.5 mm was chosen (Figure 5.8) as this value gave exactly the same level of noise (i.e., level of noise 6.0) as the maximum entropy and conventional smoothing image processing techniques.

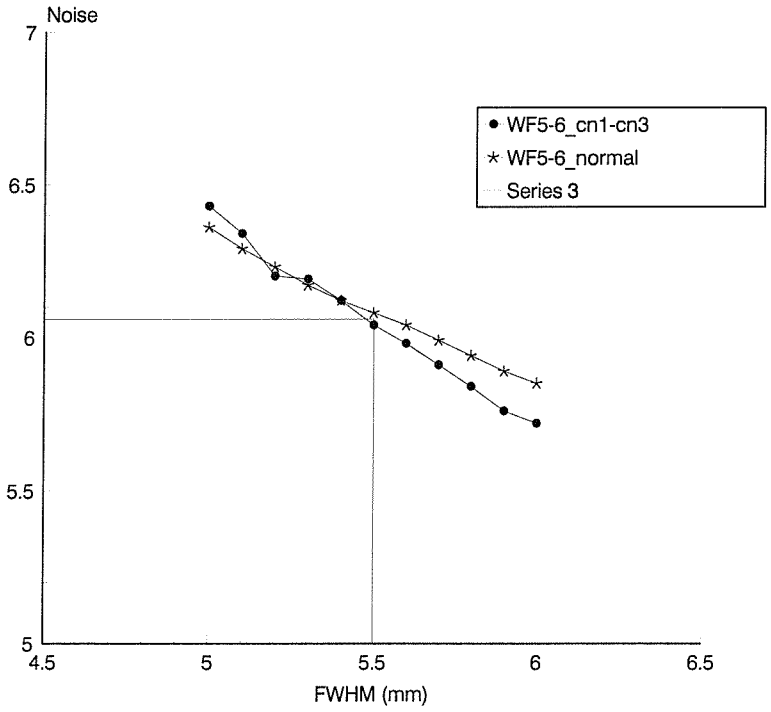

Figure 5.8: Plots of mean noise against mean point spread function FWHM for Wiener filter processed images. The value for point spread function FWHM was chosen at 5.5 mm as this value gave exactly the same level of noise (level of noise 6) as the maximum entropy and conventional smoothing image processing techniques. These values were obtained from the second set of images (section 5.2.1).

5.3.2.4 Results

For the purpose of comparison the mean value of contrast and noise for the normal image, raw data were determined as -5.2 and 11.8 respectively. The contrast was therefore lower than the noise as expected in the absence of a true feature. When processed by any of the processing technique various solutions were obtained in which the level of noise varied, but the level of contrast was small and fairly constant. This was expected since the normal image does not contain any abnormality. Therefore the level of contrast, which is the difference in between the mean count per pixel in the region of interest selected and the mean count per pixel in surrounding region, should be small.

The result obtained from Maximum entropy and Wiener filter image processing techniques, at the level of noise 6 was produced at the value of parameter $C_2 = 4.5$ and at the point spread function FWHM value of 5.5 mm, respectively.

A summary of mean contrast and noise levels can be found in Table 5.2a and b. Also an example of the images obtained by varying the different parameters which are required by the three image processing techniques, are presented in figure 5.9. Examples of the images with varying the level of contrast are presented in figure 5.10.

Mean of the Level of Noise				
Technique	True contrast 1 = 0 count	True contrast 2 = 100 count	True contrast 3 = 200 count	Normal Image
Raw data	11.73	11.76	11.86	11.78
Conventional smoothing at one pass filter	5.99	5.99	6.05	6.14
Maximum entropy at C_1= 0.6 and C_2 = 4.5	6.06	5.95	6.15	5.84
Wiener filter at point spread function FWHM = 5.5 mm	6.07	5.98	6.09	6.08

(a)

Mean of Level of Contrast				
Technique	True contrast 1 = 0 count	True contrast 2 = 100 count	True contrast 3 = 200 count	Normal Image
Raw data	-31.29	-23.61	-16.34	-5.17
Conventional smoothing at one pass filter	-24.33	-18.83	-13.36	-4.83
Maximum entropy at C_1= 0.6 and C_2 = 4.5	-31.66	-24.29	-16.56	-3.31
Wiener filter at point spread function FWHM = 5.5 mm	-28.72	-22.46	-15.1	-4.44

(b)

Table 5.2: Summary of the (a) mean noise and (b) mean contrast, levels using the images with different true contrast, gives results with similar values for the three image processing techniques.

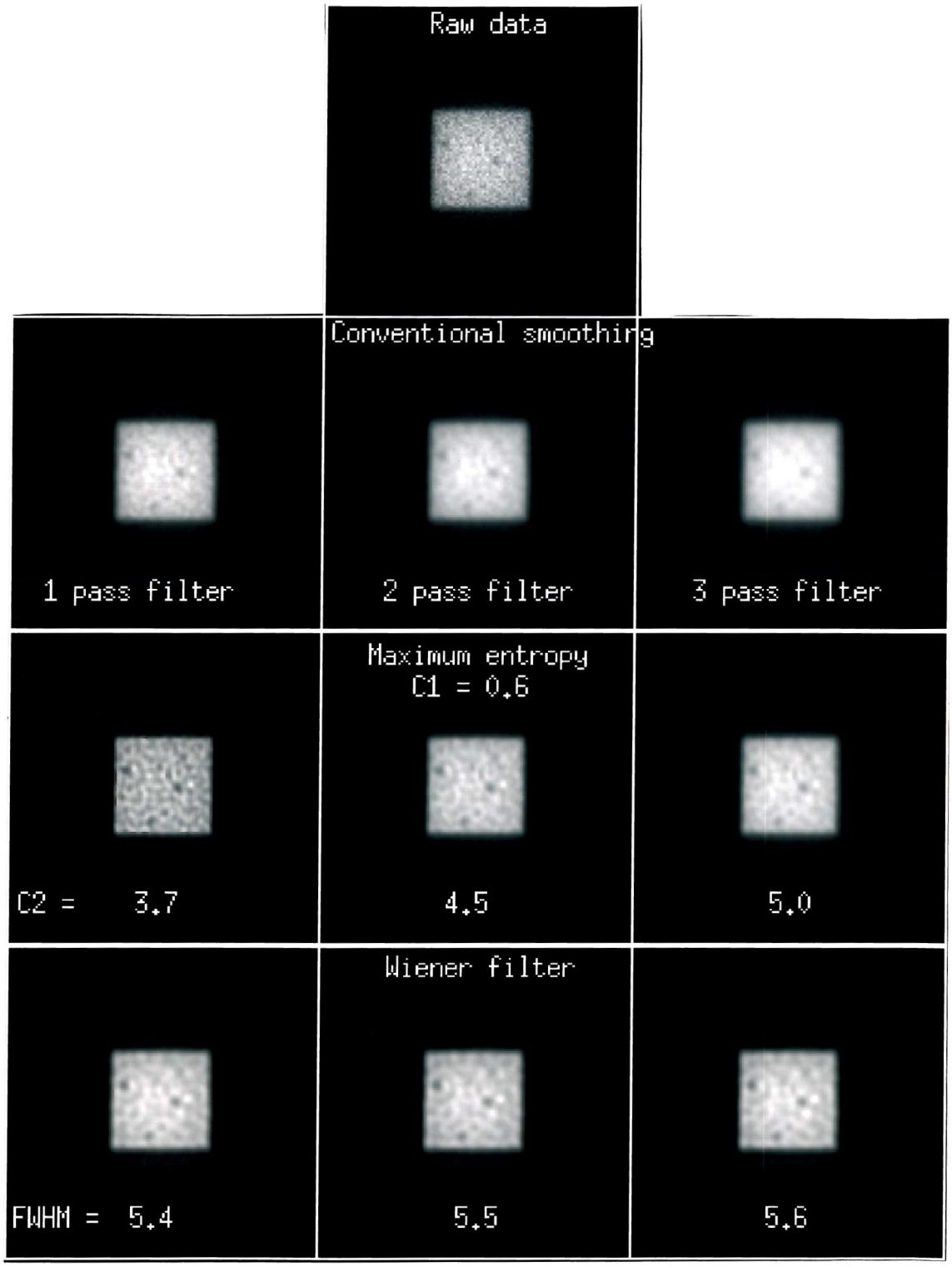

Figure 5.9: The image quality of the different solutions obtained by varying the different parameters for the three image processing techniques.

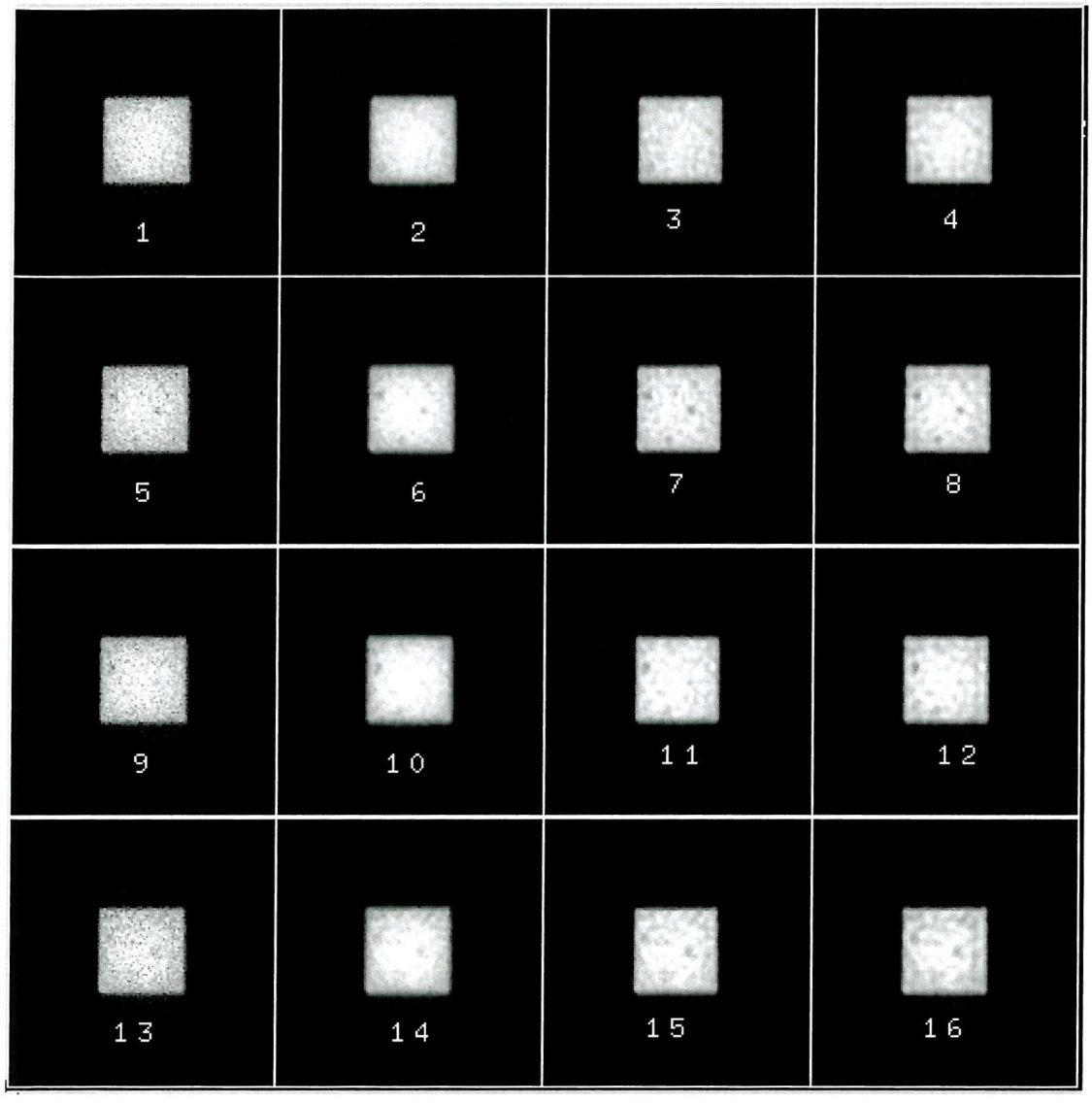

Figure 5.10: Example of normal images and images containing cold objects with varying the level of contrast. Images from 1 - 4 are representing the normal image as follow, (1) raw data , (2) smoothing, (3) maximum entropy and (4) Wiener filtering. Images from 5 - 8, are for the first contrast, from 9 - 12 are for the second contrast and 13 - 16 are for the third contrast. All the three different contrast images are in this order, raw data, smoothing, maximum entropy and Wiener filtering respectively.

5.3.3 Image Evaluation

In order to check the difference in the ability of the three different image processing techniques, in processing the above simulated images, image evaluation has been performed. The Figure of merit (FOM2), (see Chapter 3, section 3.3), has been used as an objective measure of image quality. Also ROC analysis has been used as a subjective assessment for detectability.

From the previous investigation, certain images were selected for this evaluation. These were the 40 images (i.e., Raw data images), containing abnormalities and also the processed versions of these images. The parameters which has been determined previously were used to give images with similar level of noise. The image quality calculations have confirmed that, by exhibiting the similarity in the level of noise for the three image processing techniques (Figure 5.11).

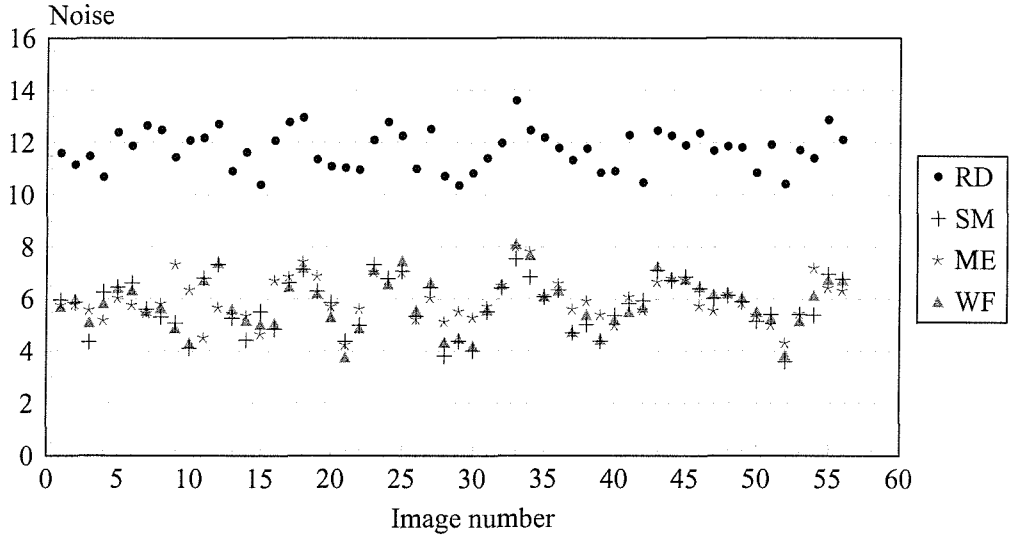

Figure 5.11: The similarity in the level of noise for the three image processing techniques.

To compare this similarity statistically, a paired t-test was used, to show how significant the difference between each group would be (Table 5.3).

Comparison	P-value	95% CI
Maximum entropy vs. Conventional smoothing	0.116	(-0.047, 0.413)
Maximum entropy vs. Wiener filtering	0.332	(-0.104, 0.304)
Conventional smoothing vs. Wiener filtering	0.06	(-0.17, 0.002)
Raw data vs. Maximum entropy	0.000	(-5.96, -5.59)
Raw data vs. Wiener filtering	0.000	(5.69, 6.06)
Raw data vs. Conventional smoothing	0.000	(5.76, 6.15)

Table 5.3: The difference in noise level between each group of images was calculated and compared statistically using a paired t-test .

These results conclude that there were no significant difference in the level of noise in the images chosen for the comparison and this actually makes a fair comparison. The statistical significance in the level of noise for the raw data, was significantly higher than that of the three image processing techniques, where the p-value was 0.000 for all the situations (i.e., Raw data versus Maximum entropy, Raw data versus Wiener filtering and Raw data versus Conventional smoothing). This was expected since the processing techniques were supposed to reduce noise.

The level of contrast for the raw data and the results obtained from the three image processing techniques were different, on account of the ability of the different image processing technique to improve the image quality.

Figure 5.12 shows the way in which the measured contrast varied with the true value. Smoothing naturally lost contrast compared to the raw data and Wiener filtering also had to reduce contrast in making compromise with noise reduction. ME however maintained the original contrast successfully.

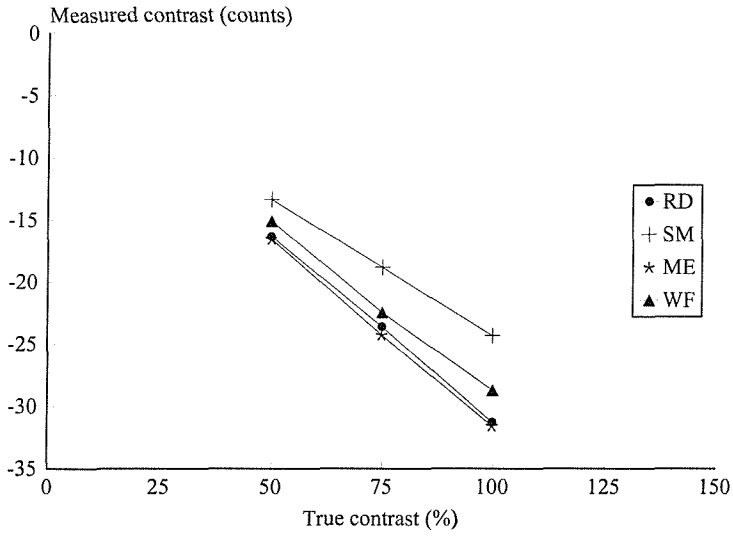

Figure 5.12: The measured contrast compared to the true contrast. It shows the way in which the decrease in detectability of the measured contrast with increasing the true contrast value.

These findings were further demonstrated when the figure of merit was calculated. They showed that there was an improvement in theoretical detectability, when applying all the image processing techniques. The improvement in detectabilty varied from one image processing technique to the other. The p-value for the difference in detectability (i.e., FOM2) between the raw data and the three image processing techniques was highly significant (Table 5.4). By comparing the values for the raw data images to the ones obtained from the three image processing techniques (Table 5.4), each technique shows an improvement in the detectability of the images. The images processed by maximum entropy image processing technique had a higher value of FOM2 than the images processed with Wiener filter and conventional smoothing techniques. The p-value for the difference in object detectability between the images processed with the three different image processing techniques showed significant differences in each case. Both maximum entropy technique versus conventional smoothing technique and Wiener filtering technique

versus conventional smoothing technique had P= 0.000, while for maximum entropy technique versus Wiener filtering technique P= 0.03 (Table 5.5).

Thus based on these FOM2 results the object detectability for each of the processing techniques should be improved relative to the raw data images. They would also predict that ME should be theoretically the best technique. These hypotheses will be tested in analysing the results of the subsequent ROC experiment.

Technique	Mean of FOM2	SD (SE)
Raw data	- 2.92	1.95 (0.261)
Conventional smoothing	- 4.76	3.248 (0.434)
Wiener filtering	- 5.54	3.704 (0.495)
Maximum entropy	- 5.98	3.962 (0.529)

Table 5.4: The mean of FOM2 and its standard deviation, for the improvement in detectability (FOM2) as the raw data processed by the three image processing techniques.

Comparison Techniques	P-value	Paired Differences SD (SE)
Maximum entropy vs. Conventional smoothing	0.000	1.33 (0.178)
Maximum entropy vs. Wiener filtering	0.03	1.48 (0.198)
Conventional smoothing vs. Wiener filtering	0.000	0.997 (0.133)

Table 5.5: The significance of differences in detectability (FOM2), between the performance of the different processing techniques. Note that the difference between the three image processing techniques was highly significant.

5.3.3.1 Receiver Operating Characteristic (ROC) Analysis

The ability of the three different image processing techniques to improve detectability was assessed subjectively by applying Receiver operating characteristic (ROC) analysis. The results obtained from both observers, for the raw data and its processing by conventional smoothing, maximum entropy and Wiener filtering techniques were analyzed by calculating the sensitivity (TPF) and specificity (1 - FPF) of object detection. For both observers the analysis of the data obtained is presented in Figure 5.13a and b, defining the fitted ROC line obtained from the program. Figure 5.13c and d, presenting the corresponding actual data points for both reader, without any data fitting.

The area under the ROC curve, for each reader in each condition (the raw data, conventional smoothing, Wiener filtering and maximum entropy) was calculated and the sensitivity at a false positive fraction of 0.1 was defined. The results of statistical comparison between the three image processing techniques are shown in Table 5.6.

Analysis of these results for the *first reader* using the true positive fraction test at false positive fraction 0.1, indicated that conventional smoothing and Wiener filtering techniques did not perform significantly better ($P > 0.05$) in processing the raw data. In fact they gave a lower value of TPF although it was not statistically significant. By contrast maximum entropy performed significantly better ($P= 0.007$) in processing the raw data.

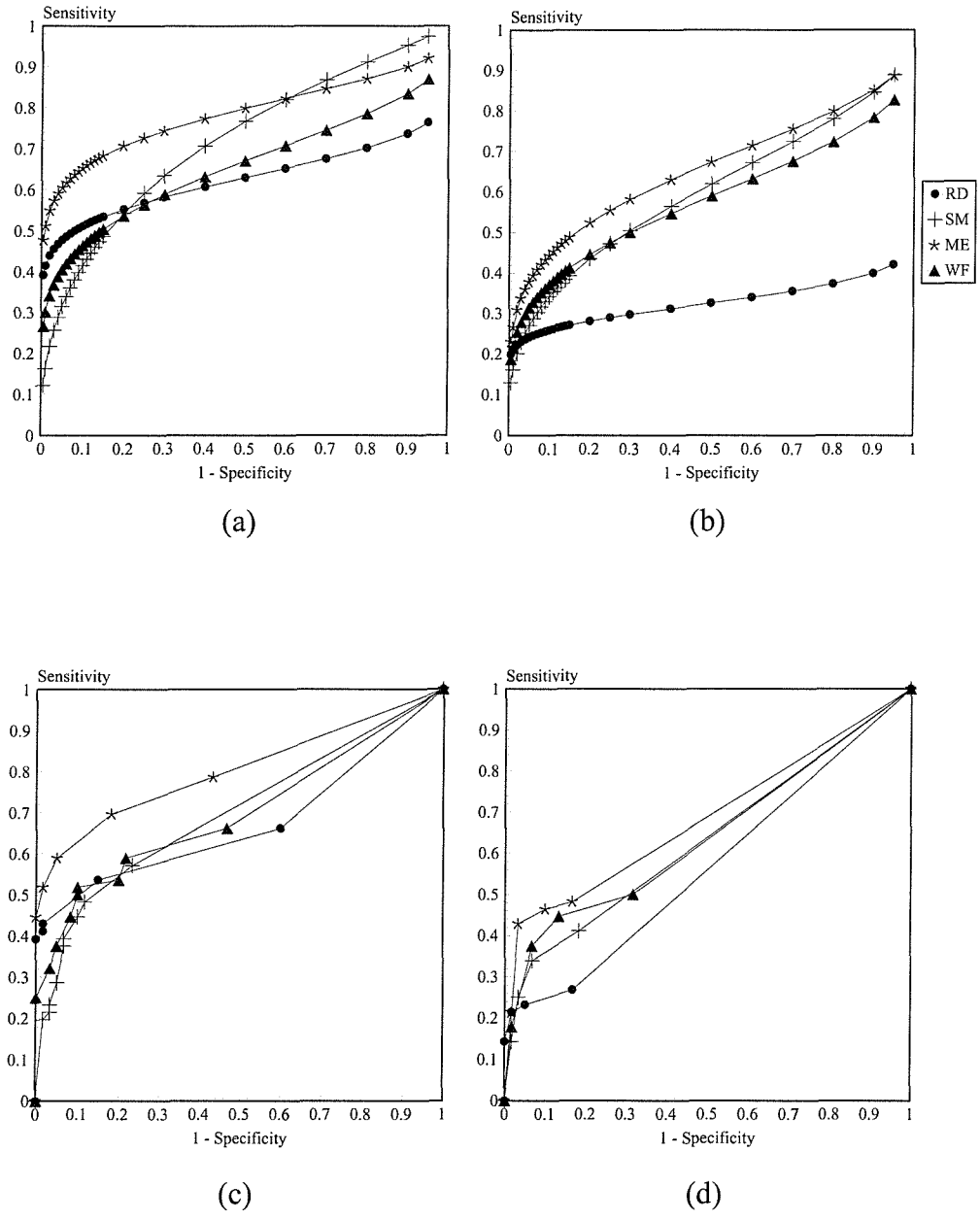

Figure 5.13: The ROC curves after fitting the line from the program, for (a) reader 1 and (b) reader 2, for the raw data and its processing by conventional smoothing, maximum entropy and Wiener filtering techniques. The ROC curves (c) and (d) represent plots of the actual data points for both readers respectively, without any data fitting.

	Reader 1				Reader 2			
	Area test		TPF test		Area test		TPF test	
Imaging technique	AUC (SE)	P-value for AUC	TPF at FPF= 0.1	P-value for TPF test	AUC (SE)	P-value for AUC	TPF at FPF= 0.1	P-value for TPF test
Raw data	0.67 (0.0501)	0.141	0.51	0.145	0.57 (0.0533)	0.009	0.26	0.161
Conventional smoothing	0.71 (0.0485)		0.41		0.63 (0.0516)		0.34	
Raw data	0.67 (0.0501)	0.0016	0.51	0.007	0.57 (0.0533)	0.0023	0.26	0.006
Maximum entropy	0.80 (0.0413)		0.65		0.69 (0.0495)		0.44	
Raw data	0.67 (0.0501)	0.532	0.51	0.347	0.57 (0.0533)	0.0016	0.26	0.044
Wiener filtering	0.68 (0.05)		0.46		0.64 (0.0514)		0.37	
Conventional smoothing	0.71 (0.0485)	0.433	0.41	0.001	0.63 (0.0516)	0.756	0.34	0.176
Maximum entropy	0.80 (0.0413)		0.65		0.69 (0.0495)		0.44	
Conventional smoothing	0.71 (0.0485)	0.437	0.41	0.49	0.63 (0.0516)	0.853	0.34	0.634
Wiener filtering	0.68 (0.05)		0.46		0.64 (0.0514)		0.37	
Maximum entropy	0.80 (0.0413)	0.015	0.65	0.0007	0.69 (0.0495)	0.593	0.44	0.363
Wiener filtering	0.68 (0.05)		0.46		0.64 (0.0514)		0.37	

Table 5.6: Estimates of the binormal ROC parameters and the inter-condition coefficients for the area under the estimated ROC. For both true positive fraction (TPF) test at false positive fraction (FPF) = 0.1 and area test, for both readers.

The analysis for the inter-comparison between conventional smoothing versus Wiener filtering technique was not significant (P= 0.49), although, the comparison between maximum entropy versus Wiener filtering techniques and maximum entropy versus conventional smoothing techniques were highly significant ($P < 0.05$). Similar results were obtained when the area under ROC curve (i.e., AUC) were used for obtaining the significance between each comparison.

A separate analysis of the results obtained from the second reader for the comparison showed that there is a significant difference in processing the raw data images with maximum entropy and Wiener filtering ($P < 0.05$). However, when the comparison was carried out between the three image processing techniques, it showed that none of the techniques is significantly better ($P > 0.05$) than the others. The sensitivity of all three processing techniques was better than the raw data (TPF = 0.26) being highest for maximum entropy (TPF = 0.44.).

The results of the raw data and each individual image processing technique obtained from each reader were compared and tested for any significant difference between their interpretation, and shown in table 5.7 and figure 5.14a,b,c and d. By using the true positive fraction test at false positive fraction 0.1, it shows that there is no significant difference ($P > 0.05$) in both readers interpretation of the images which processed by conventional smoothing and Wiener filtering techniques. However for interpreting the raw data and maximum entropy images there was a significant difference in the results of both readers. Reader 1 obtained higher ROC curve than reader 2 for all techniques.

Imaging technique	Area test			TPF test		
	AUC (SE)	P-value for AUC	Average of AUC for both observers	TPF at FPF =0.1	P-value for TPF test	Average of AUC for both observers
Reader 1	0.67(0.0501)			0.51		
Raw data		0.002	0.62		0.003	0.38
Reader 2	0.57(0.0533)			0.26		
Reader 1	0.71(0.0485)			0.41		
Conventional		0.324	0.67		0.423	0.37
smoothing	0.63(0.0516)			0.34		
Reader 2						
Reader 1	0.80(0.0413)			0.65		
Maximum entropy		0.184	0.75		0.019	0.54
Reader 2	0.69(0.0495)			0.44		
Reader 1	0.68(0.05)			0.46		
Wiener filter		0.415	0.66		0.266	0.41
Reader 2	0.64(0.0514)			0.37		

Table 5.7: The result of both readers for the raw data and the three image processing techniques using the area under curve and false positive fraction tests. Both readers result were averaged for testing any significant trends.

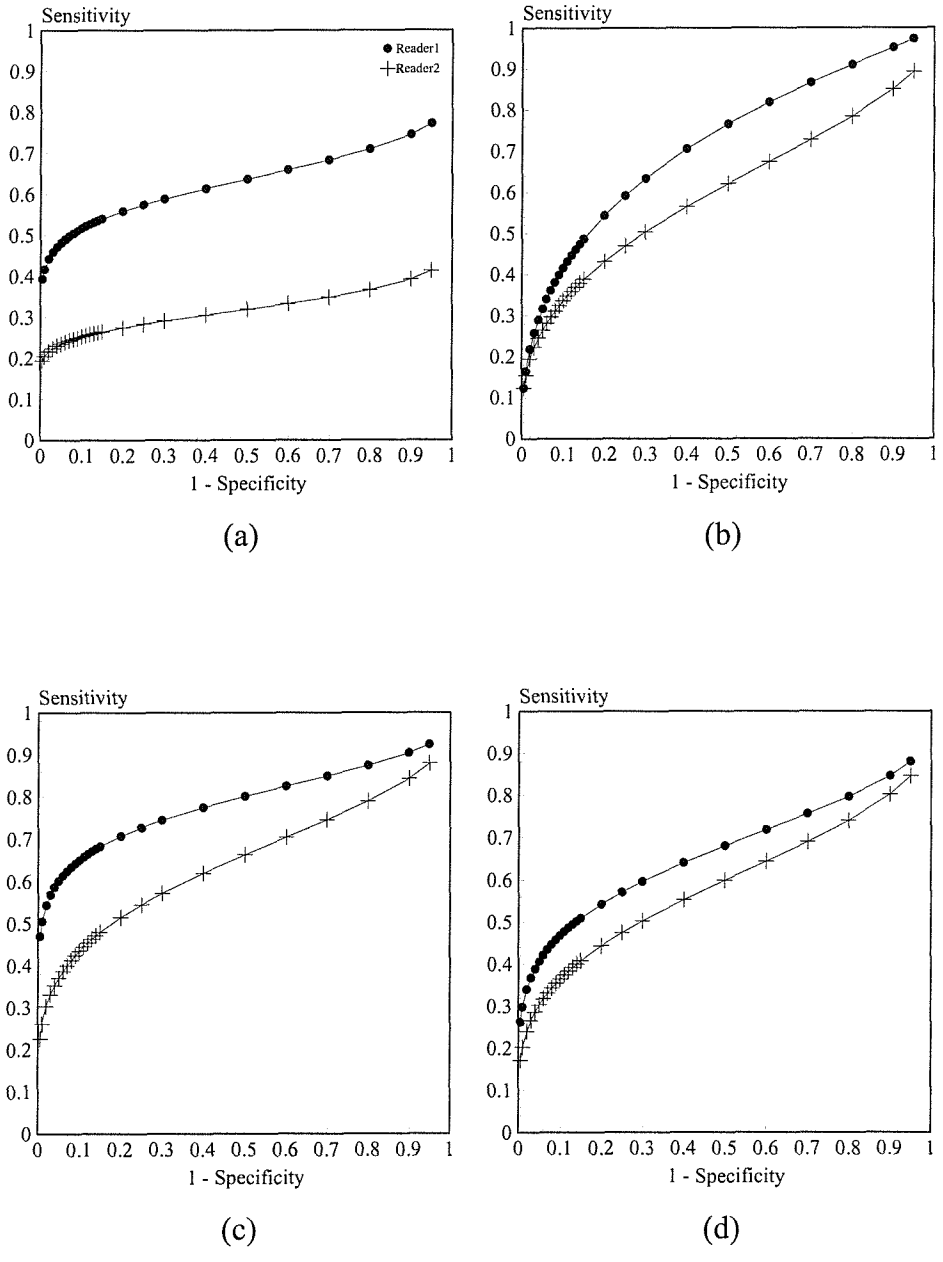

Figure 5.14: The sensitivity and (1- specificity) for both readers when interpreting the images of the (a) raw data (b) conventional smoothing (c) maximum entropy and (d) Wiener filtering techniques.

It is important to recognize that different response patterns were found from the ROC analysis of both readers. The ways in which observers use the rating scale may depend on the training they receive in use of the scales, on the nature, subtlety, and prevalence of abnormality in the experiment, and on the consequence of positive and negative findings in the corresponding display. There was a correlation in the result obtained from both tests (i.e., AUC test and TPF test) applied to the data, which was interpreted by both observers (Figure 5.15).

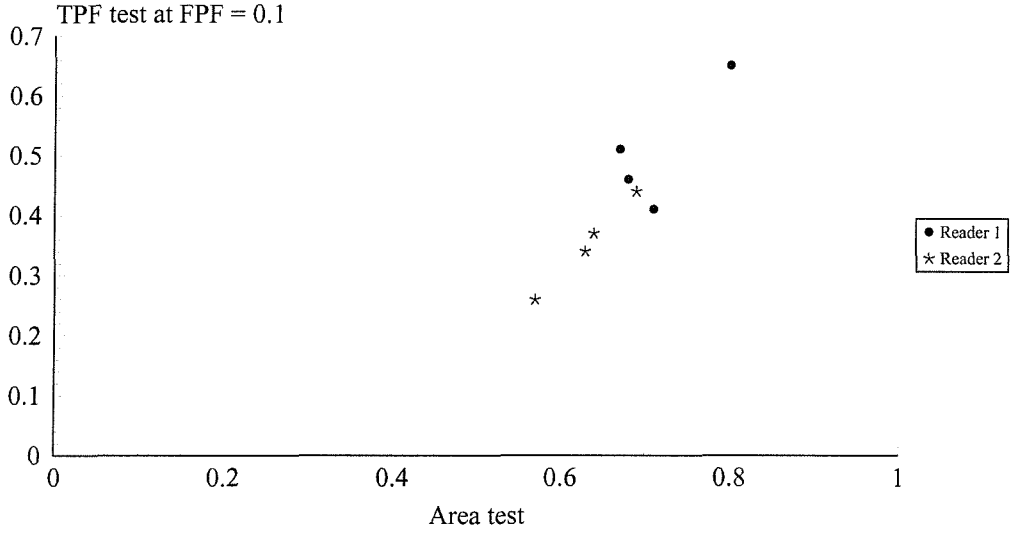

Figure 5.15: The correlation between area under curve (AUC) test and true positive fraction (TPF) test, for both readers.

5.3.3.2 The Correlation Between FOM2 and ROC Analysis

The decision made from each reader regarding the detectability or the perception of each image was correlated to the figure of merit which was obtained by calculating the image quality for each image. The Spearman correlation coefficient was used to evaluate the correlation between both evaluation techniques. The correlation of both

evaluation techniques for both readers are given in figure 5.16a,b,c and d, figure 5.17a,b,c and d and table 5.8.

For the *first reader* for the raw data and for each individual image processing techniques, it has been found that there was a significant correlation, **r** ($P < 0.001$) between the FOM2 and detectability. Thus the probability of such a correlation, or one more extreme, arising by chance when there was in fact no relation is approximately 0 in 1000.

From the results obtained from the *second reader* for the raw data and each individual image processing techniques, there were also a significant correlations, **r** ($P \leq 0.001$) between the FOM2 and detectability. However for each technique the correlation coefficient was lower for this reader.

Although there was a linear correlation between FOM2 and detectability, the correlation coefficients were not very high and some individual results obtained, particularly with the maximum entropy and Wiener filtering techniques seems to be anomalous with respect to the general trend (Figure 5.16c, 5.16d, Figure 5.17c and Figure 5.17d). These were examples either having high detectability with very low FOM2, or low detectability and high FOM2. In extreme cases, objects with high FOM2 had zero detectability. Table 5.9 shows the results for several individual objects for one of the readers using maximum entropy processing including two of the anomalous examples. In fact these anomalous results were generally for images with very small size (0.5 cm) and very low contrast objects. However one of the images with bigger object size (1.0 cm) gave a similar anomalous result. In retrospect this was probably due to interpreter error, for example reading the wrong image.

The mean of the FOM2 and detectability for the raw data and the images processed with the three image processing techniques, for both readers are shown in figure 5.18. For both readers there was a correlation between FOM2 and detectability. The correlation was particularly good for reader 2. The raw data result for the first reader was inconsistent compared to the trend of other results.

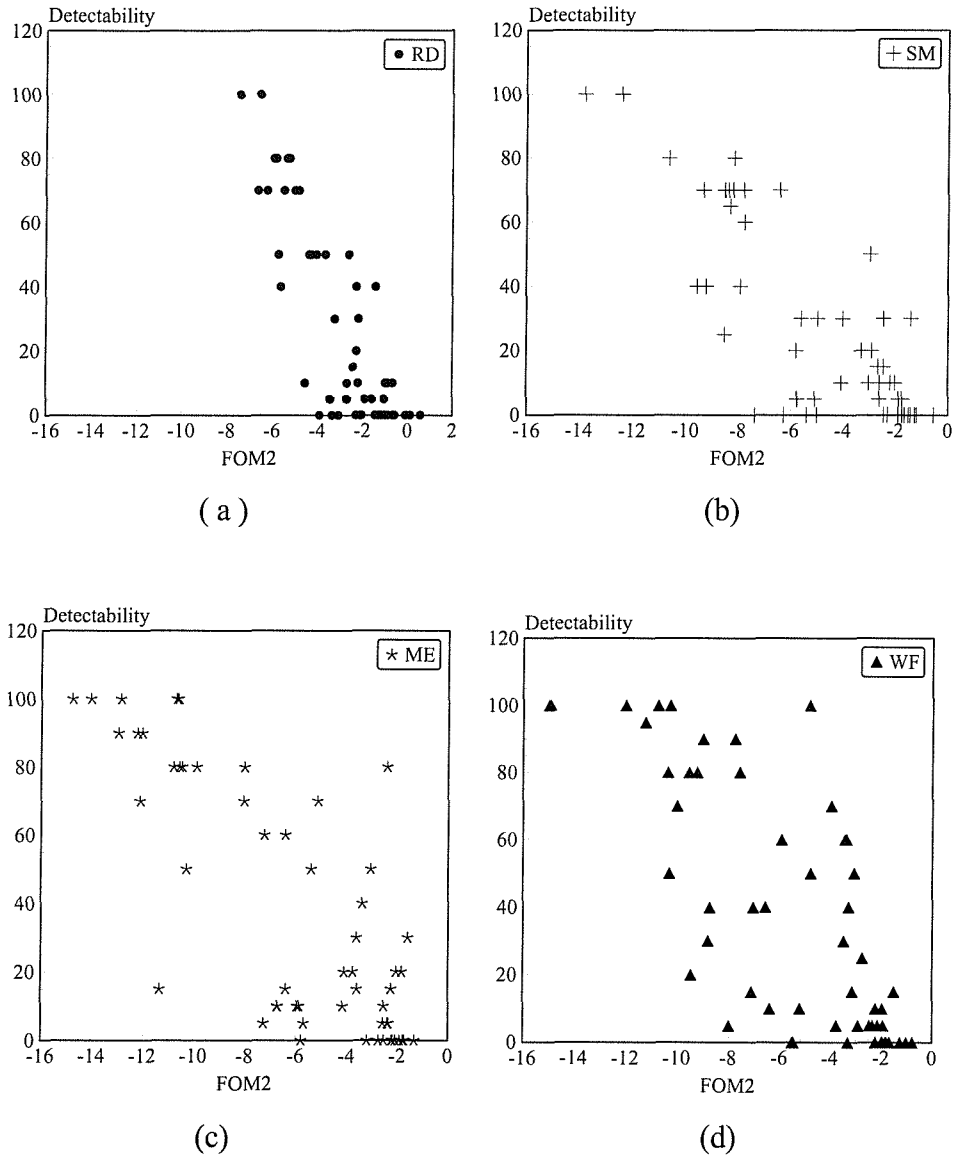

Figure 5.16: The relationship between FOM2 and detectability for the first reader, for (a) raw data (b) conventional smoothing (c) maximum entropy and (d) Wiener filtering, the correlation coefficients were not very high and some individual results obtained, particularly with the maximum entropy and Wiener filtering techniques seems to be anomalous with respect to the general trend. See table 5.8., for the correlation coefficients and P-values.

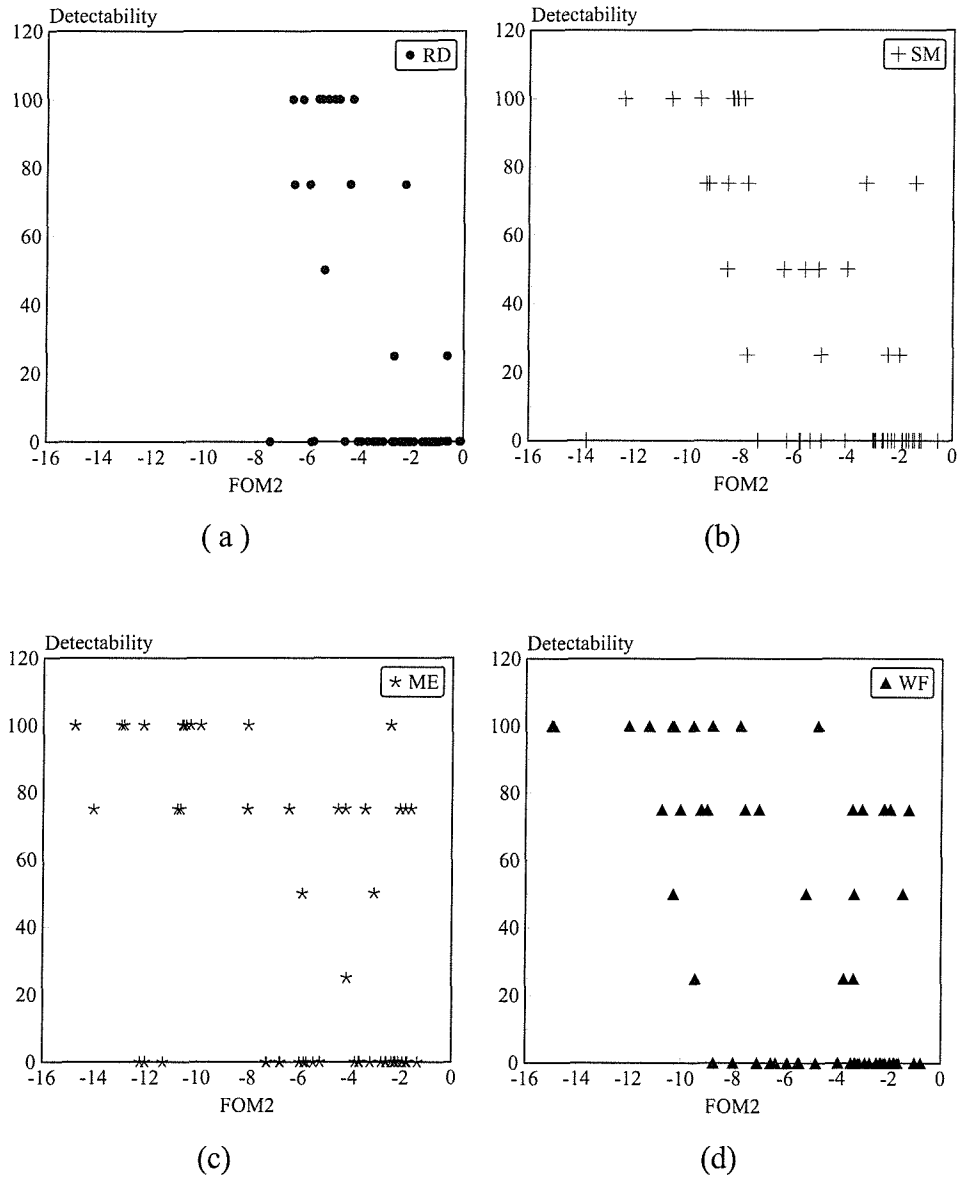

Figure 5.17: The relationship between FOM2 and detectability for the second reader, for the (a) raw data (b) conventional smoothing (c) maximum entropy and (d) Wiener filtering techniques. The correlation coefficients were not very high and some individual results obtained, particularly with the maximum entropy and Wiener filtering techniques seem to be anomalous with respect to the general trend.

Technique	Reader 1		Reader 2	
	r	P-value	r	P-value
Raw data	0.8	0.000	0.56	0.000
Conventional smoothing	0.75	0.000	0.65	0.000
Wiener filtering	0.76	0.000	0.57	0.000
Maximum entropy	0.65	0.000	0.43	0.001

Table 5.8: The Spearman correlation coefficients, between FOM2 and ROC detectability for both readers.

Image number	Detectability	FOM2	Size of object (cm)	Contrast % of object
1	100	-14.76	1	100
2*	15	-11.31	1	75
3	60	-7.22	1	75
4	10	-6.72	0.5	75
5	0	-5.77	1	50
6*	80	-2.39	0.5	75
7	0	-1.32	0.5	50

Table 5.9: Some particular and anomalous (*) cases (images) of maximum entropy results, for one of the readers.

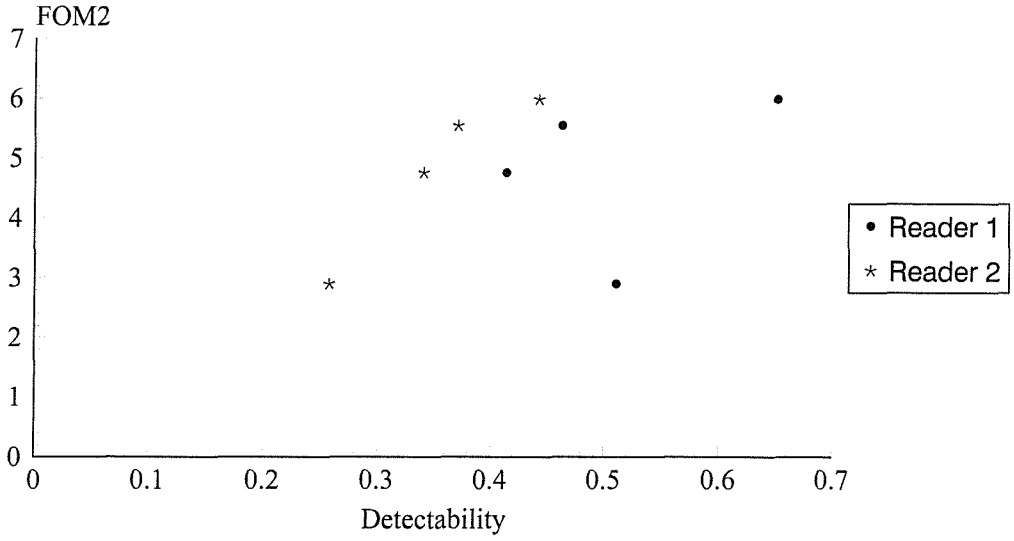

Figure 5.18: The mean of FOM2 against the mean of detectability of the raw data and the three techniques for both readers.

5.4 Discussion

The task of comparing processing techniques in medical imaging is not straightforward. Clinical images can be used for evaluation but it is difficult to be certain of the true diagnosis in these real images. In this study simulated images have been used to substitute the real clinical images, due to the benefits that arise from the simulation of images. The main advantage is that the true image distribution is known and can be used as a gold standard against which to compare the performance of other techniques. Simulation also allows a variety of distributions and features in the image to be created and investigated. It therefore allows us to study systematically, the effects of various factors in the image, on the detection, localization, and determination of shape and size of any added artifact. However the disadvantage of the simulated images is a lack of reality. No simulation techniques can currently model all aspects of gamma camera acquisition.

The three image processing techniques produced a variety of images different in image quality. Each technique required certain parameters to carry out the processing. In comparing the techniques it was important to choose these parameters in a controlled way so that the comparison could be meaningful. The type of object that was used to create the simulated images allowed for the level of noise in the image to be calculated. That enabled the selection of the parameters required by the different image processing techniques to be defined and limited. The standard deviation (i.e., level of noise) also allowed producing equivalent images from each method. The contrast to noise graphs were valuable to enable selection of parameters approximately maximizing the contrast to noise ratio. All processing techniques used in this study have the disadvantage of having to choose parameters which determine the level of smoothing applied to the images. In principle maximum entropy used with $C_1 = 1$ and $C_2 = 0$ should give a theoretically optimal solution. However the technique does not converge with these error values and other values have to be chosen to make the technique operate. C_1 has been optimized for the particular images used in this study but the general use of $C_1 = 0.6$ would have to be validated for other types of image distribution. From our previous studies we know C_2 will be

quite count dependent. Thus in its present form ME is not able to define on overall optimal solution, only an optimal solution given a specific level of smoothing.

The Wiener filter process also has two parameters that can be varied, the FWHM of the point spread function and the noise parameter. The version of the filter used in this study only allowed one of these parameters to be varied, the FWHM. This did allow a full range of solutions to be created, from high contrast high noise to low contrast low noise so that a reasonable comparison could be made with other techniques. However not having the ability to control the noise parameter was a limitation of this study.

Having determined the values of the parameters for each image processing technique the image evaluation could be carried out objectively (FOM2) and subjectively (ROC analysis), in a consistent manner.

All processing techniques had a better FOM2 than raw data, primarily as a result of reducing noise by a factor of about two. Both image processing techniques involving image sharpening (i.e., maximum entropy and Wiener filtering) were better than conventional smoothing. Conventional smoothing inevitably had to lose contrast resolution while improving noise, whereas the deconvolution techniques were able to more or less maintain contrast with the same improvement in noise. The maximum entropy image processing technique produced higher FOM2 than Wiener filter image processing technique, indicating that the theoretically more rigorous approach in image optimization is in fact producing improved images using objective image evaluation with conventional parameters of image quality.

ROC analysis has been used to test the ability of the three image processing techniques to improve subject image detectability. Both readers ranked the image processing techniques in this order: maximum entropy, Wiener filter and conventional smoothing. The result obtained from the first reader shows that conventional smoothing and the Wiener filtering technique did not perform significantly better in processing the raw data ($P > 0.05$). In contrast the maximum entropy results were significantly better from those of the raw data, conventional

smoothing and Wiener filtering ($P < 0.05$). This was true whether the sensitivity of maximum entropy results at a low FPF value (0.1) or at the area under ROC curve in general, were used to show an improvement in image quality. This was not the case with the second reader who found all three image processing techniques to be significantly better than the raw data ($P < 0.05$), but none of the techniques was significantly better than the other ($P > 0.05$). The sensitivity of maximum entropy technique was the highest (TPF = 0.44) at FPF = 0.1 .

There were clear difference between the diagnostic accuracies achieved by the two readers. This can be explained primarily by the individual methods of interpretation. Reader 1 developed a strategy of detection based on creation of a learning set of images with percentage confidence of detectability scores ranging evenly between 0% and 100 % . Each image was then compared to this baseline data set using careful adjustment of the upper contrast level to determine the value at which objects disappeared. Considerable care was taken over each evaluation. Reader 2 reported the images much more quickly and essentially recorded his initial impression of objects which were clearly seen in the image. He used the discrete five point scale in reporting. The pattern of results was also different between the readers. For reader 2 all the image processing techniques performed better than the raw data whereas reader 1 produced better results with raw data than with either smoothing or Wiener filtering. For this reader interpretation of raw data gave better results than expected from the FOM2 predictions. This is almost certainly because some observers carry out a smoothing by eye giving higher confidence to pixels which stand out from the surrounding if there are other nearby pixels of similar value. This suggests that image processing techniques are likely to be more valuable to some observers than others.

The results obtained from both readers showed a significant correlation between the figure of merit and detectability using ROC analysis for each individual image processing technique. However there was a range of correlation coefficients and in general the correlation was not precise. For a given figure of merit there was a considerable variation in the percentage score of the confidence of detectability. Even when taking care with the assessment of the FOM2 value there is variation due

to the noise in the image (Chapter 4). However this does not account for most of the variability seen in relationship between FOM2 and visual detectability and this is explained by the subjective and variable nature of the percentage confidence visual score.

The use of ROC analysis is dependent on the performance of human observer. Therefore it has certain limitations. One problem is the complexity and hence the cost of the study. More than one observer has to be used, each observer has to read many images and conditions for the study have to be carefully controlled. The time each observer needs to spend in reading the images can be very long. However it is a more reliable measure for the performance of many modalities.

5.5 Conclusion

The study has shown that image processing technique are effective in terms of objective improvement. However the argument was less clear for subjective image interpretation. For simple planar objects in which the model describing the image formation process was precise maximum entropy image processing technique, theoretically an optimal technique, produced superior images. FOM2 correlates to detectability, but does not appear to be a reliable alternative to ROC analysis.

Chapter Six

Investigations on the use of Maximum Entropy, Wiener Filter and Conventional smoothing Techniques in Processing Simulated Lung Ventilation Perfusion Images

6.1 Introduction

Pulmonary Embolism (PE) is an important cause of death . In the United Kingdom about 20,000 patients per year die from PE and it contributes up to 15-29% of all deaths in an acute general hospital (Gray 1993). PE is the presence of a blood clot or other foreign substance in pulmonary arterial blood vessels, which leads to obstruction of circulation to lung tissue. Most pulmonary emboli originate from thrombi in the proximal deep veins of the lower limbs. When this happens partial obstruction of arterial blood flow of the lung occurs, resulting in dysfunction of the affected lung tissue. There are many diagnostic procedures that can be used to detect PE such as, Chest radiography (Chest X-ray), Pulmonary Angiography, Spiral Computed Tomography Angiography (SCTA), Magnetic Resonance Imaging (MRI) and Ventilation and Perfusion Scintigraphy (V/Q scan). Chest radiographs are essential in the imaging evaluation of a patient clinically suspected of having pulmonary embolism (PE), although it is not an accurate means of diagnosis. The chest radiograph can help in establishing or excluding some of the possible clinical diagnosis to differentiate

between PE and others, such as cardiac failure, chest infection or pulmonary hypertension, which may account for the patient's symptoms. Pulmonary angiography is suggested for patients with high risk of PE. It has a high sensitivity of detection of PE and is considered the gold standard for the diagnosis of PE. However it is an invasive procedure involving the placement of a catheter into the right side of the heart with an injection of contrast medium into the pulmonary arteries. A pulmonary angiogram is considered when some other imaging scan (i.e., such as V/Q scan images) would not be able to define the risk group of PE to which the patient can be classified. However it is contraindicated in patients who are allergic to the contrast medium used for the study. According to the PIOPED (prospective investigation of pulmonary embolism diagnosis) study, pulmonary angiography is a relatively safe but not trivial procedure (Gottschalk et al 1993a and b). There is thus a need for an investigation which has a high diagnostic accuracy and specificity, but which is relatively non-invasive and can readily be used for screening. One such procedure is provided by ventilation/perfusion lung scintigraphy which is described more fully below. Another diagnostic procedure which is non-invasive and used as a mean of investigating patients with PE, is Spiral CT angiography (SCTA). This does not require catheterisation of central vessels. It images the lungs, mediastinum and pleural spaces and also it is able to reveal non-embolic pathology presenting with symptoms identical to PE which are likely to produce non-diagnostic V/Q scans. The sensitivity of SCTA for detection of PE is over 80%, while the sensitivity of V/Q scans is 45% (Kemp et al 1997).

Ventilation scintigraphy is used to assess disorders of transport of gas down the bronchial tree. To study ventilation scintigraphy, either gases (^{133}Xe, ^{81m}Kr) or ^{99m}Tc-DTPA (Diethylenetriaminepentaacetic acid) aerosols are commonly used. Perfusion scintigraphy is a useful diagnostic procedure to study disorders of blood distribution. It gives a non-invasive method for demonstrating pulmonary perfusion. The procedure is carried out by giving the patient an intravenous injection of ^{99m}Tc-labelled human albumin microspheres (HAM) or macroaggregates (MAA). These albumin particles, occlude small branches of the pulmonary artery and the capillaries, so the resulting images will show the areas of the lung which are perfused. Perfusion scintigraphy alone cannot distinguish between embolus, infarct, or any other cause of impaired pulmonary perfusion due to its ability to study only disorders of blood distribution. A combined

ventilation / perfusion (V/Q) lung scintigram can, however, reliably do so for any mismatched abnormalities.

There are many limitations of the quality of radionuclide imaging, with particularly the resolution of the gamma camera being worse than other medical imaging systems. As has been mentioned in chapter one, the spatial resolution is affected by the collimator resolution and the intrinsic resolution and is of the order of 1.0 cm. Nuclear medicine images are also degraded by the presence of noise, which reduces the certainty of the image density at a particular location. In lung scintigraphy the image produced is a two dimensional representation of the three dimensional distribution of radioactivity introduced to the lung and this reduces the contrast of abnormal features.

If the influence of image processing on diagnostic accuracy is to be investigated, there needs to be confidence in the true diagnosis. This is difficult to ascertain with clinical data and so in this investigation computer simulated images were used instead. Computer simulation has proven its practicality and usefulness in the assessment of image interpretation both qualitatively and quantitatively (Fleming and Simpson 1994). In this investigation the maximum entropy image processing technique has been used to process simulated lung V/Q images and compared to the use of other image processing techniques.

6.2 Methods

6.2.1 Image Simulation

The simulation program (Fleming 1996) required definition of a distribution of activity in the lungs and a map of the attenuation coefficients of the surrounding tissues. These were defined using high-resolution anatomical data from nine magnetic resonance images on male subjects. These had been segmented into soft tissue, lung and bone using a semi automatic method (Fleming 1996). The program used these distributions as an input to create simulated planar gamma camera images of the lung from any required

angle. Normal images used uniform distribution of activity in the airways (Fleming et al 1997). The process is summarised in figure 6.1.

The simulations were considered by expert observers to be realistic in appearance. The use of several different lung models allowed inter-subject variability amongst normals to be included in the study. Abnormalities were introduced using a model of the lung segments which was described relative to one of the subjects in the study.

'Original in colour'

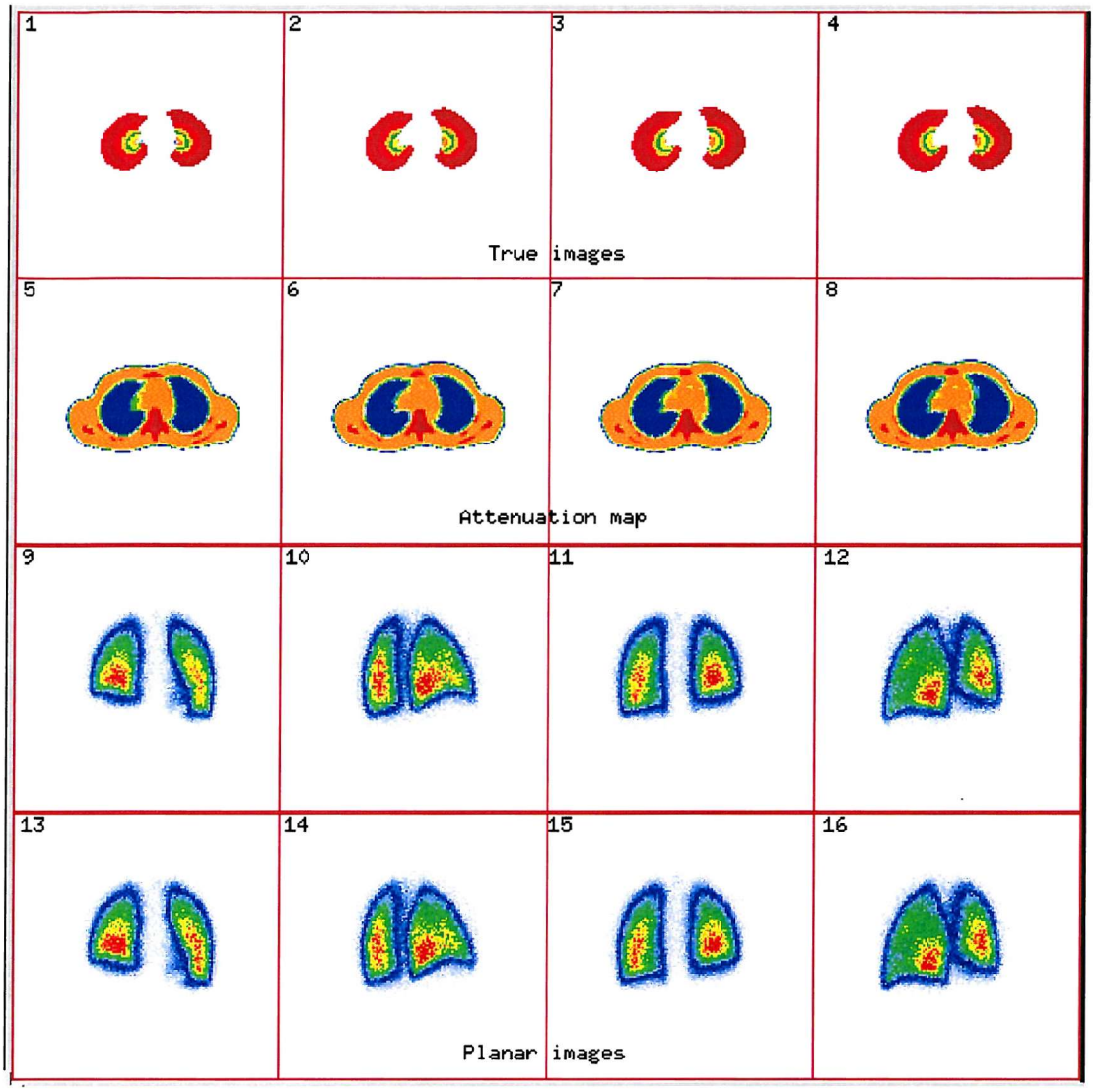

Figure 6.1: Example of input data to the simulation program algorithm, that is, (1 - 4) the activity distribution in the lung and (5 - 8) the attenuation map. Images (9 - 12) and (13 - 16) shows the anterior, right posterior oblique, posterior and left posterior oblique planar ventilation and perfusion images respectively, derived from the simulation. The first and second rows consist of a series of four transverse slices from the three-dimensional data sets. For each set, the leftmost image is near the top of the lung and subsequent images are obtained by moving down the lung. Each slice is oriented with the anterior aspect of the subject at the top of the image and with the left side on the right. The activity distribution assumes uniform concentration per unit airway volume in each generation.

6.2.2 Segmental Model

The segmental model used in this study was obtained using photographs of casts of the lung airways (anterior, posterior, left posterior oblique, right posterior oblique, left lateral and right lateral) (Netter 1989). Measurements of dimensions of the different segments were obtained from the photographs and applied to a three dimensional outline of the lungs obtained from the MR images of one of the subjects in this study (Al-Abdul Salam 1998). Each segment has given a different number as in table 6.1:

Segment number	Left Lung	Segment number	Right Lung
10	Apical	11	Apical
2	Anterior	12	Anterior
3	Posterior	13	Posterior
4	Apical superior	14	Apical superior
5	Lingular superior	15	Lateral
6	Lingular inferior	16	Medial
7	Anterior medial basal	17	Anterior basal
8	Lateral basal	18	Medial basal
9	Posterior basal	19	Lateral basal
		20	Posterior basal

Table 6.1: Value of segments for the segmental model.

An illustration of the outlines of some of the segments is shown in figure 6.2 .

'Original in colour'

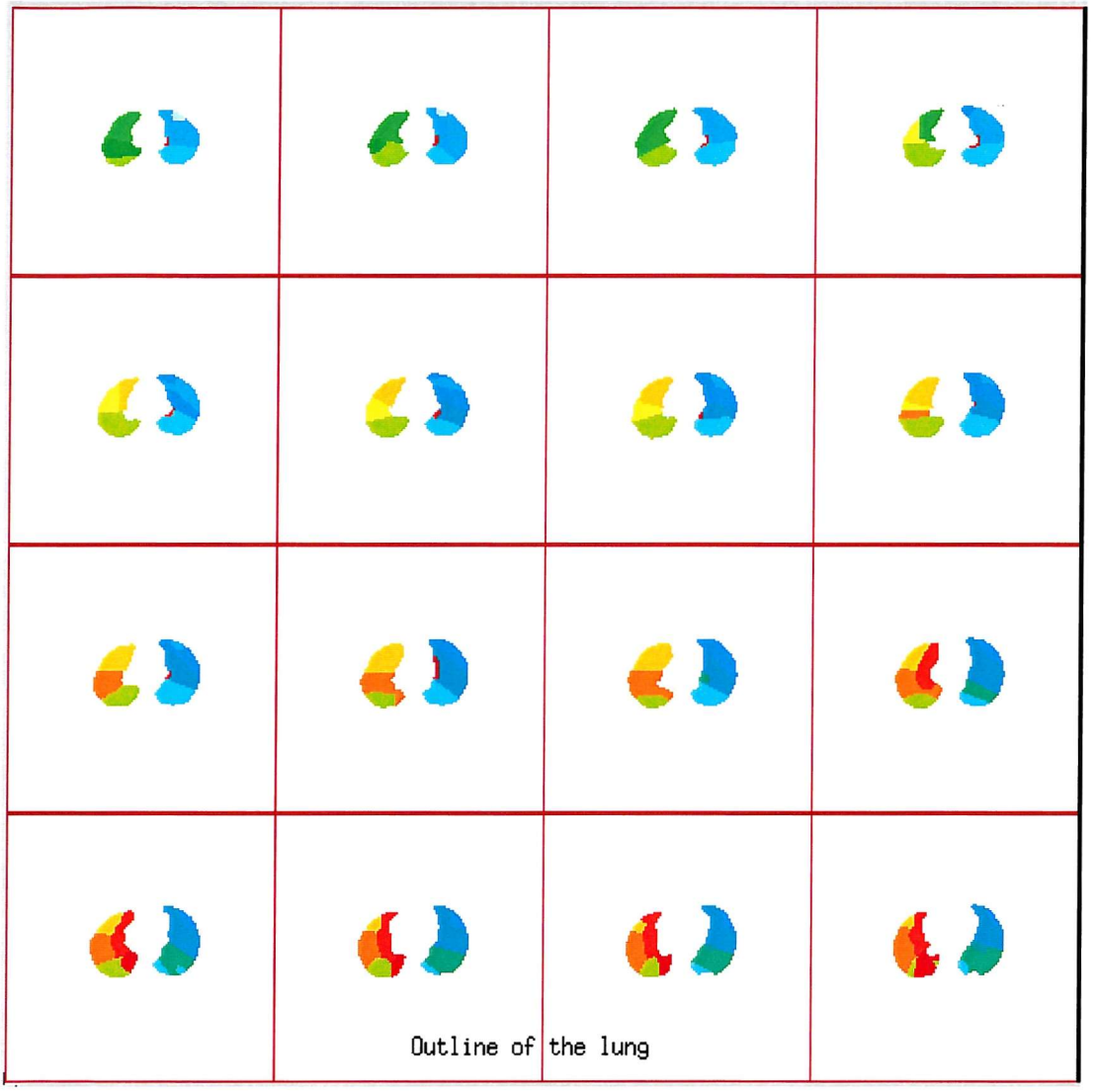

Figure 6.2: Transverse slices through the lung starting towards the apex of the lung top left and moving left to right then top to bottom towards the base of the lung. Each segment is shown in a different colour.

'Original in colour'

6.2.3 Creating Segmental Defects

The creation of segmental defects for a particular subject required definition of the outline of the segment for that individual. This was done by carrying out an elastic transform of the segmental model to the lung shape. This based on a radial stretching of the model around the hilum of the lung when the main bronchus enters the lung (Fleming et al 1996). This point had been defined on the MR data sets of all subjects. The defect was created by setting the activity in the segment to zero.

Normal images were produced assuming a uniform distribution in the lung airways (Fleming et al 1997). Example slices through typical normal and abnormal activity distributions in the lung are shown in figure 6.3.

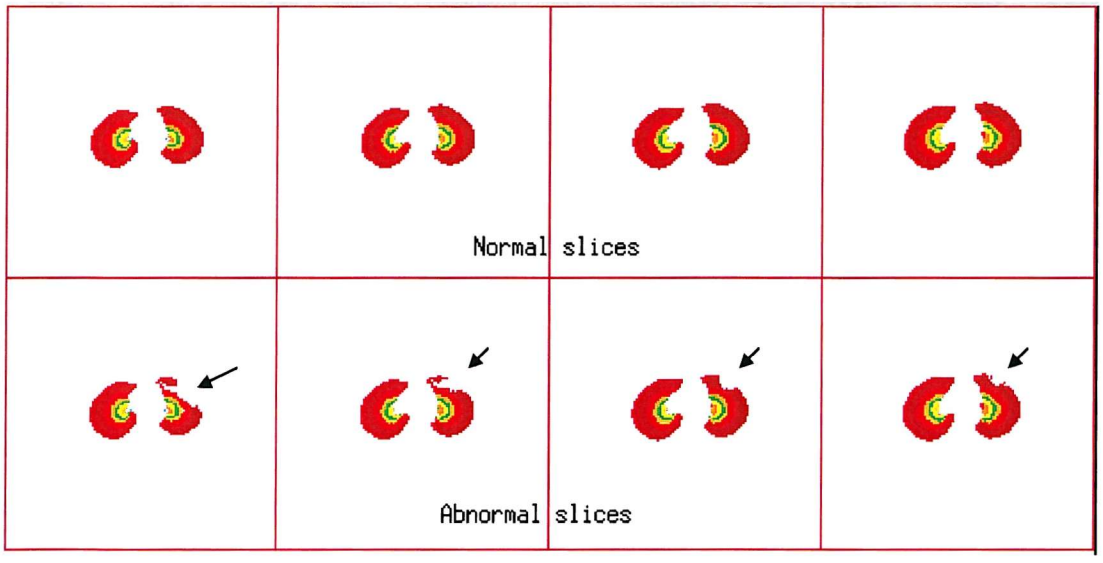

Figure 6.3: Example transaxial slices of the activity distribution within the lung. The top row of images is taken from a normal distribution of activity. The lower row shows those of a distribution with a defect in the left lingular superior segment.

6.2.4 Method of Simulating Lung Images

In this investigation two sets of data have been produced, normal lung images without any defect and abnormal lung images with a segmental defect. For each of the nine subjects used in this study 19 images were created each with a segmental defect in a different segment, examples are shown in figure 6.4.

The typical lung image was simulated by using a previously described technique in chapter 4 for simulating gamma camera images (Fleming et al 1994, Fleming 1996). As it has been mentioned, the lung models were obtained from real magnetic resonance images (MRI) of the thorax in nine male subjects. For each data set eight lung views were simulated, anterior (ANT), right anterior oblique (RAO), left anterior oblique (LAO), posterior (POST), left posterior oblique (LPO), right posterior oblique (RPO), left lateral (LL) and right lateral (RL).

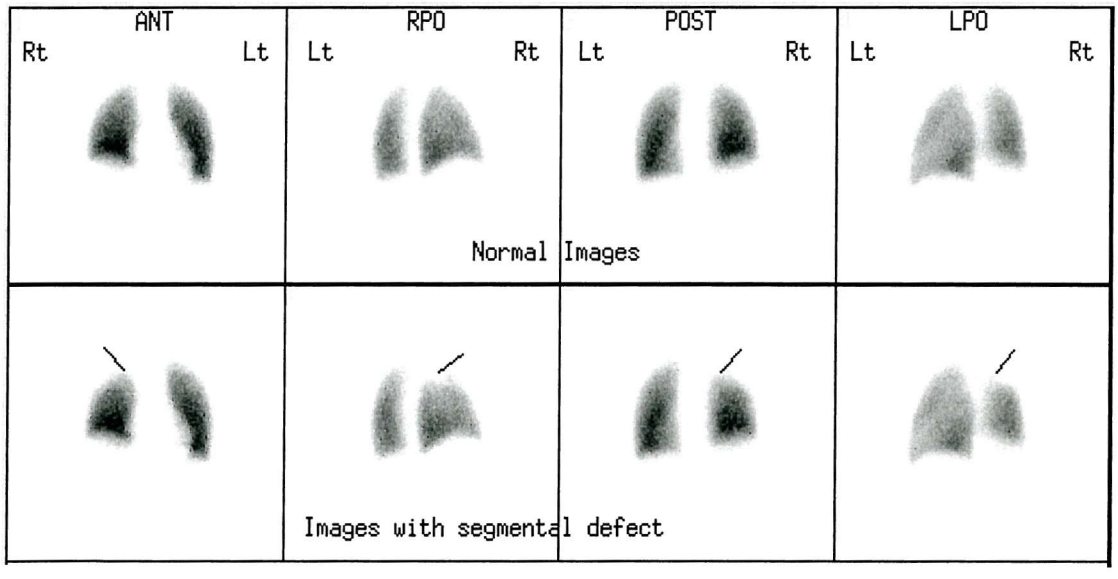

Figure 6.4: Normal images for the four views used in this study and the corresponding abnormal images with a defect in the segment.

All the views were simulated with the following parameters: 126 c/s/MBq gamma camera sensitivity, and 100 sec imaging time. Noise was added to all the simulations. All the images gave a total count of approximately 200 k counts, which is similar to the total count used in real V/Q scan. This corresponded to an activity of 50 MBq of ^{99m}Tc in the lung, which is well within ARSAC limits of this type of investigation.

Although some medical centres use the eight lung views and others use six views excluding the right and left anterior obliques (Morrel et al 1993), only four lung views (anterior, posterior, left posterior oblique and right posterior oblique) were used in this study, because these are the views usually acquired in clinical practice in Southampton General Hospital, Nuclear Medicine Department.

The data sets prepared for viewing by clinicians consisted of four perfusion views and four ventilation views. The four ventilation views each consisted of one particular realisation of the simulation of a normal distribution of activity. A normal perfusion data set consisted of a second realisation of the simulation of a normal distribution. Normal ventilation and perfusion images, therefore, differed in their noise characteristic. The images of the lung with segmental defects were presented to experienced nuclear medicine physicians, to check the visual appearance of the defects compared to real lung images. Some segments were excluded from this study due to their obvious visual appearance to the interpreter, which might decrease the chance of assessing the difference in the ability of the three image processing techniques in processing nuclear medicine planar images.

6.2.5 Method of Creating a Segmental Guidance for Interpretation

When interpreting the V/Q lung scan images for the diagnosis of pulmonary embolism based on the presence of mismatched segmental or subsegmental defects, nuclear medicine physicians normally use a guide for identifying the lung segments. This is in the form of a crib, consisting of an outline of the segmental anatomy from each view. In this study, instead of using an anatomical outline, the segmental defects were simulated in the normal lung views (anterior, posterior, left posterior oblique and right posterior

oblique), to allow real visualisation of the appearance of the segments on the images. It was impossible to create all the segmental defects in one view, therefore, in each view one or two segments and at most three, for both lungs (right and left) were created (Figure 6.5). The segments in the image appears as a "cold" area in which there are reduced counts. For each lung view there were three noise-free images of the lung, containing segmental defects each identified with the name of each segment as it appears in the different positions. This was used by the interpreters as a guide to identify the location of each segment in this study.

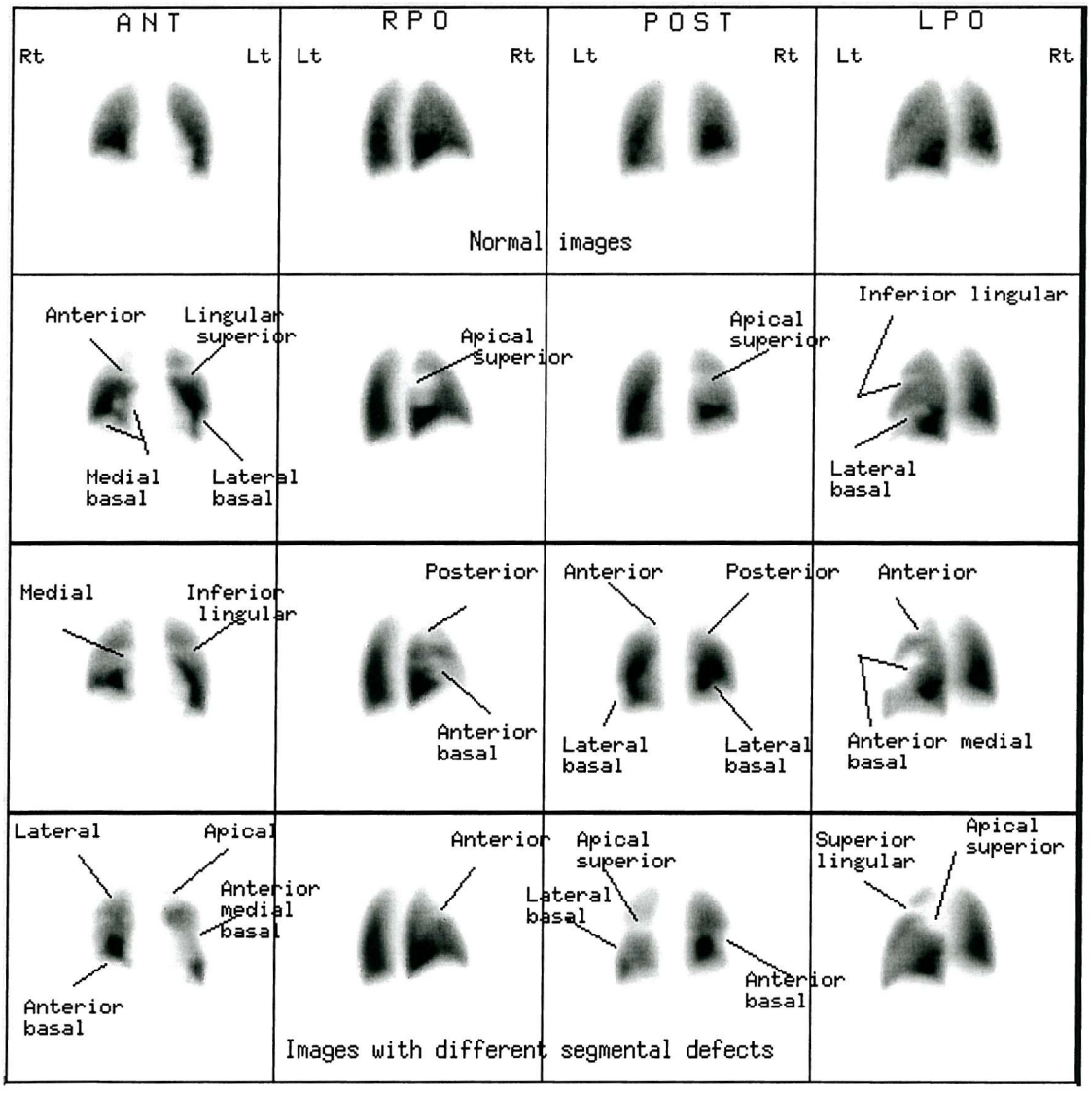

Figure 6.5: Simulation of a crib showing the appearance of segmental defects on the different noise-free views. The upper four views are for normal lung image, where the lower twelve views represented the segmental defects.

6.2.6 Image Processing

All the images with or without segmental defect (abnormal and normal simulated lung images), were processed by ME, WF and SM techniques. This was carried out using the results from the previous investigation described in chapter 5, where the parameters required by the three image processing techniques were defined to attain images with similar level of noise. However with the lung images it was not easy to obtain an estimate of the noise level as noise was superimposed on the real features in the image. It was therefore decided that as far as possible the same processing parameters would be used for the different techniques as in the experiment on the simulated planar phantom. This was considered justified as the counts per pixel in the lung images were similar to those in the planar phantom. Therefore the processing of the simulated lung images was performed by using one pass of the nine point filter for SM technique, point spread function FWHM 5.5 mm for WF technique and C_1 = 0.6 for ME technique. An exception is the value for parameter C_2 for the ME technique, where convergence of the algorithm to give solutions for some of the simulated lung images was not possible at the operating point of C_2 = 4.5 . Therefore, all the images were processed by ME technique using a value of C_1 = 0.6 and a value of parameter C_2 between 0.5 - 7.0, selected as described below.

6.2.6.1 Method of Choosing the Maximum Entropy Solution for Evaluation

In this investigation all the images which has been processed by SM and WF image processing techniques according to the previously defined parameters were used for evaluation. However the images parameters for the ME image processing technique had to be chosen using a different approach.

Therefore the aim was to use ME technique to process the lung images using a rule derived from its use on the planar images to produce images with approximately the same level of noise as the other techniques.

The rule used is similar in concept to that described in chapter 3. For any image, ME processing using a fixed value of C_1 , produces solutions for a range of values of C_2, C_{2min} to C_{2max} . Outside this range the algorithm does not converge. The image corresponding to C_{2min} is a noisy sharp image while that corresponding to C_{2max} is a smoother lower resolution image. The problem is that this range over which solutions can be obtained varies with different images. The hypothesis is that to obtain solutions of a given noise level, ME should be operated at C_2 value C_{2op} which is a fixed percentage **f**, along the range of values for which solutions are obtained, i.e.,

$$C_{2op} = \mathbf{f} (C_{2max} - C_{2min}) + C_{2min} \qquad 6\text{-}1$$

From the previous investigation (Chapter 5) on the cold object planar study, the ME technique was operated with $C_1 = 0.6$ and $C_2 = 4.5$. These values were to give solutions with a noise level equivalent to one smooth of the data.

Using equation 6-1 the average value of **f** was obtained from the planar phantom experiment. The value of **f** was calculated to be 0.26 . For the simulated lung study images, the ME technique was applied with $C_1 = 0.6$ and C_2 varying over the range of convergence. The lower and upper limits of convergence, C_{2min} and $C_{2max.}$, were noted for each lung view (anterior, posterior, left posterior oblique and right posterior oblique). Then the operational value of C_2 was calculated from equation 6-1 using a value of **f** of 0.26 .

6.2.7 Image Evaluation using ROC Analysis

Subjective visual interpretation of images is almost universally used in clinical practice of ventilation / perfusion imaging. Therefore evaluation of the performance of the different image processing techniques with this technique is required.

In this investigation the simulated lung images obtained by the maximum entropy image processing technique will be analysed and compared with the non-processed (raw data) images and the results obtained by using Wiener filtering and conventional

smoothing image processing techniques. Twenty sets of simulated lung images were used, each set representing one patient with four lung views (anterior, posterior, left posterior oblique and right posterior oblique) of both ventilation and perfusion. The perfusion images each had a single segmental defect located in the right or left lung side. Nine normal simulated lung images were also created in which both ventilation and perfusion were normal. There were therefore 29 sets of raw data images which were each processed by the three techniques giving a total of 116 data sets and therefore 928 images (i.e., raw data and processed images). Example of these images are shown in figure 6.6 . All data sets were evaluated by the previously described and widely used approach, receiver operating characteristic (ROC) analysis.

6.2.7.1 Interpretation of Images

The 928 images were saved in one file using PICS Program (Portable Imaging Computer System) (Fleming et al 1991), which is a medical image processing software system running on a UNIX Sun Sparcstation. The data sets were randomly ordered to avoid any reading-order effect (Metz 1989). The randomisation was obtained by locating each of the raw data V/Q images and its processed images, in different location order in the file. That was done to avoid locating the raw data and its processed images closer to each other. Two experienced observers were used to read these images, one is a nuclear medicine physicist (consultant). and the second is a nuclear medicine physician (consultant). The observers were instructed that the experiment was designed to test their ability to detect a PE (i.e., defected segment) on the simulated lung images and also, to test the ability of the three different image processing techniques. Each observer was provided with a two-page set of "Instructions to Observer", to clarify the procedure which needs to be followed in reading the images. It described the task, defining carefully the abnormalities to be reported in the study and, also the sheet containing examples of images with defects which they will use as a guide.

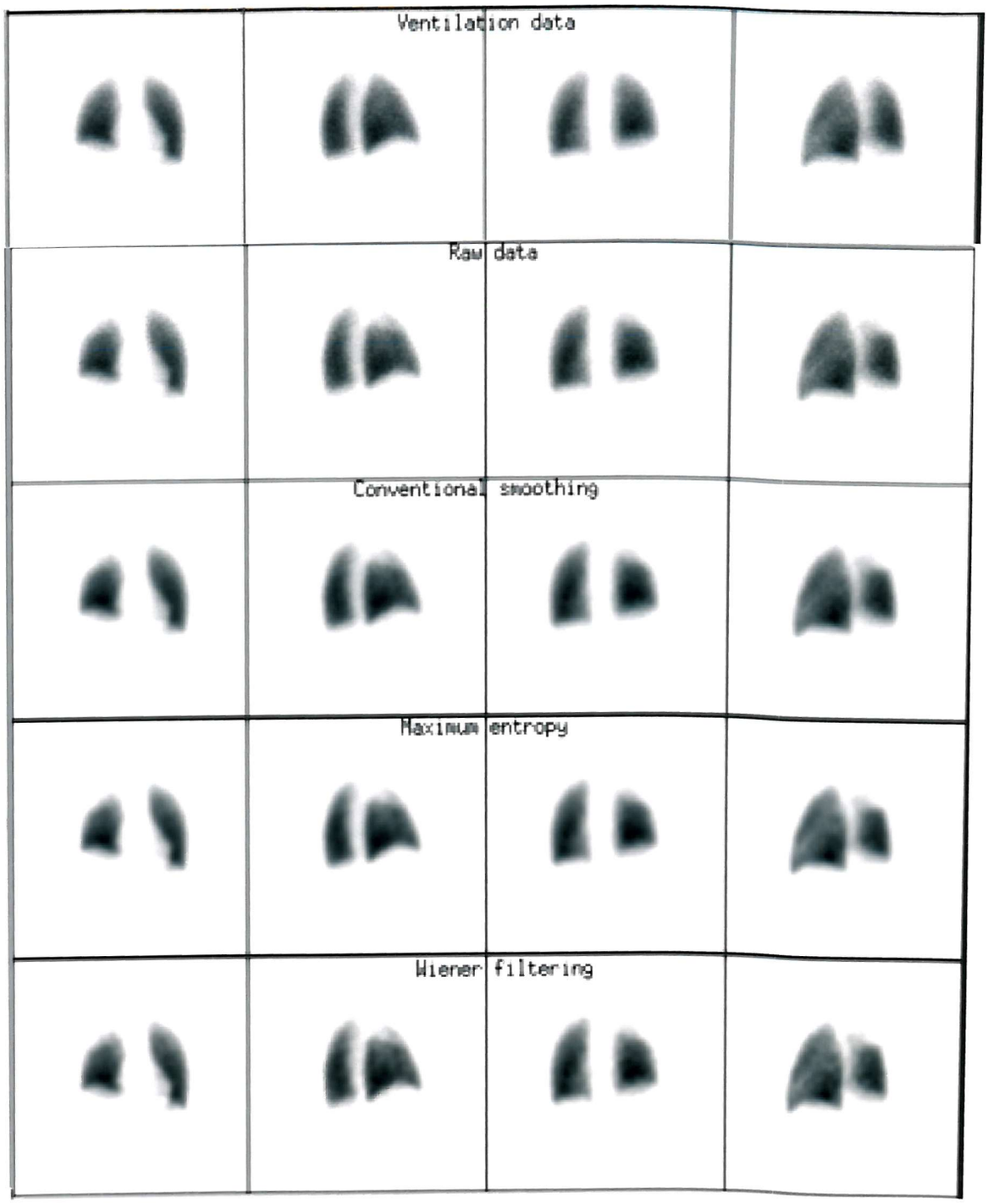

Figure 6.6: Example of the lung images used in the evaluation of the three image processing techniques. That is, the anterior, right posterior oblique, posterior and left posterior oblique planar lung images, of the ventilation data (top row) and the perfusion raw data (second row). The third, fourth and fifth rows show the images when processed by conventional smoothing, maximum entropy and Wiener filtering techniques, respectively.

The observers were instructed to interpret each set of images as follows:

(i) To detect the PE defect and its location in each set of images and subdivide his/her response into five levels of confidence if using the discrete rating scale, as the following rating scale:

1 = Definitely no PE present

2 = Fairly certain no PE present

3 = Equivocal

4 = Fairly certain PE present

5 = Definitely PE present

Or if using the continuous rating scale a subjective probability estimate (ranging from 0% - 100%) was used as follow:

0% - 9% = Definitely no PE present

10% - 39 % = Fairly certain no PE present

40% - 75 % = Equivocal

76% - 89 % = Fairly certain PE present

90% - 100% = Definitely PE present

(ii) The PE defect is located in one of the lung segments as indicated in the example sheet.

(iii) If no PE defect were detected and a decision were given such as "Definitely no PE present" then all the appropriate boxes should be ticked (✓).

(iv) If a decision is made the observer needs to fill in the location of his/her response according to the corresponding level of confidence.

(v) There is no time restriction for interpretation of each image.

(vi) The observer is free to change the display size, the contrast and brightness of the images according to his/her need (i.e., to use the workstation fully), however no image processing is permitted.

(vii) Each observer is free to repeatedly change his/her response to each image until a decision is made.

(viii) If any ambiguities are raised, they can be discussed individually with the researcher.

Also the observers were provided with a set of tables one for each of the 116 data sets which were to be completed so as to contain the level of confidence and the location (i.e., the percentage of confidence for the continuous scale which was explained earlier in chapter 5) of each PE in the image. To display the images the two observers interpreted the data one using Sun SparcStation 2 and the other used Vision workstation (SMV America, Software, USA).

6.2.7.2 Analysis of Results

The results from each of the observers were collected, categorised and then analysed using the ROC program, developed by Metz et al (1990), which are based on the Dorfman and Alf (1969) approach.

As has been explained earlier, this program calculates maximum-likelihood estimates of binormal ROC curves, including the area under each curve and its standard deviation, from data collected on discrete and continuous scales (please see section 5.2.5.2.2).

The statistical significance was calculated between the result obtained from the raw data, conventional smoothing, maximum entropy and Wiener filtering image processing techniques. Six comparisons were made as follows:

(i) Raw data versus Conventional smoothing
(ii) Raw data versus Maximum entropy
(iii) Raw data versus Wiener filtering
(iv) Conventional smoothing versus Maximum entropy
(v) Conventional smoothing versus Wiener filtering
(vi) Maximum entropy versus Wiener filtering

6.3 Results

In this investigation two sets of simulated lung images were created, the first set consisted of abnormal lung images with an area of reduced counts representing a lung image with a PE in one of its segments. The second set of images consisted of normal lung images, represented by simulated lung images without any segmental defect. The results shows that the appearance of some of the segmental defects were obvious to the interpreter, whereas others were more subtle, so out of the 19 segmental defects created only nine were used.

The ability of the three different image processing techniques to improve detectability was assessed subjectively by applying receiver operating characteristic (ROC) analysis. The sensitivity (TPF) and specificity (1 - FPF) of detection of abnormalities were calculated for the raw data and its processing by conventional smoothing, maximum entropy and Wiener filtering techniques. The results of analysis of the data for both observers are presented in figure 6.7a and b.

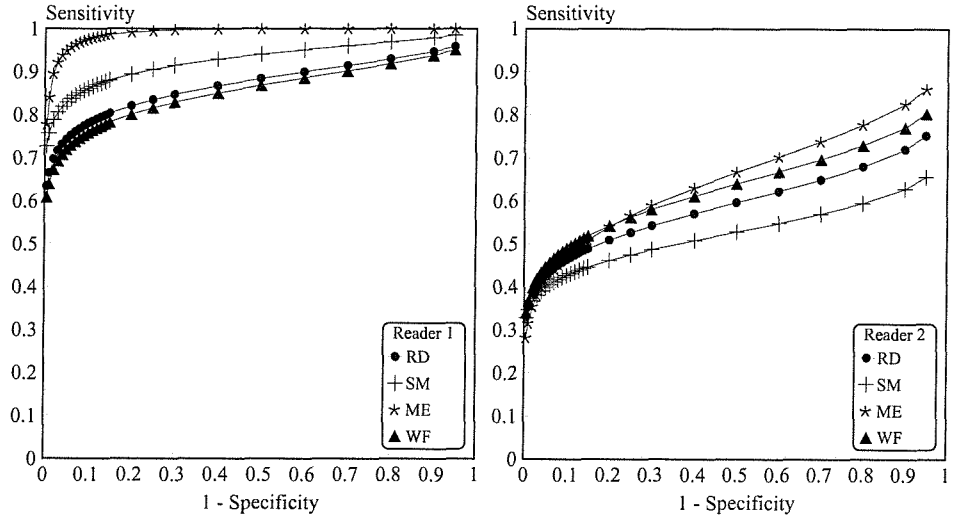

Figure 6.7: The ROC curves obtained for (a) reader 1 and (b) reader 2 in interpreting the data set of lung images using the different processing techniques.

The area and TPF tests were chosen for the statistical analysis of the data. The tests compute the statistical significance of the difference between the areas under the ROC curves and the difference between the FPF at a 0.1 FPF point respectively. The null hypothesis is that each two sets of rating data arose from ROC curves with equal area beneath them.

That analysis was applied to each reader's rating data. The area under the ROC curve and its standard error, for each reader in each condition (the RD, SM, WF and ME) was calculated and the sensitivity at a false positive fraction of 0.1 was defined. The results of statistical comparison between the three image processing techniques are shown in table 6.2.

The results of both the area and TPF tests performed, comparing each two ROC curves within readers, is expressed in terms of the two-tailed P-value. The two-tailed P-value represents the confidence with which the null hypothesis can be rejected. Lower P-values indicate more confidence in the statistical significance of the observed difference between the three image processing techniques.

	Reader 1				Reader 2			
	Area test		TPF test		Area test		TPF test	
Imaging technique	AUC (SE)	P-value for AUC	TPF at FPF= 0.1	P-value for TPF test	AUC (SE)	P-value for AUC	TPF at FPF= 0.1	P-value for TPF test
Raw data	0.84(0.062)	0.113	0.78	0.145	0.68(0.0794)	0.478	0.46	0.887
Conventional smoothing	0.92(0.0444)		0.86		0.67(0.0804)		0.43	
Raw data	0.84(0.062)	0.032	0.78	0.039	0.68(0.0794)	0.472	0.46	0.584
Maximum entropy	0.99(0.0149)		0.98		0.7(0.0779)		0.42	
Raw data	0.84(0.062)	0.547	0.78	0.545	0.68(0.0794)	0.814	0.46	0.518
Wiener filtering	0.81(0.066)		0.77		0.69(0.0784)		0.5	
Conventional smoothing	0.92(0.0444)	0.105	0.86	0.084	0.67(0.0804)	0.246	0.43	0.557
Maximum entropy	0.99(0.0149)		0.98		0.7(0.0779)		0.42	
Conventional smoothing	0.92(0.0444)	0.107	0.86	0.168	0.67(0.0804)	0.578	0.43	0.254
Wiener filtering	0.81(0.066)		0.77		0.69(0.0784)		0.5	
Maximum entropy	0.99(0.0149)	0.024	0.98	0.032	0.7(0.0779)	0.486	0.42	0.799
Wiener filtering	0.81(0.066)		0.77		0.69(0.0784)		0.5	

Table 6.2: Estimates of the binormal ROC parameters and the inter-condition coefficients for the area under the estimated ROC curve. For both true positive fraction (TPF) test at false positive fraction (FPF) = 0.1 and area test, for both readers.

Analysis of these results for the first reader using the true positive fraction test at false positive fraction = 0.1 showed that the sensitivity of maximum entropy, conventional smoothing and the raw data were better than the Wiener filtering technique (TPF = 0.77) being highest for maximum entropy (TPF = 0.98) . Conventional smoothing and Wiener filtering techniques did not perform significantly better ($P > 0.05$) in processing the raw data. But maximum entropy performed significantly better ($P = 0.039$) in processing the raw data. The analysis for the comparison between conventional smoothing versus maximum entropy and conventional smoothing versus Wiener filtering techniques was not significant ($P > 0.05$), although the comparison between maximum entropy versus Wiener filtering techniques was significant ($P < 0.05$). Similar results were obtained when the area under ROC curve was used for obtaining the significance between each comparison.

The results obtained from the second reader for the six comparisons using the true positive fraction test at 0.1 false positive fraction showed that there is no significant difference between any of the comparisons ($P > 0.05$). Similar results were obtained when the area under ROC curve was used for obtaining the significance between each comparison. The sensitivity of Wiener filtering, maximum entropy and the raw data were higher than conventional smoothing (TPF = 0.43) being highest for Wiener filtering (TPF = 0.51).

The results obtained from both readers for the raw data and the three image processing techniques were compared for investigating the significance of the difference between their interpretation and summarised in table 6.3. Both readers results are shown in figure 6.8 a, b, c, and d . Applying the true positive fraction test at 0.1 false positive fraction, shows that the two readers interpreted the images of the raw data and the images processed by the three image processing techniques differently and that difference was statistically significant. When the area under curve test was applied, for interpreting the raw data and maximum entropy images their was no significant difference in the result of obtained from both readers ($P > 0.05$), although their was a significant difference in the interpretation of the conventional smoothing and Wiener filtering images ($P < 0.05$).

When the results from both readers were averaged (Table 6.3), for the area under the ROC curve and the sensitivity at FPF = 0.1, the sensitivity of the three techniques in processing the raw data were proved to be in the order of : maximum entropy, conventional smoothing and Wiener filter.

Imaging technique		Area test			TPF test		
		AUC (SE)	P-value for AUC	Average of AUC	TPF at FPF =0.1	P-value for TPF test	Average of TPF
Raw data	*Reader 1*	0.84(0.062)	0.061	0.76	0.78	0.015	0.61
	Reader 2	0.68(0.0794)			0.44		
Conventional smoothing	*Reader 1*	0.92(0.0444)	0.004	0.795	0.86	0.002	0.645
	Reader 2	0.67(0.0804)			0.43		
Maximum entropy	*Reader 1*	0.99(0.0149)	0.132	0.845	0.98	0.008	0.73
	Reader 2	0.7(0.0779)			0.48		
Wiener filter	*Reader 1*	0.81(0.066)	0.049	0.75	0.77	0.038	0.64
	Reader 2	0.69(0.0784)			0.51		

Table 6.3: Comparing both readers result for testing any significant trends in interpreting the lung images.

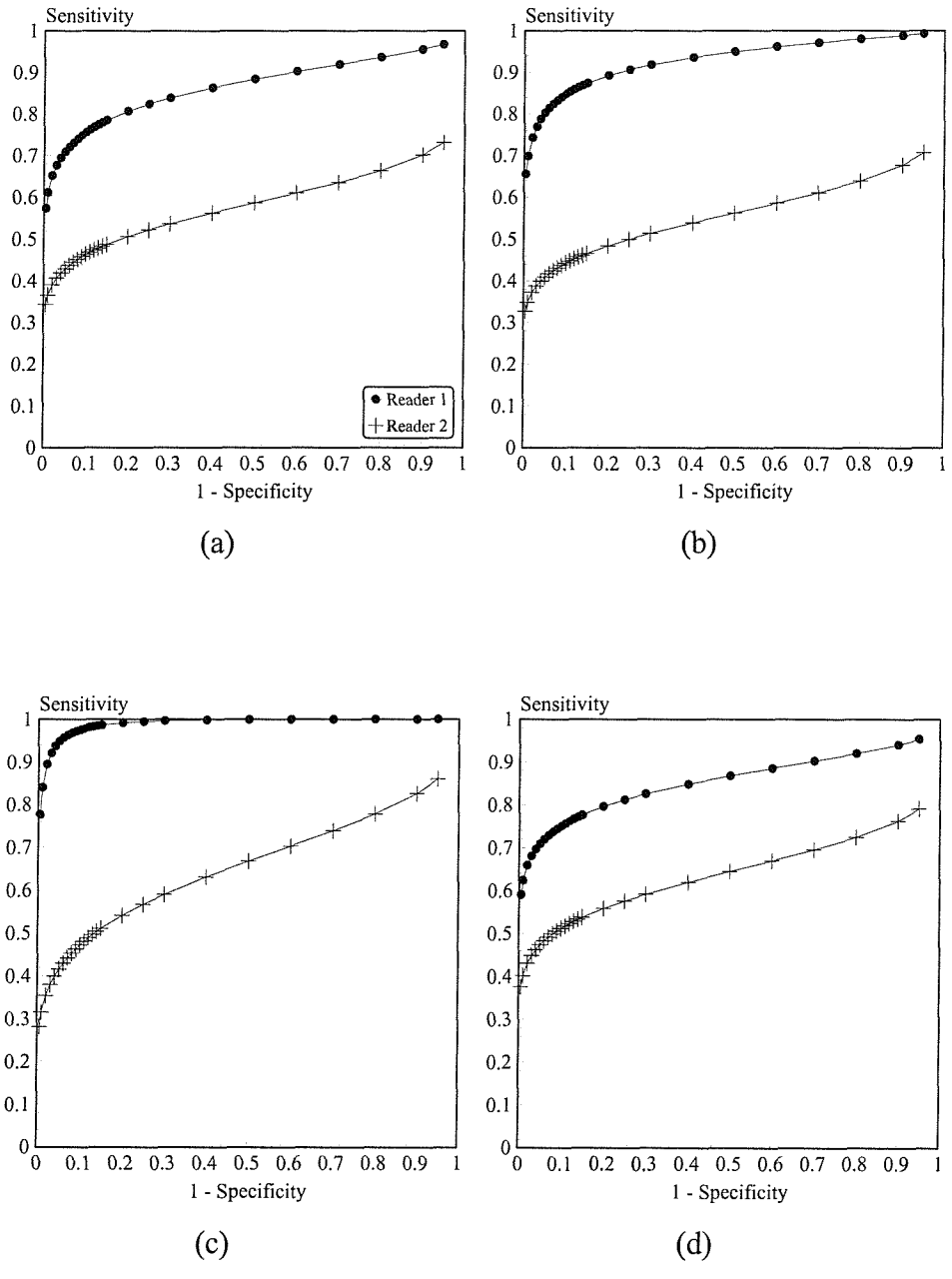

Figure 6.8: The ROC curves obtained from both readers for (a) raw data (b) conventional smoothing (c) maximum entropy and (d) Wiener filtering, for interpreting the data set of lung images.

Also there was a significant correlation in the results obtained from both parameters (i.e., TPF test and AUC test) used to assess image interpretation (Figure 6.9).

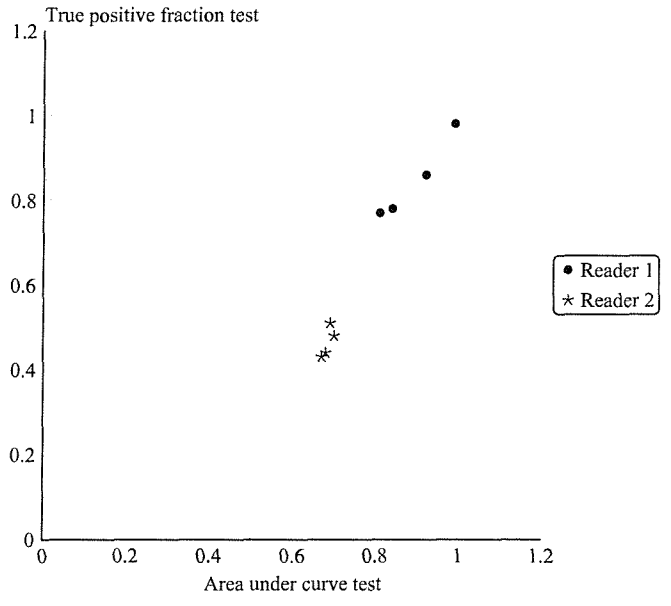

Figure 6.9: The correlation between area under curve (AUC) test and true positive fraction (TPF) test for the first reader (•), and the second reader (*).

6.4 Discussion

The assessment of image processing techniques requires their interpretation to be compared to that of the gold standard of the true diagnosis. In many clinical situations this is not generally available and the diagnosis of PE is one such example. Therefore simulated images which enable truth to be known provide a useful way of evaluating the different image processing algorithms. The use of simulation also has its limitations. The diagnostic process in nuclear medicine imaging depends on two separate components:

(i) the physiological uptake of the radiopharmaceutical being different in the diseased part of the organ being different from normal.
(ii) the gamma camera being able to adequately represent the activity distribution.

In the simulation technique described here only the second component of this process is being tested. In addition a clinician reporting a V/Q scan will have other information to hand in addition to the scan itself, such as the patient's history and an x-ray. Despite these limitation, still has an important role to play in giving a clear evaluation of the image interpretation process itself, uncomplicated by other factors on which a clinical diagnosis will depend.

In this investigation simulated lung images have been used to evaluate the three image processing techniques. These techniques produce a variety of images which are different in quality. The parameters required by the three image processing techniques were defined according to the results obtained from the previous investigation in chapter 5 . These parameters were chosen to give images with a similar level of noise.

For Wiener filtering (WF) and conventional smoothing (SM) this was straightforward as the same parameters could be used. However for maximum entropy (ME) a more complicated regime had to be employed due to the fact that not all the images converged for a fixed value of error parameter C_2 . This represents a significant disadvantage in the practical use of ME, in that a range of solutions have to be created to allow a consistent operation of the technique.

ROC analysis has been used to test the ability of the three image processing techniques to enhance and improve the detectability of images. The first reader ranked the three image processing techniques as follows, maximum entropy, conventional smoothing and Wiener filter, while the second reader ranked them as, maximum entropy, Wiener filter and conventional smoothing. The results obtained from the first reader indicated that the conventional smoothing and Wiener filtering techniques did not perform significantly better than the raw data ($P > 0.05$). The maximum entropy result was significantly different from the raw data, but not from conventional smoothing and Wiener filter techniques. The maximum entropy result was higher in its sensitivity

(TPF) at a low false positive fraction (FPF) value of 0.1 or using the area under the ROC curve (AUC), indicating the improvement in image quality. However in the case of the second reader none of the three image processing techniques gives any significantly different result compared to the raw data, when applying both the area under the ROC curve test or the true positive fraction (TPF) test ($P > 0.05$). Also none of the techniques was significantly better than the other ($P > 0.05$). The sensitivity of the Wiener filter image processing technique was the highest (TPF = 0.51) at FPF = 0.1, but the maximum entropy technique gives the highest value for the area under the curve (AUC = 0.7).

There was a clear difference in the two readers interpretation of the images. Reader 1 had a higher ROC curve for all sets of images, which was significant in each case using the TPF test. Therefore the results are not consistent across both observers. That could be due to the variation in their perception. It is noticeable that the two readers are varied in their degree of training and experience. Therefore their method of interpreting the data was different. The first reader planned a strategy of detection to obtain the fine differences in image appearance. A set of reference images was first established defining typical percentage detectabilities across the range 0 - 100 %. Each image was then compared to this baseline data set using careful adjustment of the upper contrast level to determine the value at which objects disappeared. Considerable care was taken over each evaluation. Reader 2 reported the images much more quickly and essentially recorded his initial impression of objects which were clearly seen in the image. He used the discrete five point scale (see section 5.2.5.2.3) in reporting. This might represent the clinical reporting of nuclear medicine images by nuclear medicine clinicians which does not depend on the image only, it requires a patient's history and certain other medical information.

6.5 Conclusion

This investigation has shown that the improvements of image processing observed on a planar object are not so clearly seen in this example of a clinical study. This is not surprising for several reasons. The two deconvolution techniques would not be expected

to operate so effectively as the convolution model describing their operation does not apply exactly to the imaging of a three dimensional object. In a 3D object the point spread function (PSF) is varying at different depths whereas the ME and WF techniques assume a single PSF. There were also limitations in the numbers of images that could be used in the ROC experiment, due to the long time required for evaluation and lack of availability of that time for the readers. In retrospect the experiment could probably have been improved using subsegmental defects instead of segmental defects, as this would have provided more features around the threshold of detectability; segmental defects were generally too obvious.

Despite these deficiencies the study was able to demonstrate that ME did produce a significant improvement for one of the readers. This suggests it may be of value in improving diagnostic accuracy for some observers and is worthy of further study.

The practical application of ME in this study was hampered by the difficulty of defining the error parameters. The new method of ME processing, recently developed (McGrath 1998) in which parameters are predefined may be of value in this respect.

Chapter Seven

Conclusions and Future Work

In this chapter a summary of the findings of this study will be put into context of previous work that has been carried out. It will also discuss future work that is indicated as a result of the work

7.1 Practical Implementation of Maximum Entropy

The practical application of ME requires several parameters to be defined. The technique will also only converge for a limited range of parameters. In this study an investigation of the influence of parameter values on image quality has been carried out. This data has then been used to develop rules for using the technique in practice. The requirement of defining these parameters is, however, still a drawback of the technique and further work is required in this area. A new technique for application of ME not requiring parameter definition has recently be developed in which the data errors required are obtained iteratively (McGrath 1998). This is currently of promise, but requires fuller evaluation.

Another practical aspect of the technique is the time it takes to operate. The current algorithm takes about 30 sec to process a 128×128 image. This is a little long for routine application. However, the code has not been optimised for speed and is being run on a relatively old computer. Therefore it is anticipated that considerable

improvements in running time could be achieved if routine application were required.

7.2 Assessment of Image Quality using a Figure of Merit

Objective quantitative measures of image performance are of potential value in evaluating quality. However, they require accurate and reproducible values of contrast and noise to be measured from the images. With planar radionuclide imaging this can only be achieved easily by imaging planar objects. Even in this situation the study has shown that care needs to be taken in defining the regions of interest in the image used to evaluate contrast and noise. When measured carefully, the FOM used in this study (i.e., FOM2) did show correlation with observer detectability (Chapter 5). For a given observer using a particular processing technique there was a significant correlation in each case. However, the correlations were not exact and there was considerable variability in detectability for a given figure of merit. The data from the different processing techniques varied monotonically with the corresponding mean FOM2. However, for only one of the observers did the results from the raw data fit into this same pattern. For the other observer the detectability for the raw data was considerably higher than expected based on the FOM2.

FOM2 values are clearly giving useful information on image performance and in particular on the relative values of image processing techniques. However, their direct relation to detectability of objects needs to be interpreted with some care.

7.3 Comparative Evaluation of Maximum Entropy Processing

A lot of work has been carried out on the application of image processing in planar radionuclide imaging. This has generally led to little clear advantage in clinical practice although some recent work show that there is evidence for improved diagnostic accuracy (Mountford 1998). In this study the immediate visual impact of

all the image processing techniques is confirmed as being quite subtle. However, quantitative evaluation using FOM2 analysis on planar objects shows quite clearly image processing is providing improvements. ROC data provided less clear evidence although for one observer all the processing techniques gave improved detectability compared to the raw data. This suggests that all the forms of processing studied may be of value for some observers. However, for the simulated lung data the ROC study showed little evidence of the advantage of image processing. Only the ME technique for one observer showed a significant improvement over the unprocessed images.

The results suggest that maximum entropy does perform better than other image processing techniques. In the planar image study it gave the best results from the FOM2 analysis and for both observers using the ROC. In the lung study ME was the only technique to show a significant improvement over the raw data, although this was only true for one of the observers. This suggests that further work to prove its value in clinical imaging is indicated. Thus there is still hope of potential clinical application to either in improving diagnostic accuracy or in achieving similar accuracy with lower count images leading to dose-reduction or shortening of imaging times.

7.4 Use of Simulation in Evaluation of Image Interpretation

The simulation of images has been used in this investigation to substitute the real clinical images. Its main value compared to the use of clinical data is that the true image distribution is known and can be used as a gold standard to compare the performance of different techniques. It also allows the influence of various parameters on the image quality and interpretation to be studied in a systematic manner. Its disadvantage lies in the difficulty of simulating all aspects of clinical imaging, both of the physical imaging process and more particularly of the clinical context in which image interpretation occurs, such as other prior information about the patient condition. Nevertheless simulation does provide a very useful way of studying the influence of image formation process on the detection of abnormalities.

7.5 Visual Image Interpretation

The results shows a clear difference between the diagnostic accuracies achieved by the two readers. This can be due to different circumstances such as, the individual methods of interpretation from one reader to another and the number and type of images used in the investigation. Therefore it is suggested to perform more studies and increase the number of readers. The simulated lung images were useful on evaluating the performance of image processing techniques. However, most of the segmental defects were too easily seen to distinguish between the capabilities of different techniques. Therefore smaller sub-segmental defects would be likely to provide better differentiation between techniques.

7.6 Conclusion

ME has been adapted to be suitable for clinical use. It gave the best results for processing nuclear medicine planar images, among the techniques studied. This may assist in improving diagnostic accuracy or in obtaining similar quality images with less radioactivity given to the patient or shorter imaging times. It's clinical usefulness is not yet convincingly shown but is of sufficient promise to recommend further studies, both in V/Q scanning and other types of radionuclide investigations.

Bibliography

Abrams, H.L., Siegelman, S.S., Adams, D.F. and et al (1982). Computed tomography versus ultrasound of the adrenal gland: A prospective study. *Radiology* **143** 121-128.

Ackerman, L.V. and Green, P.J. (1972). Breast lesion classification by computer and xeroradiograph. *Microbiology and Pathology* **30** (4):1025-1035.

Agresti, A. (1989). A survey of models for repeated ordered categorical response data. *Statist.Med.* **8** 1209-1224.

Aird, E.G.A. (1975). *An Introduction to Medical Physics*, William Heinemann Medical Books.

Aird, E.G.A. (1988). *Basic Physics for Medical Imaging*, Heinemann Medical Books.

Al-Abdul Salam, A. (1998). Investigation of the use of the simulation in evaluation of image interpretation in radionuclide image. [Dissertation]. University of Surrey, UK. MSc.

Alderson, P.O., Vieras, F., Housholder, D.F., Mendenhall, K.G. and Wagner, H.N.Jr. (1979). Gated and cinematic perfusion lung imaging in dogs with experimental pulmonary embolism. *Journal of Nuclear Medicine* **20** 407-412.

Altman, D.G. and Bland, J.M. (1983). Measurement in medicine: The analysis of method comparison studies. *The Statistician* **32** 307-317.

Andrews, H.C. and Hunt, B.R. (1977). *Digital Image Restoration*, Prentice-Hall, Englewood Cliffs.

Andrus, W.S., Dreyfuss, J.R., Jaffer, F. and Bird, K.T. (1975). Interpretation of roentgenograms via interactive television. *Radiology* **116** 25-31.

Anger, H.O. (1958). Scintillation Camera. *The review of scientific instruments* **29** (1): 27-33.

Arlig, A., Jacobsson, L., Larsson, A., Ljungberg, M. and Wikkelso, C. (1997). Selection of collimator for rCBF studies and evaluation of triple-headed SPET using noise-resolution plots. *Nuclear Medicine Communications* **18** 655-661.

Armstrong II, J.D., Sorenson, J.A., Nelson, J.A., Tocino, I., Lester, P.D., Janes, J.O., Niklason, L.T. and Stanish, W. (1983). Clinical evaluation of unsharp masking

and slit scanning techniques in chest radiography. *Radiology* **147** 351-356.

Barrett, H.H., Gooley, T., Girodias, K., Rolland, J., White, T. and Yao, J. (1991). Linear discriminants and image quality. *Lecture Notes in Computer Science* **511** 458-473.

Barrett, H.H., Gooley, T., Girodias, K., Rolland, J., White, T. and Yao, J. (1992). Linear discriminants and image quality. *Image and Vision Computing* **10** (6):451-460.

Barrett, H.H. and Gmitro, A.F., (Eds.) (1993). Tomographic reconstruction using information-weighted spline smoothing. pp 373. Springer-Verlag.

Bartkiewicz, B., Huda, W. and McLellan, Y. (1991). Impact of gamma camera parameters on imaging performance, evaluated by reciever operating characteristic (ROC) analysis. *Phys.Med.Biol.* **36** (8):1065-1074.

Begg, C.B. and Greenes, R.A. (1983). Assessment of diagnostic tests when disease verification is subject to selection bias. *Biometrics* **39** 207-215.

Begg, C.B. and McNeil, B.J. (1988). Assessment of radologic tests: Control of bias and other design considerations. *Radiology* **167** 565-569.

Berbaum, K.S., Franken, E.A., Dorfman, D.D., Barloon, T., Ell, S.R., Lu, C.H., Smith, W. and Abu-Yousef, M.M. (1986). Tentative diagnoses facilitate the detection of diverse lesions in chest radiographs. *Invest Radiol* **21** 532-539.

Bergmann, H. (1995). Inter-laboratory comparison of imaging devices in nuclear medicine. *Radiation Protection Dosimetry* **57** (1-4):21-26.

Blackwell, R.J., Shirley, I., Farman, D.J. and Michael, C.A. (1975). Ultrasonic "B" scanning as a pregnancy test after less than six weeks' amenorrhoea. *British Journal of Obstetric and Gynecology* **82** 108-114.

Blahd, W.H. (1971). *Nuclear Medicine*, second edn. (McGraw-Hill Co).

Bland, J.M. and Altman, D.G. (1986). Statistical methods for assessing agreement between two methods of clinical measurement. *The Lancet* **February 8** 307-310.

Boardman, A.K. (1979). Constrained optimisation and its application to scintigraphy. *Phys.Med.Biol.*, **24** (2):363-371.

Boulfelfel, D., Rangayyan, R.M., Hahn, L.J. and Kloiber, R. (1992). Use of the geometric mean of opposing planar projections in pre-reconstruction restoration of SPECT images. *Phys.Med.Biol.*, **37** (10):1915-1929.

Boulfelfel, D., Rangayyan, R.M. and Kloiber, R. (1992). prereconstruction restoration

of myocardial single photon emission computed tomography images. *IEEE Transactions on Medical Imaging* **11** (3):336-341.

Boulfelfel, D., Rangayyan, R.M., Kloiber, R. and Kuduvalli, G.R. (1994). Two-dimentional restoration of single photon emission computed tomography images using the kalman filter. *IEEE Transactions on Medical Imaging* **13** (1):102-109.

Bowsher, J.E. and Floyd, C.E. (1991). Treatment of Compton scattering in maximum-likelihood, expectation-maximization reconstructions of SPECT images. *The Journal of Nuclear Medicine* **32** 1285-1291.

Brink, A.D. (1996). Using spatial information as an aid to maximum entropy image threshold selection. *Pattern Recognition Letters* **17** 29-36.

Brown, D.W. (1964). Digital computer analysis and display of the radionuclide scan. *Journal of Nuclear Medicine* **5** 802

Brown, M.L., Wahner, H.W., Hay, I.D., Hammel, T.C. and Gray, J.E. (1980). Adrenal scintigraphy: Comparison of Anger tomographic scanner and the large field gamma camera. *Journal of Nuclear Medicine* **21** 729-732.

Brown, S., Stockley, A.V. and Batchelor, S. (1985). Maximum entropy processing of nuclear medicine data. *Eur.J.Nucl.Med* **11**, A44(Abstract).

Bryan, R.K. and Skilling, J. (1980). Deconvolution by maximum entropy, as illustrated by application to the jet of M87. *Mon.Not.R.astr.Soc.* **191** 69-79.

BSI (1990). British standard recommendations for the presentation of theses and dissertations. BS 4821, pp.1-27. UK.

Bunch, P.C., Hamilton, J.F., Sanderson, G.K. and Simmons, A.H. (1978). A free-response approach to the measurement and characterization of radiographic-observer performance. *Journal of Applied Photographic Engineering* **4** (4):166-171.

Burgess, A.E., Wagner, R.F. and Barlow, H. (1981). Efficiency of human visual signal discrimination. *Science* **214** 93-94.

Burgess, A.E. and Ghandeharian, H. (1984). Visual signal detection. II. Signal-location identification. *J.Opt.Soc.Am.A* **1** (8):906-910.

Burgess, A.E. and Ghandeharian, H. (1984). Visual signal detection. I. Ability to use phase information. *J.Opt.Soc.Am.A* **1** (8):900-905.

Burgess, A.E. (1985). Visual signal detection. III. On Bayesian use of prior knowledge and cross correlation. *J.Opt.Soc.Am.A* **2** (9):1498-1507.

Buvat, I., Rodriguez-Villafuerte, M., Todd-Pokropek, A., Benali, H. and Paola, R.D.

(1995). Comparitive assessment of nine scatter correction methods based on spectral analysis using monte carlo simulation. *The Journal of Nuclear Medicine* **36** (8):1476-1488.

Calvetti, D. and Reichel, L. (1996). Application of iterative methods to the restoration of noisy images. *SIAM Journal on Marix Analysis and Application* **17** (1):165-186.

Carril, J.M., MacDonald, A.F., endy, P.P., eyes, W.I., ndril, P.E. and allard, J.R. (1979). Cranial scintigraphy: Value of adding emission computed tomographic sections to conventional pertechnetate images (512 cases). *Journal of Nuclear Medicine* **20** 1117-1123.

Cassen, B., Curtis, L., Reed, C. and Libby, R. (1951): Instrumentation for I^{131} use in medical studies. *Nucleonics* **9** (2): 46-50.

Castleman, K.R. (1979). *Digital Image Processing*, Prentice-Hall, Englewood Cliffs.

Chakraborty, D.P., Breatnach, E.S., Yester, M.V., Soto, B., Barnes, G.T. and Fraser, R.G. (1986). Digital and conventional chest imaging: A modified ROC study of observer performance using simulated nodules. *Radiology* **158** 35-39.

Chakraborty, D.P. (1989). Maximum likelihood analysis of free-response reciever operating characteristic (FROC) data. *Medical Physics* **16** (4):561-568.

Chakraborty, D.P. and Winter, L.H.L. (1990). Free-response methodology: Alternate analysis and a new observer-performance experiment. *Radiology* **174** 873-881.

Charalambous, C., Ghaddar, F.K. and Kouris, K. (1992). Two iterative image restoration algorithms with applications to nuclear medicine. *IEEE Transactions on Medical Imaging* **11** (1):2-8.

Charter, M.K. and Gull, S.F. (1987). Maximum entropy and its application to the calculation of drug absorption rates. *Journal of Pharmacokinetics and Biopharmaceutics* **15** (6):645-655.

Chesters, M.S. and Hay, G.A. (1983). Quantitative relation between detectability and noise power. *Phys.Med.Biol.* **28** (10):1113-1125.

Chesters, M.S. (1992). Human visual perception and ROC methodology in medical imaging. *Phys.Med.Biol.* **37** (7):1433-1476.

Chicco, P., Magnussen, J.S., Mackey, D.W., Murray, I.P.C. and Van Der Wall, H. (1997). Recognition of subsegmental scintigraphic defects in virtual lung scintigraphy. *Nuclear Medicine Communications* **18** 728-733.

Chinn, S. (1990). The assessment of methods of measurement. *Statist.Med.* **9** 351-362.

Cox, R.T. (1946). Probability, frequency and reasonable expectation. *American Journal of Physics* **14** (1):1-13.

Cuaron, A., Acero, A.P., Cardenas, M., Huerta, D., Rodriguez, A. and deGaray, R. (1980). Interobserver variability in the interpretation of myocardial images with Tc-99m-labeled diphosphonate and pyrophosphate. *Journal of Nuclear Medicine* **21** 1-9.

Daniell, G.J. and Gull, S.F. (1980). Maximum entropy algorithm applied to image enhancement. *IEE Proceedings* **127, Pt. E**, (5):170-172.

Daniell, G.J. (1991). Of maps and monkeys: An introduction to the maximum entropy method. In: Buck, B. and Macaulay, V.A., (Eds.) *Maximum Entropy in Action.*, Oxford University Press.

Davies, E.R. (1992). Accurate filter for removing impulse noise from one- or two-dimensional signals. *IEE Proceedings-E* **139** (2):111-116.

Delibasis, K.K., Undril, P.E. and Cameron, G.G. (1996). Genetic algorithm implementation of stack filter design for image restoration. *IEEProc.- Vis.Image Signal Process.* **143** (3):177-183.

DeLong, E.R. and DeLong, D.M. (1988). Comparing the areas under two or more correlated receiver operating characteristic curves: A nonparametric approach. *Biometrics* **44** 837-845.

Dendy, P.P., McNab, J.W., MacDonald, A.F., Keyes, W.I. and Carril, J.M. (1977). An evaluation of transverse axial emission tomography of the brain in the clinical situation . *British Journal of Radiology* **50** 555-561.

Dendy, P.P., Keyes, W.I., Reid, A. and et al. (1981). A clinical trial of the value of a tomographic section view to identify liver abnormalities by radionuclide imaging, with special reference to metastatic disease. *Eur.J.Nucl.Med* **6** 51-55.

Dendy, P.P., Barber, R.W. and Bayliss, C.C. (1988). An experimental study of the relationship between image quality and spatial resolution for the gamma camera. *Eur.J.Nucl.Med* **14** 579-585.

Dorfman, D.D. and Alf, E. (1969). Maximum likelihood estimation of parameters of signal detection theory and determination of confidence intervals-rating method data. *Journal of Mathematical Psychology* **6** 487-496.

Dorfman, D.D., Berbaum, K.S. and Metz, C.E. (1992). Receiver operating characteristic rating analysis: Generalization to the population of readers and patients with the jackknife method. *Invest Radiol* **27** 723-731.

Dorfman, D.D., Berbaum, K.S., Metz, C.E., Lenth, R.V., Hanley, J.A. and Dagga, H.A. (1996). Proper receiver operating characteristic analysis : The Bigamma model.

Acad Radiol **4** 138-149.

Eckelman, W.C. (1988). Radiopharmaceuticals. In: Gottschalk, A., Hoffer, P.B., Potchen, E.J. and Berger, H.J., (Eds.) *Diagnostic Nuclear Medicine*, pp. 150-163. Baltimore, Williams and Wilkins.

Egan, J.P., Greenberg, G.Z. and Schulman, A.I. (1961). Operating characteristics, singnal detectability, and the method of free response. *The Journal of the Acoustical Society of America* **33** (8):993-1007.

Ell, P., Todd-Pokropek, A. and Britton, K.E. (1975). Localisation of parathyroid adenomas by computer assisted parathyroid scanning. *British Journal of Surgery* **62** 553

Ffrench, P.A., Zeidler, J.R. and Ku, W.H. (1997). Enhanced detectability of small objects in correlated clutter using an improved 2-D adaptive lattice algorithm. *IEEE Transactions on Image Processing* **6** (3):383-397.

Fleiss, J.L. (1986). *The Design and Analysis of Clinical Experiments*,

Fleiss, J.L. and Davies, M. (1982). Jackknifing functions of multinomial frequences, with an application to a measure of concordance. *American Journal of Epidemiology* **115** (6):841-845.

Fleming, J.S. and Kenny, R.W. (1977). A comparison of techniques for the filtering of noise in the renogram. *Phys.Med.Biol.*, **22** (2):359-364.

Fleming, J.S., Britten, A.J., Perring, S., Keen, A.C. and Howlett, P.J. (1991). A general software package for the handling of medical images. *Journal of Medical Engineering & Technology* **15** (4/5):162-169.

Fleming, J.S. and Simpson, D.E. (1994). A technique for simulation of the point spread function of a gamma camera. *Phys.Med.Biol.* **39** 1457-1473.

Fleming, J.S. (1996). Evaluation of a technique for simulation of gamma camera images. *Phys.Med.Biol.* **41** 1855-1861.

Fleming, J.S., Halson, P., Conway, J.H., Moore, E., Nassim, M.A., Hashish, A.H., Bailey, A.G., Holgate, S.T. and Martonen, T.B. (1996). Three dimensional description of pulmonary deposition of inhaled aerosol using data from multimodality imaging . *The Journal of Nuclear Medicine.* **37** 873-877.

Fleming, J.S., Hashish, A.H., Conway, J.H., Hartley-Davies, R., Nassim, M.A., Guy, M.J., Coupe, J., Holgate, S.T., Moore, E., Bailey, A.G. and Martonen, T.B. (1997). A technique for simulating radionuclide images from the aerosol deposition pattern in the airway tree. *Journal of Aerosol Medicine* **10** (3):199-212.

Fleming, J.S., Conway, J.H., Holgate, S.T., Moore, E., Hashish, A.H., Bailey, A.G. and Martonen, T.B. (1998). Evaluation of the accuracy and precision of lung aerosol deposition measurements from planar radionuclide imaging using simulation. *Phys.Med.Biol.* **43** 2423-2429.

Floyd, C.E., Jaszczak, R.J., Greer, K.L. and Coleman, R.E. (1985). Deconvolution of Compton scatter in SPECT. *The Journal of Nuclear Medicine* **26** 403-408.

Franceschetti, G., Pascazio, V. and Schirinzi, G. (1995). Iterative homomorphic technique for speckle reduction in synthetic-aperture radar imaging. *J.Opt.Soc.Am.A* **12** (4):686-694.

Frieden, B.R. (1972). Restoring with maximum likelihood and maximum entropy. *J.Opt.Soc.Am.A* **62** (4):511-518.

Fryback, D.G. and Thornbury, J.R. (1991). The efficacy of diagnostic imaging. *Med Decis Making* **11** 88-94.

Fukuhisha, K., Tateno, Y., Iinuma, T.A. and et al. (1984). Evaluation of clinical efficacy of body x-ray computed tomography (XCT) for various hepatic and pancreatic diseases: I. A prospective study and several results. *NIPPON ACTA RADIOLOGICA* **44** 604-623.

Furuie, S.S., Herman, G.T., Narayan, T.K., Kinahan, P.E., Karp, J.S. and Lewitt, R.M. (1994). A methodology for testing for statistically significant differences between fully 3D PET reconstruction algorithms. *Phys.Med.Biol.* **39** 341-354.

Garra, B.S., Insana, M.F., Shawaker, T.H., Wagner, R.F., Bradford, M. and Russell, M. (1989). Detection and classification of diffuse liver disease comparison with human obsever performance. *Invest Radiol* **24** 196-203.

Glick, S.J., Penney, B.C., King, M.A. and Byrne, C.L. (1994). Noniterative compensation for the distance-dependent detector response and photon attenuation in SPECT imaging. *IEEE Transactions on Medical Imaging* **13** (2):363-374.

Goin, J.E., Haberman, J.D., Linder, M.K. and Lambird, P.A. (1983). Analysis of mammography: A blind interpretation of BCDDP radiographs. *Radiology* **148** 393-396.

Goodenough, D.J., Rossmann, K. and Lusted, L.B. (1973). Factors affecting the detectability of a simulated radiographic signals. *Investigative Radiology* **8** 339-344.

Gooley, T.A. and Barrett, H.H. (1992). Evaluation of statistical methods of image reconstruction through ROC analysis. *IEEE Transactions on Medical Imaging* **11** (2):276-283.

Gottschalk, A., Juni, J.E., Sostman, D., Coleman, R.E. and et al. (1993). Ventilation / perfusion scintigraphy in the PIOPED study. Part I. Data collection and tabulation. *Journal of Nuclear Medicine* **34** (7):1109-1118.

Gottschalk, A., Juni, J.E., Sostman, D., Coleman, R.E. and et al. (1993). Ventilation / perfusion scintigraphy in the PIOPED study. Part II. Evaluation of the scintigraphic criteria and interpretations. *Journal of Nuclear Medicine* **34** (7):1119-1126.

Gray, R.N. (1993). Pulmonary embolism. *Med Internat* **21** 474

Green, D.M. and Moses, F.L. (1966). On the equivalence of two recognition measures of short-term memory. *Psychological Bulletin* **66** 228-234.

Green, P.J. (1990). Bayesian reconstructions from emission tomography data using a modified EM algorithm. *IEEE Transactions on Medical Imaging* **9** (1):84-93.

Griner, P.F., Mayewski, R.J., Mushlin, A.I. and Greenland, P. (1981). Selection and interpretation of diagnostic tests and procedures. *Annals of Internal Medicine* **94** (4 (part 2)):559-563.

Guiss, L.W. and Kuenstler, P. (1960). A retrospective view of survey photofluorograms of persons with lung cancer. *Cancer* **13** 91-95.

Gull, S.F. and Daniell, G.J. (1978). Image reconstruction from incomplete and noisy data. *Nature* **272** (5655):686-690.

Gull, S.F. and Skilling, J. (1984). Maximum entropy method in image processing. *IEE Proceedings* **131, Pt. F** (6):646-659.

Gull, S.F. and Newton, T.J. (1986). Maximum entropy tomography. *Applied Optics* **25** (1):156-160.

Gull, S.F. (1989). Developments in maximum entropy data analysis. In: Skilling, J., (Ed.) *Maximum Entropy and Bayesian Methods, Fundamental Theories of Physics*, pp. 53-71. Kluwer Academic.

Halpern, E.J., Albert, M., Krieger, A.M., Metz, C.E. and Maidment, A.D. (1996). Comparision of receiver operating characteristic curves on the basis of optimal operating points. *Acad Radiol* **3** 245-253.

Hanley, J.A. and McNeil, B.J. (1982). The meaning and use of the area under a receiver operating characteristic (ROC) curve. *Radiology* **143** 29-36.

Hanley, J.A. and McNeil, B.J. (1983). A method of comparing the areas under receiver operating characteristic curves derived from the same cases. *Radiology* **148** 839-843.

Hanley, J.A. (1988). Alternative approaches to reciever operating characteristic analyses. *Radiology* **168** 568-570.

Hanley, J.A. (1989). Receiver operating characteristic (ROC) methodology: The state of the art. *Critical Reviews in Diagnostic Imaging* **29** (3):307-335.

Harmon, L.D. and Julesz, B. (1973). Masking in visual recognition: Effects of two-dimensional filtered noise. *Science* **180** 1194-1197.

Hart, G. (1997). A UK survey of nuclear medicine imaging performance using the TransBone anthropomorphic phantom. *Nuclear Medicine Communications* **18** 668-672.

Hart, H. and Liang, Z. (1987). Bayesian image processing in two dimensions. *IEEE Transactions on Medical Imaging* **MI-6** (3):201-208.

Hebert, T.J. and Gopal, S.S. (1992). The GEM MAP algorithm with 3-D SPECT system response. *IEEE Transactions on Medical Imaging* **11** (1):81-90.

Henkelman, R.M., Kay, I. and Bronskill, M.J. (1990). Receiver operator characteristic (ROC) analysis without truth. *Med Decis Making* **10** 24-29.

Herath, K.B. and Sharp, P.F. (1976). Effects of 'Matched Filter' smoothing as measured by receiver operating characteristic curve. *Phys.Med.Biol.*, **21** (3):442-446.

Herman, G.T. and Yeung, K.T.D. (1989). Evaluators of image reconstruction algorithms. *International Journal of Imaging Systems and Technology* **1** 187-195.

Herman, G.T. and Odhner, D. (1991). Performance Evaluation of an Iterative Image Reconstruction Algorithm for Positron emission tomography. *IEEE Transactions on Medical Imaging* **10** (3):336-346.

Herman, P.G., Drummey, J., Swensson, R.G., Hessel, S.J. and Balikian, J.P. (1982). 350 kV Chest radiography has no diagnostic advantage: A comparison with 140 kV technique. *American Journal of Roentgenology* **138** 485-489.

Hermann, G.A., Herrera, N. and Sugiura, H.T. (1982). Comparison of interlaboratory survey data in terms of receiver operating characteristic (ROC) indices. *Journal of Nuclear Medicine* **23** 525-531.

Hessel, S.J., Siegelman, S.S., McNeil, B.J. and et al (1982). A prospective evaluation of computed tomography and ultrasound of the pancreas. *Radiology* **143** 129-133.

Hon, T.C., Rangayyan, R.M., Hahn, L.J. and Kloiber, R. (1989). Restoration of Gamma Camera-Based Nuclear Medicine Images. *IEEE Transactions on Medical Imaging* **8** (4):354-363.

Houston, A.S. and Macleod, M.A. (1977). An intercomparison of computer assisted data processing and display methods in radioisotope scintigraphy using mathematical tumours. *Phys.Med.Biol.* **22** (6):1097-1114.

Houston, A.S., Sharp, P.F., Tofts, P.S. and Diffey, B.L. (1979). A multicentre comparison of computer assisted image processing and display methods in scintigraphy. *Phys.Med.Biol.*, **24** (3):547-558.

Houston, A.S. (1985). Uses of ROC analysis in nuclear medicine. *Clinical Physics and Physiological Measurment* **6** (2):173

Houston, A.S. and Sampson, W.F.D. (1989). Comparison of two interpolative background subtraction methods using phantom and clinical data. *Nuclear Medicine Communications* **10** 121-132.

Hunink, M.G., de Slegte, R.G.M., Gerritsen, G.J. and Speelman, H. (1990). CT and MRI assessment of tumors of the nose and paranasal sinuses, the nasopharynx and the parapharyngeal space using ROC. *Neuroradiology* **32** 220-225.

Hunter, B.V. and Leong, K.H. (1997). Improving fiber-optic laser beam delivery by incorporating GRADIUM optics. *Applied Optics* **36** (13):2763-2769.

Iinuma, T.A. and Nagai, T. (1967). Image restoration in radioisotope imaging systems. *Phys.Med.Biol.* **12** (4):501-509.

International Atomic Energy Agency (IAEA) (1977). IAEA Co-ordinated research programme on the intercomparison of computer-assissted scintigraphic techniques. *Medical Radionuclide Imaging* **1** 585-615.

Ishida, M., Doi, K., Loo, L.-N. and Metz, C.E. (1984). Digital image processing: effect on detectability of simulated low-contrast radiographic patterns. *Radiology* **150** 569-575.

Jones, D.E.A. and Raine, H.C. (1949). Correspondence. *British Journal of Radiology* **22** 549-550.

Joseph, P.M., Hilal, S.K., Schulz, R.A. and Kelcz, F. (1980). Clinical and experimental investigation of a smoothed ct reconstruction algorithm. *Radiology* **134** 507-516.

Judy, P.F., Swensson, R.G. and Szulc, M. (1981). Lesion detection and signal-to-noise ratio in CT images. *Medical Physics* **8** 13-23.

Judy, P.F. and Swensson, R.G. (1985). Detectability of lesions of various sizes on CT images. *Proceedings of SPIE* **535** 38-42.

Judy, P.F. and Swensson, R.G. (1985). Detection of small focal lesions in CT images: effects of reconstruction filters and visual display windows. *The British Journal*

of Radiology **58** 137-145.

Keeling, D.H. and Todd-Pokropek, A. (1969). Computer assisted parathyroid scanning. *Medical Radioisotope Scintigraphy* **1** 745

Kelsey, C.A., Moseley, R.D., Mettler, F.A. and Briscoe, D.E. (1982). Cost-effectiveness of stereoscopic radiographs in detection of lung nodules. *Radiology* **142** 611-613.

Kelsey, C.A., Moseley, R.D., Mettler, F.A., Garcia, J.F., Parker, T.W. and Briscoe, D.E. (1982). Comparison of nodule detection with 70-kVp and 120-kVp chest radiographs. *Radiology* **143** 609-611.

Kelsey, C.A., Moseley, R.D., Garcia, J.F., Parker, T.W., Juhl, J.H. and Briscoe, D.E. (1983). Anticrossover emulsions evaluated by observer performance tests. *Radiology* **146** 209-211.

Kelsey, C.A., Moseley, R.D., Garcia, J.F., Mettler, F.A., Parker, T.W. and Juhl, J.H. (1985). ROC and contrast detail image evaluation test compared. *Radiology* **154** 629-631.

Kemp, M.C. and Jarritt, P.H. (1982). Image reconstruction by maximum entropy. *IEEE Proceedings SPIE* 521-526.

Kemp, P.M., Cross, J., Flower, C.D.R., Dixon, A.K. and Wraight, E.P. (1997). Initial British experience in the use of spiral CT in the diagnosis of pulmonary embolism. *Nuclear Medicine Communications* **18** 318(Abstract).

Keyes, J.W.Jr., Singer, D., Satterlee, W., Kalff, V. and Harkness, B.A. (1984). Liver-spleen studies with the rotating gamma camera. II. Utility of tomography. *Radiology* **153** 537-541.

Kinahan, P.E. and Karp, J.S. (1994). Figures of merit for comparing reconstruction algorithms with a volume-imaging PET scanner. *Phys.Med.Biol.*, **39** 631-642.

King, J.L., Britton, C.A., Gur, D. and Rockette, H.E. (1993). On the validity of the continuous and discrete confidence rating scales in receiver operating characteristic studies. *Invest Radiol* **28** (10):962-963.

King, M.A., Doherty, P.W. and Schwinger, R.B. (1983). A Wiener filter for nuclear medicine images. *Medical Physics* **10** (6):876-880.

King, M.A., Schwinger, R.B., Doherty, P.W. and Penney, B.C. (1984). Two-dimensional filtering of spect images using the metz and wiener filters. *The Journal of Nuclear Medicine* **25** 1234-1240.

Kuhl, D.E., Chamberlain, R.H., Hale, J. and Gorson, R. (1956). A high-contrast photographic recorder for scintillation counter scanning. *Radiology* **66** 730-739.

Kuhl, D.E. and Edwards, R.Q. (1963). Image separation radioisotope scanning. *Radiology* **80** 653-662.

Kuhl, D.E. and Edwards, R.Q. (1968). Digital techniques for on-site scan processing. In: *Fundamental Problems in Scanning*, pp. 250. Thomas Springfield III

Kundel, H.L. (1972). Factors limiting roentgen interpretation-physical and psychologic. In: Potchen, E.J., (Ed.) *Current Concepts in Radiology.*, pp. 1-29. St louis: C.V. Mosby.

Kundel, H.L., Revesz, G. and Toto, L. (1979). Contrast gradient and the detection of lung nodules. *Invest Radiol* **14** 18-22.

Kundel, H.L. and Polansky, M. (1997). Mixture distribution and reciever operating characteristic analysis of bedside chest imaging with screen-film and computed radiography. *Acad Radiol* **4** 1-7.

Lalush, D.S. and Tsui, B.M.W. (1992). Simulation evaluation of gibbs prior distributions for use in maximum a posteriori SPECT reconstructions. *IEEE Transactions on Medical Imaging* **11** (2):267-275.

Lassen, M. and Bloch, P. (1978). Measurements of the effects of x-ray film-screen characteristics on threshold detectability of small low-contrast objects. *Medical Physics* **5** 152-161.

Lehr, J.L. and Capek, P. (1985). Histogram equalization of CT images. *Radiology* **154** 163-169.

Leinsinger, G., Kirsch, C.M., Kragh, P., Pletzer, G. and Lechel, U. (1991). Quantitative determination of uptake of I-131 Labeled Anti-CEA and CA 19-9 in liver metastases using SPECT. *Antibody Immunoconjugates and Radiopharmaceuticals* **4** (4):665-671.

Levitan, E. and Herman, G.T. (1987). A maximum a posteriori probability expectation maximization algorithm for image reconstruction in emission tomography. *IEEE Transactions on Medical Imaging* **MI-6** (3):185-192.

Liang, Z., Jaszczak, R. and Greer, K. (1989). On Bayesian image reconstruction from projections: uniform and nonuniform a priori source information. *IEEE Transactions on Medical Imaging* **8** (3):227-235.

Lieberman, D.E. (1977). *Computer methods: The fundamentals of digital nuclear medicine.*, St Louis: C.V. Mosby.

Lingxiong, S., Joel, S.K. and Pete, C. (1994). Practical considerations of the Wiener filtering technique on projection data for PET. *IEEE Transactions on Nuclear Science* **41** (4):1560-1565.

Links, J.M., Price, J.L. and Gupta, S.N. (1996). A vector Wiener filter for dual-radionuclide imaging. *IEEE Transactions on Medical Imaging* **15** (5):700-709.

Livesey, A.K. and Skilling, J. (1985). Maximum entropy theory. *Acta Cryst.* **A41** 113-122.

Lusted, L.B. (1960). Logical analysis in roentgen diagnosis. *Radiology* **74** 178-193.

Lusted, L.B. (1971). Signal detectability and medical decision-making. *Science* **171** 1217-1219.

MacIntyre, W.J., Saha, G.B. and Go, R.T. (1994). Planar imaging with single-head large-field-of-view cameras: are they still the workhorse? *Seminars in Nuclear medicine* **XXXIV** (1):11-16.

Magnussen, J.S., Chicco, P., Mackey, D.W., Murray, I.P.C. and Van Der Wall, H. (1997). Simulation of the stripe sign in a scintigraphic model of the lungs. *Nuclear Medicine Communications* **18** 648-654.

Magnussen, J.S., Chicco, P., Palmer, A.W., Mackey, D.W., Magee, M., Murray, I.P.C., Bautovich, G., Allman, K., Storey, G. and Van Der Wall, H. (1997). Optimization of the scintigraphic segmental anatomy of the lungs. *Journal of Nuclear Medicine* **38** 1987-1991.

Magnussen, J.S., Chicco, P., Palmer, A.W., Mackey, D.W., Magee, M., Murray, I.P.C., Bautovich, G., Allman, K., Storey, G. and Van Der Wall, H. (1998). Variability of perceived defect size in virtual lung scintigraphy. *Journal of Nuclear Medicine* **39** 361-365.

Mayneord, W.V., Turner, R.C., Newbery, S.P. and Hodt, H.J. (1951). A method of making visible the distribution of activity in a source of ionizing radiation. *Nature* **168** 762-765.

McGrath, D.M. (1998). Maximum entropy deconvolution of low count nuclear medicine images. [Thesis]. University of Southampton. PhD.

McNeil, B.J., Keeler, E. and Adelstein, J. (1975). Primer on certain elements of medical decision making. *The New England Journal of Medicine* **293** (5):211-215.

Meany, T.F., Raudkivi, U., MacIntyre, W.J. and et al (1980). Detection of low-contrast lesions in computed body tomography: An experimental study of simulated lesions. *Radiology* **134** 149-154.

Metz, C.E. (1974). Applications of ROC Analysis in diagnostic image evaluation. In: Neul, A.G., (Ed.) *Physics of Medical Imaging*, pp. 546-572.

Metz, C.E. (1978). Basic principles of ROC analysis. *Seminars in Nuclear medicine* **8** (4):283-298.

Metz, C.E. (1986). ROC methodology in radiological imaging. *Invest Radiol* **21** 720-733.

Metz, C.E., Shen, J.-H. and Herman, B.A. (1990). New methods for estimating a binormal ROC curve from continuously-distributed test results. Presented at the 1990 Annual Meeting of the American Statistical Association. Anaheim, CA, August 7, 1990:

Metz, C.E. (1993). Quantification of failure to demonstrate statistical significance the usefulness of confidence intervals. *Invest Radiol* **28** 59-63.

Metz, C.E., Herman, B.A. and Shen, J.-H. (1998). Maximum likelihood estimation of receiver operating characteristic (ROC) curves from continuously-distributed data. *Statist.Med.* **17** 1033-1053.

Metz, C.E., Herman, B.A. and Roe, C.A. (1998). Statistical comparision of two ROC-curve estimates obtained from partially-paired datasets. *Med Decis Making* **18** 110-121.

Metz, C.E., Starr, S.J. and Lusted, L.B. (1976). Observer performance in detecting multiple radiographic signals: prediction and analysis using a generalized ROC approch. *Radiology* **121** 337-347.

Metz, C.E. (1989). Some practical issues of experimental design and data analysis in radiological ROC studies. *Invest Radiol* **24** 234-245.

Miller, T.R. and Sampathkumaran, K.S. (1982). Digital filtering in nuclear medicine. *The Journal of Nuclear Medicine* **23** 66-72.

Miller, T.R., Goldman, K.J., Epstein, D.M., Biello, D.R., Sampathkumaran, K.S., Kumar, B. and Siegel, B.A. (1984). Improved interpretation of gated cardiac images by use of digital filters. *Radiology* **152** 795-800.

Moralidis, E., Woldman, S., Martin, W. and Hutton, I. (1998). Single crystal biplane equilibriem radionuclide ventriculography: An improved planar imaging technique. *Nuclear Medicine Communications* **19** 83-89.

Morrel, N.W., Nijran, K.S. and et al. (1993). The limitations of posterior view ventilation scanning in the diagnosis of pulmonary embolism. *Nuclear Medicine Communications* **14** 983-988.

Mountford, P.J. (1998). Techniques and limitations of planar imaging. In: Quantification in Nuclear Medicine Meeting. Paper presented at the British Institute of Radiology, London on 17 February 1998, pp.9-11.

Mouroulis, P.Z. and Cheng, X. (1994). Robustness of visual image quality measures against various monochromatic aberrations. *Optical Engineering* **33** (8):2626-2631.

Muhm, J.R., Miller, W.E., Fontana, R.S., Sanderson, D.R. and Uhlenhopp, M.A. (1983). Lung cancer detected during a screening program using four-month chest radiographs. *Radiology* **148** 609-615.

Myers, K.J., Barrett, H.H., Borgstorm, M.C., Patton, D.D. and Seeley, G.W. (1999). Effect of noise correlation on detectability of disk signals in medical imaging. *J.Opt.Soc.Am.A* **2** (10):1752-1759.

Narayan, T.K. and Herman, G.T. (1999). Prediction of human observer performance by numerical observers: an experimental study. *J.Opt.Soc.Am.A* **16** (3):679-693.

Neill, G.D.S. and Hutchinson, F. (1971). Computer detection and display of focal lesions on scintiscans. *British Journal of Radiology* **44** 962

Netter, F.H. (1989). *Atlas of human anatomy*, Basle, Switzerland: CIBA-GEIGY LIMITED.

Niederau, C. and Sonnenberg, A. (1984). Liver size evaluated by ultrasound: ROC curves for hepatitis and alcoholism. *Radiology* **153** 503-505.

Notes for Guidance on the Clinical Administration of Radiopharmaceuticals and Use of Sealed Radioactive Sources (1998). Administration of Radioactive Substances Advisory Committee.

Oestmann, J.W. (1995). The scientific work-up of radiographic image quality now and a decade ago: the radiologist's approach. *Radiation Protection Dosimetry* **57** (1-4):9-11.

Oittinen, P.T. and Saarelma, H.J. (1991). Application of information theory to characterize print quality. *Tappi Journal* **74** (8):197-203.

Ott, R.J., Flower, M.A., Babich, J.W. and Marsden, P.K. (1988). The physics of radioisotope imaging. In: Webb, S., (Ed.) *The Physics of Medical Imaging.*, Bristol and Philadelphia: Adam Hilger]

Park, K.H. and Park, S.B. (1987). Maximum entropy image reconstruction for an object with opaque obstructions. *IEEE Transactions on Medical Imaging* **MI-6** (4):308-312.

Penney, B.C., Glick, S.J. and King, M.A. (1990). Relative importance of the error sources in Wiener restoration of scintigrams. *IEEE Transactions on Medical Imaging* **9** (1):60-70.

Pina, R.K. and Puetter, R.C. (1992). Incorporation of spatial information in bayesian image reconstruction: the maximum residual likelihood criterion. *Publications of the Astronomical Society of the Pacific* **104** 1096-1103.

PIOPED Investigators (1990). Value of the ventilation / perfusion scan in acute

pulmonary embolism: Results of the prospective investigation of pulmonaryembolism diagnosis (PIOPED). *JAMA* **263** 2753-2759.

Pladellorens, J., Serrat, J., Castell, A. and Yzuel, M.J. (1992). Using mathematical morphology to determine left ventricular contours. *Phys.Med.Biol.* **37** 1877-1894.

Pladellorens, J., Serrat, J., Castell, J., Yzuel, M.J. and Escofet, J. (1997). Improving left ventricle volume calculation from gammagraphic images using a Wiener filter. *Physica Medica* **XIII** (1):17-23.

Pratt, W.K. (1978). *Digital Image Processing.*, New York: Wiley.

Pratt, W.K. (1991). *Digital image processing.*, New York: Wiley Interscience.

Pullan, B.R., Ritchings, R.T., Isherwood, I. and Adams, J.E. (1980). Effect of smoothing brain scans: a study using receiver operating characteristic curves. *J.Comput.Assist.Tomogr.* **4** (1):91-93.

Qian, w. and Clarke, L.P. (1996). Wavelet-based neural network with fuzzy-logic adaptivity for nuclear image restoration. *Proceedings of the IEEE* **84** (10):1458-1473.

Raff, U., Nelson, T.R. and Retenour, E.R. (1984). Improvement of SPECT imaging for myocardial perfusion studies using a median filter processing technique. *The Journal of Nuclear Medicine* **25** (5):P14

Rai, G.S., Haggith, J.W., Fenwick, J.D. and James, O. (1979). Clinical evaluation of computer processing of liver gamma camera scans. *British Journal of Radiology* **52** 116

Ranshoff, D.F. and Feinstein, A.R. (1978). Problems of spectrum and bias in evaluating the efficacy of diagnostic tests. *The New England Journal of Medicine* **299** (17):926-930.

Revesz, G., Shea, F.J. and Kundel, H.L. (1982). The effects of kilovoltage on diagnostic accuracy in chest radiography. *Radiology* **142** 615-618.

Ritchings, R.T., Isherwood, I., Pullan, B.R. and Kingsley, D. (1979). Receiver operating characteristic curves in the evaluation of hard copies of computed tomography scans. *J.Comput.Assist.Tomogr.* **3** (3):423-425.

Robertson, E.A., Zweig, M.H. and Steirteghem, A.C.V. (1983). Evaluating the clinical efficacy of laboratory tests. *American Journal Clinical Pathology* **79** 78-86.

Robertson, J.S. (1982). Radiation absorbed dose calculations in diagnostic nuclear medicine. *Int.J.Appl.Radiat.Isot.* **33** 981-990.

Rockette, H.E., Gur, D., Cooperstein, L.A. and et al. (1990). Effect of two rating formats in multi-disease ROC study of chest images. *Invest Radiol* **25** 225-229.

Rockette, H.E., Gur, D. and Metz, C.E. (1992). The use of continuous and discrete confidence judgments in receiver operating characteristic studies of diagnostic imaging techniques. *Invest Radiol* **27** 169-172.

Rolland, J.P., Barrett, H.H. and Seeley, G.W. (1991). Ideal versus human observer for long-tailed point spread functions: does deconvolution help? *Phys.Med.Biol.* **36** (8):1091-1109.

Rummeny, E.J., Wernecke, K., Saini, S., Vassallo, P., Wiesmann, W., Oestmann, J.W., Kivelitz, D., Reers, B., Reiser, M. and Peters, P.E. (1992). Comparison between high-field-strength MR imaging and CT for screening of hepatic metastases: A receiver operating characteristic analysis. *Radiology* **182** 879-886.

Sainfort, F. (1991). Evaluation of Medical Technologies: A generelized ROC analysis. *Med Decis Making* **11** 208-220.

Schepers, H. and Winkler, C. (1964). An automatic scanning system, using tape perforator and computer techniques. *Medical Radioisotope Scanning* **1** 321

Schouterden, K., Lairson, B.M. and Azarian, M.H. (1996). Optimal filtering of scanning probe microscope images for wear analysis of smooth surfaces. *Journal of Vacuum Society Technology B* **14** (6):3445-3451.

Shao, L., Karp, J.S. and Countryman, P. (1994). Practical considerations of the Wiener filtering technique on projection data for PET. *IEEE Transactions on Nuclear Science* **41** (4):1560-1565.

Sharp, P.F. (1989). The gamma-camera. In: Sharp, P.F., Gemmell, H.G. and Smith, F.W., (Eds.) *Practical Nuclear Medicine.*, pp. 5-14. Oxford: IRL Press.

Shepp, L.A. and Vardi, Y. (1982). Maximum likelihood reconstruction for emission tomography. *IEEE Transactions on Medical Imaging* **MI-1** (2):113-122.

Simon, T.R., Neumann, R.L., Gorelick, F.S., Riely, C.A., Hoffer, P.B. and Gottschalk, A. (1981). Scintigraphic diagnosis of cirrhosis: A receiver operating characteristic analysis of the common interpretive criteria. *Radiology* **138** 723-726.

Simpson, D.E., Fleming, J.S. and Daniell, G.J. (1993). Improvement of image quality in planar scintigraphy using maximum entropy. *Nuclear Medicine Communications* **14** 236

Simpson, D.E., Fleming, J.S., Aldous, A.J. and Daniell, G.J. (1995). Deconvolution of planar scintigrams by maximum entropy. *Phys.Med.Biol.* **40** 153-162.

Sipila, O., Nihhinen, P., Pohjonen, H., Poutanen, V.P., Visa, A., Savolainen, S., Katatila, T. and Liewendahl, K. (1997). Accuracy of a registartion procedure for brain SPET and MRI: Phantom and simulation studies. *Nuclear Medicine Communications* **18**, 517-526.

Skilling, J., Strong, A.W. and Bennett, K. (1979). Maximum-entropy image processing in gamma-ray astronomy. *Mon.Not.R.astr.Soc.* **187** 145-152.

Skilling, J. and Bryan, R.K. (1984). Maximum entropy image reconstruction: general algorithm. *Mon.Not.R.astr.Soc.* **211** 111-123.

Skilling, J. (1988). The axioms of maximum entropy. In: Erickson, G.J. and Smith, C.R., (Eds.) *Maximum Entropy and Bayesian Methods in Science and Engineering, Vol. 1 of Fundemental Theories of Physics.*, pp. 173-187. Kulwer Academic.

Skilling, J. (1991). Fundamentals of MaxEnt in data analysis. In: Buck, B. and Macaulay, V.A., (Eds.) *Maximum Entropy in Action.*, Oxford University Press.

Skretting, A., Strandmyr, E. and Lindegaard, M.W. (1990). A Norwegian nationwide quality assurance project in nuclear medicine: total performance in bone scintigraphy measured with a new transmission phantom. *Eur.J.Nucl.Med* **17** 10-14.

Smith, A.D.C., Smith, I.A.C. and Dance, D.R. (1998). Objective assessment of phantom image quality in mammography: a feasibility study. *The British Journal of Radiology* **71** 48-58.

Smith, E.M. and Brill, A.B. (1966). Progress with computers in nuclear medicine. *Nucleonics* **24** 58

Sorenson, J.A. and Phelps, M.E. (1987). *Physics in Nuclear Medicine.*, Second edn. W.B. Saunders company.

Staff, R.T., Gemmell, H.G. and Sharp, P.F. (1995). Assessment of energy-weighted acquisition in SPECT using ROC analysis. *The Journal of Nuclear Medicine* **36** (12):2352-2355.

Starck, S.A. and Carlsson, S. (1997). Digital filtering of bone scans: An ROC study. *Nuclear Medicine Communications* **18** 98-104.

Starr, S.J., Metz, C.E., Lusted, L.B. and Goodenough, D.J. (1975). visual detection and localization of radiographic images. *Radiology* **116** 533-538.

Stone, C.D., McCormick, J.W., Gilland, D.R., Greer, K.L., Coleman, R.E. and Jaszczak, R.J. (1998). Effect of registartion errors between transmission and emission scans ona SPECT system using sequential scanning. *The Journal of Nuclear Medicine* **39** 365-373.

Straub, W.H., Gur, D., Good, W.F., Campbell, W.L., Davis, P.L., Hecht, S.T., Skolnick, M.L., Thaete, F.L., Rosenthal, M.S. and Sashin, D. (1991). Primary CT diagnosis of abdominal masses in a PACS environment. *Radiology* **178** 739-743.

Sullivan, D.C., Coleman, R.E., Mills, S.R., Ravin, C.E. and Hedlund, L.W. (1983). Lung scan interpretation: Effects of different observers and different criteria. *Radiology* **149** 803-807.

Swensson, R.G. and Judy, P.F. (1981). Detection of noisy visual targets: Models for the effects of spatial uncertainty and signal-to-noise ratio. *Perception and Psychophysics* **29** 521-534.

Swets, J.A. (1979). ROC analysis applied to the evaluation of medical imaging techniques. *Invest Radiol* **14** (2):109-121.

Swets, J.A. and Pickett, R.M. (1982). *Evaluation of diagnostic systems: Methods from signal detection theory.*, New York: Academic Press.

Swets, J.A. (1986). Form of empirical ROCs in discrimination and diagnostic tasks: Implications for theory and measurement of performance. *Psychological Bulletin* **99** (2):181-198.

Swets, J.A. (1986). Indices of discrimination or diagnostic accuracy: Their ROCs and implied models. *Psychological Bulletin* **99** (1):100-117.

Swets, J.A., Getty, D.J., Pickett, R.M., D'orsi, C.J., Seltzer, S.E. and McNeil, B.J. (1991). Enhancing and evaluating diagnostic accuracy. *Med Decis Making* **11** 9-16.

Takaki, Y., Kojima, A., Tsuji, A., Nakashima, R., Tomiguchi, S. and Takahashi, M. (1993). Quantification of renal uptake of technitum-99m-DTPA using planar scintigraphy: A technique that considers organ volume. *The Journal of Nuclear Medicine* **34** (7):1184-1189.

Tanaka, E. and Iinuma, T.A. (1970). Approaches to optimal data processing in radioisotope imaging. *Phys.Med.Biol.* **15** (4):683-694.

Tauxe, W.N., Chaape, D.W. and Sprau, A.C. (1966). Contrast enhancement of scanning procedures by high speed computer. *Journal of Nuclear Medicine* **7** 647

Thompson, M.L. and Zucchini, W. (1989). On the statistical analysis of ROC curves. *Statist.Med.* **8** 1277-1290.

Todd-Pokropek, A. (1980). Image processing in nuclear medicine. *IEEE Transactions on Nuclear Science* **NS-27** (3):1080-1094.

Todd-Pokropek, A. and Gagnon, D. (1991). Optimization of scatter correction

techniques using energy information: How many (Photon) beans make five. In: *Information Processing in Medical Imaging*, pp. 155-170. Wiley-Liss, Inc.

Tourassi, G.D., Floyd Jr, C.E., Munley, M.T., Bowsher, J.E. and Coleman, R.E. (1991). Improved lesion detection in SPECT using MLEM reconstruction. *IEEE Transactions on Nuclear Science* **38** (2):780-783.

Tsui, B.M.W., Zhao, X., Frey, E. and Gullberg, G.T. (1991). Comparison between ML - EM and WLS - CG algorithms for SPECT image reconstruction. *IEEE Transactions on Nuclear Science* **38** (6):1766-1772.

Turner, D.A., Fordham, E.W., Pagano, J.V., Ali, A.A., Ramos, M.V. and Ramachandran, P.C. (1976). Brain scanning with the Anger multiplane tomographic scanner as a second examination. *Radiology* **121** 115-124.

Turner, D.A., Ramachandran, P.C., Ali, A.A., Fordham, E.W. and Ferry, T.A. (1976). Brain scanning with the Anger multiplane tomographic scanner as a primary examination. *Radiology* **121** 125-129.

Turner, D.A. (1978). An intuitive approach to receiver operating characteristic curve analysis. *Journal of Nuclear Medicine* **19** 213-220.

Turner, S. and Cerrina, F. (1993). Optimization of aerial image quality. *J.Vac.Sci.Technol.B* **11** (6):2446-2451.

Uchida, I., Onai, Y., Ohahi, Y., Tomaru, T. and Irfune, T. (1979). Quantitative diagnosis of breast thermograms by a computer. *NIPPON ACTA RADIOLOGICA* **30** 401-411.

Wagner, R.F. and Brown, D.G. (1985). Unified SNR analysis of medical imaging systems. *Phys.Med.Biol.*, **30** (6):489-518.

Wang, Ge., Skinner, M.W. and Vannier, M.W. (1995). Temporal bone volumetric image deblurring in spiral computed tomography scanning. *Acad Radiol* **2** 888-895.

Ward, A.L., Tan, R.J. and Kaul, R. (1994). Spike leakage of thin Si PIN limiters. *IEEE Transactions on Microwave Theory and Techniques* **42** (10):1879-1885.

Warren, R.C. (1981). Contrast and latitude of CT hard copy: An ROC study. *Radiology* **141** 139-145.

Warren, R.C. and Pandya, Y.V. (1982). Effect of window width and viewing distance in CT display. *The British Journal of Radiology* **55** 72-74.

Webb, S., Long, A.P., Ott, R.J., Leach, M.O. and Flower, M.A. (1985). Constrained deconvolution of SPECT liver tomograms by direct digital image restoration. *Medical Physics* **12** (1):53-58.

Webb, S. (1985). Comparison of data-processing techniques for the improvement of contrast in SPECT liver tomograms. *Phys.Med.Biol.*, **30** (10):1077-1086.

Webb, S. (1988). The mathematics of image formation and image processing. In: Webb, S., (Ed.) *The Physics of Medical Imaging*, Bristol and Philadephia: Adam Hilger

Wieand, S., Gail, M.H., James, B.R. and James, K.L. (1989). A family of nonparametric statistics for comparing diagnostic markers with paired or unpaired data. *Biometrika* **76** (3):585-592.

Wiener, S.N., Flynn, M.J. and Edelstein, J. (1980). Observer performance with computer-generated images of ^{201}Tl-Cl myocardial perfusion. *Radiology* **30** 181-185.

Wilson, A.J., Mann, F.A., Murphy, Jr.W.A., Monsees, B.S. and Linn, M.R. (1991). Photostimulable phosphor digital radiography of the extremities: Diagnostic accuracy compared with conventional radiography. *American Journal of Roentgenology* **157** 533-538.

Winter, L.H.L. and Chakraborty, D.P. (1990). Free-response methodology: Alternate analysis and a new observer-performance experiment. *Radiology* **174** 873-881.

Yamada, I. and Tanaka, K. (1994). Detectability in nuclear medicine images by a random-dot modle: a theoretical analysis. *Applied Optics* **33** (14):2900-2908.

Yanch, J.C., Webb, S., Flower, M.A. and Irvine, A.T. (1987). Constrained deconvolution to remove resolution degradation caused by scatter in SPECT. In: Yanch, J., (Ed.) *Information Processing in Medical Imaging*, pp. 263-276.

Yanch, J.C., Flower, M.A. and Webb, S. (1988). A Comparison of deconvolution and windowed subtraction techniques for scatter compensation in SPECT. *IEEE Transactions on Medical Imaging* 7 (1):13-20.

Yerushalmy, J. (1969). The statistical assessment of the variability in observer perception and description of roentgenographic pulmonary shadows. *The Radiologic Clinics of North America* 7 (3):381-392.

Zalevsky, Z. and Mendlovic, D. (1996). Fractional Wiener filter. *Applied Optics* **35** (20):3930-3936.